First-principle study of atomic and electronic structures of 3C-SiC(111)/Si(110) interfaces

Eric K. K. ABAVARE
(Doctoral Program in Frontier Science)

Submitted to the Graduate School of
Pure and Applied Sciences
in Partial Fulfillment of the Requirements
for the Degree of Doctor of Philosophy in
Science

at the
University of Tsukuba

Abstract

3C-SiC(111) on Si (110) surface with a particular alignment of the two planes offers almost perfect fake matching of the lattice periodicity, albeit dense 3C-SiC and sparse Si in spite of the large lattice mismatch ~20% between them. We here report total-energy electronic-structure calculations based on real-space density functional theory (RSDFT), which elucidate new reconstruction mechanism of dense 3C-SiC(111) on sparse Si(110) surface with the relaxed superstructures displaying undulation near the interface. We explore a variety of candidate interface structures and reach two distinctive types called type I and II which show bistability at the interface. We define interface energy as the energy difference between the total energy of the interface structure and the energy of the bulk constituent atoms. In type I, the interface energy where the silicon faces meet each other (silicon-silicon) is calculated as 9.571 eV/cell or 0.117 eV/Å^2 whereas the interface energy where the silicon and carbon faces meet (silicon-carbon) is 10.406 eV/cell or 0.127 eV/Å^2. Similarly, in type II, silicon-silicon interface energy is 9.890 eV/cell or 0.121 eV/Å^2 and that of silicon-carbon is 10.840 eV/cell or 0.133 eV/Å^2. Hence, We conclude that in both types, the silicon-silicon interface is energetically favorable compared with the silicon-carbon interface. The mechanism of the interface reconstruction is that, one of the Si(110) interfacial layer atoms in the supercell completely breaks a nearest neighbor sp^3 bond to relax the strain between 3C-SiC(111) and Si(110) which might be the origin of the undulation and relate to the lattice mismatch. We propose that bond breaking creates a defect hole perpendicular to the interface around which charges are redistributed. The new extended rebonding arrangement result in energy gain and subsequently make the overall electronic property of the interface system exhibit semiconducting behavior.

Acknowledgements

I am very thankful to the great I am that I am, the maker of the universe, the heavens and the earth. I wish to take this opportunity to express my profound gratitute to Professor Atsushi Oshiyama and to say "Aye koo, me dawua ase" meaning thank you so much for your invaluable contribution throughout my study under you in Japan, a great chance and great challenge. I am deeply indebted to Professor Kenji Shiraishi and Professor Susumu Okada for their help and advice and hearty support during the course of my study. I am also very grateful to Professor Sukmin Jeong and Professor Mauro Boero for valuable discussions. I wish to thank Dr. Kazuyuki Uchida, Dr. Jun-ich Iwata, Dr. Yoshihiro Gohda, Dr. Yoshitaka Fujimoto, Dr. Shinnosuke Furuya, Dr. Kenichi Koizumi, Dr. Sung Dongchul, Dr. Katsumasa Kamiya for various help and advice. I would also like to thank the present graduate students namely Yuichiro Matsushita, Shinya Kyogoku, Hirota Sho, Suda Shota, Enkhtaivan Batnyam and past students Dr. Kentaro Takai, Dr. Takahiro Kurita, Messrs. Igarashi Masayuki, Kenji Kobayashi, Mitsuru Nishikawa, Masahide Yoshimura for various help and making my laboratory life a memorable one. My special thanks goes to Dr. Kazuyuki Uchida who taught me how to do scientific computing.

I wish to thank the entire congregation of Tsukuba International Christian Assembly (TICA) for their prayers and spiritual support. I am also indebted to Ms. Kaori Iizumi and family for their invaluable support. I thank all my numerous friends whose confidence in me has seen the success of this work.

Lastly but not the least, I wish to express my sincere thanks to the members of the Abavare family, my in-laws for their continual encouragement and support throughout my stay and above all my beloved wife whose cynicism gave me strength to push on.

Contents

Chapter 1

Introduction

Heteroepitaxial growth of two dissimilar semiconductor materials has widespread applications in modern solid state electronics. The developments of modern electronics and large-scale integrated circuits need multilayer semiconductor structures with a thick substrate and multiple thin layers on top. The doping levels or chemical compositions of the multilayer may be quite different from each other. Generally, two broad classes of devices are considered. In the first class, carrier transport is across the interface (heterojunction bipolar transistor (HBT), lasers, photodiodes, light-emitting diode, etc.), and in the second class, transport is along the interface (meta-oxide-semiconductor field-effect transistor and others). Heterojunction parameters such as the valence- and conduction band discontinuities, and the built-in potentials determine the performance of both classes of devices. For example, they affect carrier confinement on both sides of the active region where radiative recombination occurs in the heterojunction lasers, emitter efficiencies in HBTs, as well as the gate voltage swing and the gate leakage current in modulation-doped field effect transistor structures [1].

In current growth techniques such as molecular beam epitaxy, it is observed that strain can build into a given semiconductor material by growing it on top of a suitable lattice-mismatched substrate [2]. Lattice-mismatched heterostructures can be grown with essentially no misfit-originated defect generation if the layers are sufficiently thin; the mismatch is then completely accommodated by uniform lattice strain. The lattice constants parallel to the interface adjust so that perfect matching of the two materials is obtained [3]. If the lattice mismatch is large or the overlayer is too thick, the strain becomes too large and

misfit dislocations are formed to release the strain, allowing the overlayer to approach its own lattice constant. This type of growth is usually called islanding. But if the lattice mismatch is modest and the overlayer is thin enough (below the critical layer thickness), the so called pseudomorphic or commensurate growth is achieved (epilayers). The overlayer assumes then an in-plane lattice constant equal to that of the substrate which acts as a template. In short, three experimentally observed hetreoepitaxial growth modes are known and loosely described as layer-by-layer, islanding and layer-by-layer plus islanding [4].

Silicon carbide SiC [5] is a semiconductor with many polytypes [6–8] which has a different stacking sequence of double layers of Si and C atoms and wide indirect band gap [9]. It is the focus of attention recently as a potential material for high-power and high-frequency applications requiring high-temperature operation. It is chemically inert, stable at high temperature environment and its radiation damage resistance makes it useful for power electronics device application. Some of the possible applications of SiC as a material for power electronics are for advanced turbine engines, propulsion systems, automotive and aerospace electronics and applications requiring large radiation damage resistance. Properties such as large breakdown electric field strength, large saturated electron drift velocity, small dielectric constant, reasonably high electron mobility and high thermal conductivity make SiC a promising candidate for fabricating power devices with reduced power losses [10–12]. The experimental production of SiC-based gas sensors to optimize fuel efficiency and reduce emission have been proposed [13] for example. They are expected to perform under steady state and transient conditions while operating reliably in high pressure, harsh erosive environments. In spite of the potential usefulness and the impressive volume of research papers on it, the realization of SiC technological application still remains a science fiction. The main reason for this until now is that, research pertaining to SiC electronic devices and their practical applications is hampered by the lack of reproducible techniques to grow semiconductor-quality single large crystals and epilayers by sublimation process.

The heteroepitaxial growth of SiC on a foreign substrate has the potential to solve the size issue and can probably be the only way presently. It is reported that among the SiC polytypes, the one capable of epitaxial growth on a substrate specifically Si, is the cubic 3C-SiC or β-SiC form [14]. The reason for this might be due to the fact that Si is also a cubic structure material. Regarding the enlargement of the size of SiC single

crystals, the possibility to grow 3C-SiC on Si substrates is very attractive. For example, if 3C-SiC of 30-cm in diameter can be epitaxially grown on a Si substrate its impact will be tremendous from a technological point of view. For example, graphene science [15] and graphene technology [16] on SiC is an envisaged next-generation technology material. The boom is related to the intention of forming wide area graphene on SiC rather than scotch-tape manufacturing and it is now established as an alternative, more practical and viable method to fabricate a large graphene sheet. The strong reason is because, graphene is a promising contender to succeed the throne of silicon in electronics beyond complementary metal-oxide-semiconductor (CMOS) [17]. The challenges for graphene-on-SiC technology however, are the abdication of the well-established Si technologies and the high production cost of bulk SiC crystals. The preparation of single-layer graphene by thermal decomposition of SiC is proposed as a potential route for the synthesis of uniform wafer-size graphene layers for technological applications. As a consequence, the devices fabricated based on 3C-SiC on the Si substrate have the potential of being integrated onto the already well established Si-based devices [18, 19].

The progress on high-quality single-crystal growth of cubic 3C-SiC using chemical vapor deposition (CVD) method was pioneered by Nishino and his coworkers as well as other researchers [20–23]. This has brought tremendous advance for the potential application of SiC as a high temperature semiconductor material. However, the improvement in the growth technique of 3C-SiC on Si is currently a setback to realize 3C-SiC on a large area substrate.

The most widely utilized substrate material for 3C-SiC growth is Si(001) surface [24–31]. A group reported on the surface morphology, defects, as well as atomic structure and composition of the cubic film grown on Si(001) [22]. The growth temperature of 3C-SiC on Si substrate is usually achieved at temperatures higher than 1000° after formation of a carbonized buffer layer [32]. As a result of the high vapor pressure of Si at such a high temperature [33], structural damage and formation of voids are liable to occur at the interface. Again, efforts to grow high quality 3C-SiC epitaxial film on the Si substrate are also hindered largely by the structural difference between the two semiconducting materials. The problems are largely intrinsic in the heteroepitaxial growth such as the mismatch of the lattice constants. The presence of a large lattice mismatch of ~20% between the lattice parameters, $a_{si} = 5.43$ and $a_{sic} = 4.36$Å affect heteroepitaxy [34].

Another parameter that influences the heteroepitaxial quality is the difference in thermal expansion coefficients (~8%) between the two materials. This generates additional severe strain in the epitaxial film during the cooling process after growth. The strain causes defects at the interface and in the film itself, as misfit dislocation, stacking faults, cracks, twinning rotations and antiphase domains [35, 36]. The antiphase boundary forms deep levels in the energy gap and acts as scattering centers for carriers [37]. The presence of such defects degrades interface morphology and result in a poor crystalline quality of 3C-SiC and consequently in poor device characteristics. It is of highest priority to form a qualified epitaxial film on top of Si substrate. Therefore the large lattice mismatch between 3C-SiC and Si crystals is a real challenge for researchers; as a result, the growth between the two crystals is generally thought of as impossible to occur.

However, by special crystallographic orientation and alignments, 3C-SiC on Si can be made to almost lattice match perfectly in a fake way. The fake matching of 3C-SiC and Si makes it quite different from other forms of important interfaces already known in the past which are not fake matched. Few examples are given here to illustrate the point of non-fake matching semiconductors which exhibit moderately lattice mismatch at their interfaces includes InAs on GaAs(110) 7.2% [38–40], Ge on Si(100) 4% [41, 42] and 3C-SiC on GaN 3.4% [43] with respect to their corresponding substrates. As a consequence, epitaxial growths are achieved between these semiconductors with slight interface modifications due to their respective mismatches. Although in some planes and directions, 3C-SiC on Si appears to match, [34] this is fake because the atom in 3C-SiC has no partner on the substrate atoms. Until now, nobody has investigated this type of interface from atomic point of view. As a result, we are motivated in the present work to quantum-mechanically clarify this unknown interface system.

It is reported that heteroepitaxial growth of 3C-SiC on Si is strongly related to the orientation of the Si substrate used for the growth. Recently, Nishiguchi and his coworkers have succeeded in epitaxially growing 3C-SiC on Si by CVD method with a good fake lattice matching for the first time. They observed the crystallographic relationship that Si(110) surface is parallel to 3C-SiC(111) and that the Si[$\bar{1}$10] direction is parallel to 3C-SiC[$\bar{1}$10] direction as shown in Figure1.1 [28, 34]. Following their method [34], other workers have succeeded in growing graphene films on insulating 3C-SiC(111)/ Si(111) [46, 49, 50], 3C-SiC(111)/ Si(110) [45], 3C-SiC(110)/Si(110) [46] and 3C-SiC(100)/Si

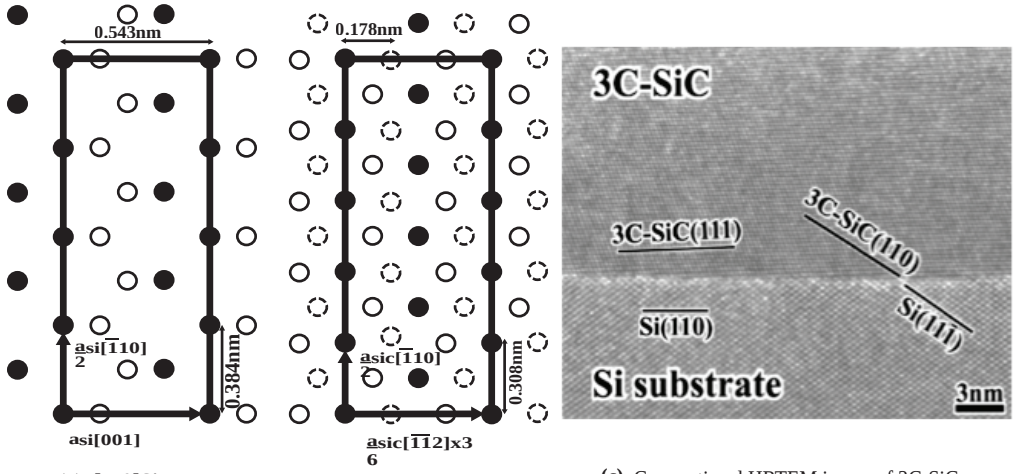

Figure 1.1: The schematic atomic projections of (a) [110] Si and (b) [111] 3C-SiC. Solid black, circles and hatched circle represent the first, second and third layers of atoms, which exist within the same plane. (c) 3C-SiC(111) grown on the Si substrate [34]

wafers [48] superlattatices by gas-source molecular beam epitaxy.

Nishiguchi and his collaborators reasoned that Si(110) surface could match 3C-SiC(111) in which Si[001] direction is parallel to 3C-SiC[$\bar{1}\bar{1}2$] with surprisingly drastic reduction in the lattice mismatch to 1.6% with Si[$\bar{1}10$] direction parallel to 3C-SiC[$\bar{1}10$]. Of course 3C-SiC[$\bar{1}10$] and Si[$\bar{1}10$] should not match but five-time 3C-SiC periodicity matches with four-time Si periodicity along [$\bar{1}10$] direction with corresponding lattice mismatch of 0.2%. We emphasize that, this fake matching intuitively suggests, one of every 5th of Si in 3C-SiC along [$\bar{1}10$] direction might be lonely in the Si region which means that the heterostructure may be energetically unfavorable. The reason is that the number of 3C-SiC(111) surface atoms are more (dense) than those of Si(110) surface atoms(sparse). The difference in the number of atoms between the two crystal planes at the interface area may result in some intrinsic effects, for example, nature of dangling bonds (DBs), reconstruction and relaxation mechanism.

With the above fake matching, it is evident that the atomistic understanding of this interface heterostructure is not known yet, since there is no report on this important interface system. It is technologically important and scientifically interesting to clarify the interface morphology of these two important semiconductors as two group IV elements of different ionicity and electronegativity participates in bonding. Knowledge about the physics and chemistry of this kind of interface is crucial but it is presently lacking. What we need to

clarify includes determination of the nature of relaxation and reconstruction mechanism of the interface, especially how flat is the interface between the two crystal planes and what kind of atoms exist at the interface that yields most stable atomic geometry? What is the nature of electronic charge distribution and the interface states? We shall understand this heterojunction atomic and electronic properties based on accurate and reliable first-principles calculations.

In this thesis, we use (111) and $(\bar{1}\bar{1}\bar{1})$ index planes of 3C-SiC corresponding to Si- and C- terminations respectively, or Si- and C- rich surfaces. These are often used interchangeably. In the same way, if no reference to an index plane is used, it is called bulk-terminated. These terminologies are frequently used in the literature. For the sake of completeness, we study surface energies and surface electronic properties of Si(110), Si- and C- terminated surfaces. The reason is that these data are unavailable but relevant to science and technology.

We denote the interface system of 3C-SiC(111) on Si(110) surface as nL/nL where *n* is a *natural number* to describe the number of atomic-layers for each material to be used and L indicate atomic layers. In this thesis, we focus on 8-atomic layers (8L) of 3C-SiC(111) grown epitaxially on top of 8-atomic layers of Si(110) substrate which we write as (8L/8L) constituent slabs which we find to converge and sufficient to discuss realistic interface structures. There are two candidates heterojunctions under consideration, for example, if silicon and silicon face meet each other, we call it Si-Si interface and if silicon and carbon face meet similarly, we call it Si-C interface. These notations we shall frequently use to describe the interface systems accordingly.

We perform detailed geometric and electronic-structure calculations based on density functional theory (DFT) in the framework of real-space formalism. DFT is a powerful tool to reveal atom-scale mechanisms for a variety of phenomena in real materials, capable of treating quantitatively the physics and chemistry of these materials including two dissimilar interface systems such as the one under present investigation. We find new reconstruction mechanism of dense 3C-SiC(111) on sparse Si(110) surface with relaxed structures displaying undulation near the interface.

We explore a variety of candidate interface structures after extensive, accurate and reliable total-energy minimization calculations. We reach two distinctive structures and call them type I and II which shows bistability and undulation at the interface. In all types,

Si-Si interface is found to be energetically favorable compared with the Si-C interface. The mechanism of reconstruction and relaxation is clarified. The 3C-SiC sp^3 bonds are more difficult to bend than Si, therefore at the Si-Si interface bond bending is more flexible than the bending at the Si-C interface. Hence the strain at the Si-C interface is more than that at Si-Si interface.

The mechanism of the interface reconstruction is the breaking of one Si(110) surface layer atom bond in the supercell which causes the disappearance of excess partially occupied dangling bonds from 3C-SiC(111) side. This results in the formation of extended floating bonds around a hole at the interface due to new electron redistribution. The peculiar atomic relaxation near the interface is characterized by the interface electron states. We note that, irrespective of the interface system, the band dispersion at the interface structures shows semiconducting behavior. The extended floating bond around a hole can be arranged periodically, hence the reason for the strong dispersion near the interface. It is expected that, these floating interface states and the defect hole near the interface should be detected by experiment in the future.

The organization of this dissertation is as follows. In Chapter 2, we present the computational methods used to carry out the research. We describe the method of the first-principles total-energy electronic-structure calculation based on density functional theory in the framework of the real space formalism. We then introduce the calculation model and conditions. In Chapter 3, we show the results of atomic and electronic structure calculations of Si(110) surface as well as the (111) and $(\bar{1}\bar{1}\bar{1})$ index planes of 3C-SiC terminated surfaces. In Chapter 4, we show the results of calculations of Si(110)/3C-SiC(111) interface by determining the energetics, relaxation mechanism and band structures. In order to confirm the results of the interface calculations, we also prepare pre-relaxed slabs of 8L 3C-SiC(111) and Si(110) surfaces appropriately and match the two slabs to form the interface. Finally in Chapter 5, we give conclusions of the present dissertation.

Chapter 2

Method of Computation

In this chapter, We describe the computational approach adopted in the present thesis. The Born-Oppenheimer approximation (BOA) is outlined in section 2.1. Density functional theory DFT is discussed in section 2.2. We review the pseudopotential scheme, show how to solve the Kohn-Sham equations on three dimensional grid and finally demonstrate how to perform practical electronic structure calculations.

2.1 Born Oppenheimer Approximation

We first present the BOA based on an assumption that the electronic motion and the nuclear motion in a system consisting of nuclei and electrons can be separated because nuclei are more massive and treated as fixed than electrons. As a result, the electrons see the ions as providing a kind of electrostatic background in which they move. This physical picture is the very heart of the BOA [51]. It is useful at the onset to consider the total Hamiltonian of a many body system as:

$$\begin{aligned}\hat{H} &= -\sum_i \frac{\hbar^2\nabla_i^2}{2m_i} + \frac{1}{2}\sum_{i\neq j}\frac{e^2}{|\boldsymbol{r}_i-\boldsymbol{r}_j|} - \sum_{i,I}\frac{Z_I e^2}{|\boldsymbol{r}_i-\mathbf{R}_I|} \\ &\quad -\sum_I \frac{\hbar^2\nabla_I^2}{2M_I} + \frac{1}{2}\sum_{I\neq J}\frac{Z_I Z_J e^2}{|\mathbf{R}_I-\mathbf{R}_J|} \\ &= \hat{T}_e + \hat{U}_{ee}(\boldsymbol{r}) + \hat{U}_{eN}(\boldsymbol{r},\boldsymbol{R}) + \hat{T}_N + \hat{U}_{NN}(\boldsymbol{R}). \end{aligned} \tag{2.1}$$

where $\boldsymbol{R}_I$, $\boldsymbol{M}_I$ and $\boldsymbol{Z}_I$ denote coordinates, masses and atomic numbers of nuclei respectively and $\boldsymbol{r}_i$ is the electronic coordinates. The constants e and m are the charge and mass of an electron. The summations are over the number of electrons N_e and nuclei N_n. The direct treatment of this Hamiltonian is formidably difficult due to the $3(N_e+N_n)$ degrees of freedom in the system. Historically, the development of condense matter theory has been a way of seeking for an eigenfunctions and eigenvalues of this Hamiltonian. The Born-Oppenheimer approximation allows one to say that the nuclei are nearly fixed with respect to electron motion (adiabatic approximation). Note that this Hamiltonian is universal because it describes all everyday matter from biological macromolecules such as proteins, enzymes and nucleic acids, to metals and semiconductors to synthetic materials such as plastics. Thus, if we can solve for the eigenvalues and eigenfunctions of this Hamiltonian, we can predict any property we wish of a given system. The second line of Eq. (2.1), $\hat{T}, \hat{U}_{ee}, \hat{U}_{eN}, \hat{T}_N$ and $\hat{U}_{NN}$ represents the electron kinetic energy term, the electron-electron interaction term, the electron-nucleus interaction term, the nuclear kinetic term and the nucleus-nucleus interaction term respectively. The coordinates of electrons, $\{\boldsymbol{r}_1, \boldsymbol{r}_2, \cdots\}$, for simplicity are labeled as $\{\boldsymbol{r}_i\}$ and similarly for nuclei position, $\{\boldsymbol{R}_1, \boldsymbol{R}_2, \cdots\}$ are labeled as $\{\boldsymbol{R}_i\}$.

The time-independent Shrödinger equation is written as:

$$\hat{H}\Psi(\boldsymbol{r}, \boldsymbol{R}) \;=\; E\Psi(\boldsymbol{r}, \boldsymbol{R}). \tag{2.2}$$

where $\Psi(\boldsymbol{r}, \boldsymbol{R})$ is the full wave function and E is an eigenvalue. The approximate wavefunction (a function of the electronic position and nuclear position) in separable form is written as $\Psi(\boldsymbol{r}, \boldsymbol{R}) \;=\; \psi(\boldsymbol{r}, \boldsymbol{R})\Phi(\boldsymbol{R})$, where $\psi(\boldsymbol{r}, \boldsymbol{R})$ is an electronic wavefunction that parametrically depends on the nuclear positions and $\Phi(\boldsymbol{R})$ is the nuclear wavefunction. The electronic wavefunction represent the electronic state for fixed nuclear configuration $\mathbf{R_I}$. The nuclear wavefunction is actually the solution to the rotational-vibrational problem for the nuclear coordinates in the presence of an electronic potential energy surface.

Consider again the original Hamiltonian (2.1). An exact solution can be obtained by using an (infinite) expansion of the form

$$\Psi(\boldsymbol{r}, \boldsymbol{R}) \;=\; \sum_k \psi_k(\boldsymbol{r}, \boldsymbol{R})\Phi_k(\boldsymbol{R}), \tag{2.3}$$

although, to the extent that the BOA is valid, very accurate solutions can be obtained using only one or few terms. Equation (2.2) can be re-written by substituting it into equation (2.3) as follows:

$$\hat{H}\psi_k(\boldsymbol{r},\boldsymbol{R})\Phi_k(\boldsymbol{R}) \;=\; E_k\psi_k(\boldsymbol{r},\boldsymbol{R})\Phi_k(\boldsymbol{R}). \tag{2.4}$$

Substituting Eq. (2.1) into Eq. (2.4) yields

$$\left(\hat{T}_e + \hat{U}_{ee}(\boldsymbol{r}) + \hat{U}_{eN}(\boldsymbol{r},\boldsymbol{R}) + \hat{T}_N + \hat{U}_{NN}(\boldsymbol{R})\right)\psi_k(\boldsymbol{r},\boldsymbol{R})\Phi_k(\boldsymbol{R}) \;=\; \left(E_{ke} + E_{kN}\right)\psi_k(\boldsymbol{r},\boldsymbol{R})\Phi_k(\boldsymbol{R}) \tag{2.5}$$

Equation (2.5) is then grouped into two parts as:

$$\begin{aligned}&\left\{\left(\hat{T}_e + \hat{U}_{ee}(\boldsymbol{r}) + \hat{U}_{eN}(\boldsymbol{r},\boldsymbol{R})\right)\psi_k(\boldsymbol{r},\boldsymbol{R}) - E_{ke}\psi_k(\boldsymbol{r},\boldsymbol{R})\right\}\Phi_k(\boldsymbol{R})\\ &+\left\{\left(\hat{T}_N + \hat{U}_{NN}(\boldsymbol{R})\right)\psi_k(\boldsymbol{r},\boldsymbol{R})\Phi_k(\boldsymbol{R}) - E_{kN}\psi_k(\boldsymbol{r},\boldsymbol{R})\Phi_k(\boldsymbol{R})\right\} \;=\; 0\end{aligned} \tag{2.6}$$

Equation (2.6) is satisfied if $\psi_k(\boldsymbol{r},\boldsymbol{R})$ and $\Phi_k(\boldsymbol{R})$ are the solutions of the following two coupled equations

$$\left(\hat{T}_e + \hat{U}_{ee}(\boldsymbol{r}) + \hat{U}_{eN}(\boldsymbol{r},\boldsymbol{R})\right)\psi_k(\boldsymbol{r},\boldsymbol{R}) \;=\; E_{ke}\psi_k(\boldsymbol{r},\boldsymbol{R}). \tag{2.7}$$

and

$$\left(\hat{T}_N + \hat{U}_{NN}(\boldsymbol{R})\right)\psi_k(\boldsymbol{r},\boldsymbol{R})\Phi_k(\boldsymbol{R}) \;=\; E_{kN}\psi_k(\boldsymbol{r},\boldsymbol{R})\Phi_k(\boldsymbol{R}). \tag{2.8}$$

Substituting Eq. (2.7) into the left-hand side of Eq. (2.5) is expressed as

$$\begin{aligned}&E_{ke}\psi_k(\boldsymbol{r},\boldsymbol{R})\Phi_k(\boldsymbol{R}) + \left(\hat{T}_N + \hat{U}_{NN}(\boldsymbol{R})\right)\psi_k(\boldsymbol{r},\boldsymbol{R})\Phi_k(\boldsymbol{R})\\ &= E_{ke}\psi_k(\boldsymbol{r},\boldsymbol{R})\Phi_k(\boldsymbol{R}) + \left(-\sum_I \frac{\hbar^2\nabla_I^2}{2M_I} + \hat{U}_{NN}(\boldsymbol{R})\right)\psi_k(\boldsymbol{r},\boldsymbol{R})\Phi_k(\boldsymbol{R})\\ &= E_{ke}\psi(\boldsymbol{r},\boldsymbol{R})\Phi_k(\boldsymbol{R})\\ &-\sum_I \frac{\hbar^2}{2M_I}\left((\nabla_I^2\psi_k(\boldsymbol{r},\boldsymbol{R}))\Phi_k(\boldsymbol{R}) + 2(\nabla_I\psi_k(\boldsymbol{r},\boldsymbol{R}))(\nabla_I)\Phi_k(\boldsymbol{R}) + \psi_k(\boldsymbol{r},\boldsymbol{R})(\nabla_I^2\Phi_k(\boldsymbol{R}))\right)\\ &+\hat{U}_{NN}(\boldsymbol{R})\psi_k(\boldsymbol{r},\boldsymbol{R})\Phi_k(\boldsymbol{R})\\ &= \psi_k(\boldsymbol{r},\boldsymbol{R})\left(-\sum_I \frac{\hbar^2\nabla_I^2}{2M_I} + \hat{U}_{NN}(\boldsymbol{R} + E_{ke}(\mathbf{R})\right)\Phi_k(\boldsymbol{R})\\ &-\sum_I \frac{\hbar^2}{2M_I}\left\{\left((\nabla_I^2\psi_k(\boldsymbol{r},\boldsymbol{R}))\Phi_k(\boldsymbol{R}) + 2(\nabla_I\psi_k(\boldsymbol{r},\boldsymbol{R}))\nabla_I\Phi_k(\boldsymbol{R})\right)\right\}.\end{aligned} \tag{2.9}$$

If the last term of the right-hand side of Eq. (2.9) is ignored, we obtain an eigenvalue equation for the nuclear degrees of freedom

$$\left(-\sum_I \frac{\hbar^2\nabla_I^2}{2M_I} + E_{ke}(\boldsymbol{R}) + \hat{U}_{NN}(\boldsymbol{R})\right)\Phi_k(\boldsymbol{R}) \;=\; E_k(\boldsymbol{R})\Phi_k(\boldsymbol{R}). \tag{2.10}$$

Equations (2.7) and (2.10) are the principal results of the BOA. Now, we can solve equation Eq. (2.2) as follows. First solve equation (2.7), followed by solving Eq. (2.10). This implies that the motion of nuclei and electrons can be separated provided the second term in Eq. (2.9) is neglected. The solutions to Eq. (2.10) describe the phonon modes of the nuclei. Also, each electronic eigenvalue $E_{ke}(\mathbf{R})$ will give rise to an electronic surface, and these surfaces are known as Born-Oppenheimer surfaces. Thus, the full internuclear potential for each electronic surface is given by $\hat{U}_{NN}(\mathbf{R}) + E_{ke}(\mathbf{R})$. On each Born-Oppenheimer surface, the nuclear eigenvalue problem can be solved, which yields a set of levels (rotational and vibrational in the nuclear motion).

We justify the treatment of Eq. (2.9) that, the second term diagonal matrix element

$$-\sum_I \int d\boldsymbol{r}d\boldsymbol{R}\psi^*_{k'}(\boldsymbol{r},\boldsymbol{R})\Phi^*_{k'}(\boldsymbol{R})\frac{\hbar^2}{2M_I}\Big\{(\nabla_I^2\psi_k(\boldsymbol{r},\boldsymbol{R}))\Phi_k(\boldsymbol{R}) + 2(\nabla_I\psi_k(\boldsymbol{r},\boldsymbol{R}))\nabla_I\Phi_k(\boldsymbol{R})\Big\}, \tag{2.11}$$

can indeed be neglected. The first term in (2.11) is as follows:

$$-\sum_I \int d\boldsymbol{r}d\boldsymbol{R}\psi^*_{k'}(\boldsymbol{r},\boldsymbol{R})\Phi^*_{k'}(\boldsymbol{R})\left(\left(\frac{\hbar^2\nabla_I^2}{2M_I}\psi_k(\boldsymbol{r},\boldsymbol{R})\right)\Phi_k(\boldsymbol{R})\right). \tag{2.12}$$

The wavefunction, $\psi_k(\boldsymbol{r},\boldsymbol{R})$, depends on the difference between $\boldsymbol{r_i}$ and $\boldsymbol{R_I}$. Thus, the derivative of the wavefunction with respect to $\boldsymbol{R_I}$ is opposite in sign to the derivative of the wavefunction with respect to $\boldsymbol{r_i}$:

$$\nabla_I\psi_k(\boldsymbol{r},\boldsymbol{R}) \;=\; -\nabla_i\psi_k(\boldsymbol{r},\boldsymbol{R}). \tag{2.13}$$

Equation (2.12) can be re-written as:

$$-\sum_I \frac{m_i}{M_I}\int d\boldsymbol{R}\Phi^*_{k'}(\boldsymbol{R})\left\{\int d\boldsymbol{r}\psi^*_{k'}(\boldsymbol{r},\boldsymbol{R})\left(\frac{\hbar^2\nabla_i^2}{2m_i}\psi_k(\boldsymbol{r},\boldsymbol{R})\right)\right\}\Phi_k(\boldsymbol{R}). \tag{2.14}$$

The ratio of m_i to M_I is very small since electrons are much lighter than the nuclei by three orders of magnitude. Hence, the first term in equation (2.11) can easily be neglected. The

second term in equation (2.11) is as follows:

$$
\begin{aligned}
& -\sum_I \int d\boldsymbol{r}d\boldsymbol{R}\frac{\hbar^2}{2M_I}\psi^*_{k'}(\boldsymbol{r},\boldsymbol{R})\Phi^*_{k'}(\boldsymbol{R})\Big\{2\left(\nabla_I\psi_k(\boldsymbol{r},\boldsymbol{R})\right)\left(\nabla_I\Phi_k(\boldsymbol{R})\right)\Big\} \\
= & -\sum_I \frac{\hbar^2}{2M_I}\int d\boldsymbol{R}\Phi^*_{k'}(\boldsymbol{R})2\Big\{\int d\boldsymbol{r}\psi^*_{k'}(\boldsymbol{r},\boldsymbol{R})\left(\nabla_I\psi_k(\boldsymbol{r},\boldsymbol{R})\right)\Big\}\left(\nabla_I\Phi_k(\boldsymbol{R})\right). \qquad (2.15)
\end{aligned}
$$

At this point, the real part of the integral with respect to $\{\mathbf{r}\}$ is zero:

$$
\begin{aligned}
Re\left[\int d\boldsymbol{r}\psi^*_{k'}(\boldsymbol{r},\boldsymbol{R})\left(\nabla_I\psi_k(\boldsymbol{r},\boldsymbol{R})\right)\right] &= \frac{1}{2}Re\int d\boldsymbol{r}\Big\{\psi^*_{k'}(\boldsymbol{r},\boldsymbol{R})\left(\nabla_I\psi_k(\boldsymbol{r},\boldsymbol{R})\right)+\{\psi^*_{k'}(\boldsymbol{r},\boldsymbol{R})\left(\nabla_I\psi_k(\boldsymbol{r},\boldsymbol{R})\right)\}^*\Big\} \\
&= \frac{1}{2}Re\int d\boldsymbol{r}\Big\{\psi^*_{k'}(\boldsymbol{r},\boldsymbol{R})\left(\nabla_I\psi_k(\boldsymbol{r},\boldsymbol{R})\right)+\psi_k(\boldsymbol{r},\boldsymbol{R})\left(\nabla_I\psi_k(\boldsymbol{r},\boldsymbol{R})\right)^*\Big\} \\
&= \frac{1}{2}\Big\{\nabla_I\int d\boldsymbol{r}\psi_k(\boldsymbol{r},\boldsymbol{R})\psi^*_{k'}(\boldsymbol{r},\boldsymbol{R})\Big\} \\
&= \frac{1}{2}\{\nabla_I N_e\} \\
&= 0. \qquad (2.16)
\end{aligned}
$$

As shown in Eqs. (2.14) and (2.16), the diagonal matrix element of the second term in equation (2.9) can be avoided.

2.2 Density Functional Theory

In this section, we shall explain density functional theory (DFT) formalism for total energy electronic structure calculations carried out in this dissertation. First-principles calculation based on density functional theory has long been recognized as a practical means of providing important microscopic information for physical properties of materials on the basis of quantum theory. Presently, DFT is in premier status among various theoretical methodologies for clarification and prediction of phenomena in condensed matters. The basic idea was introduced by Hohenberg, Kohn and Sham in the 1960s. The goal as shown by Hohenberg and Kohn [52] is to find the exact ground-state density and total energy of a system of N interacting electrons in an external potential without an explicit reference to the many-body wavefunction. The electrons are assumed to interact pairwise via Coulomb interaction. The ultimate aim of DFT calculation is minimization of an energy functional $E[n]$ with respect to the density n. Furthermore, the nontrivial part of this

functional is universal, that is, it has the same form for all physical systems. Kohn and Sham also demonstrated that it is possible to convert the many-electron problem to an exactly equivalent set of self-consistent one-electron equations [53]. In the subsequent subsections, we shall explain DFT formalism. Equations are in atomic unit, i.e., the fundamental constant $\hbar$, e^2 and m_e are set to unity.

2.2.1 Density variational principle

Let us consider a system of interacting electrons whose Hamiltonian $\hat{H}$ is defined as:

$$\begin{aligned}\hat{H} &= \sum_i \left(-\frac{1}{2}\nabla_i^2\right) + \frac{1}{2}\sum_{i\neq j}\frac{1}{|\boldsymbol{r}_i - \boldsymbol{r}_j|} + \sum_i \sum_I \upsilon_{ext,I}\left(\boldsymbol{r}_i - \boldsymbol{R}_I\right) \\ &= \sum_i \left(-\frac{1}{2}\nabla_i^2\right) + \frac{1}{2}\sum_{i\neq j}\frac{1}{|\boldsymbol{r}_i - \boldsymbol{r}_j|} + \sum_i \upsilon_{ext}\left(\boldsymbol{r}_i\right) \\ &= \hat{T} + \hat{U} + \hat{V}_{ext}, \end{aligned} \tag{2.17}$$

where $\hat{T}$, $\hat{U}$ and $\hat{V}_{ext}$ are the electron kinetic energy term, the electron-electron interaction term and the electron-nucleus interaction term (external potential term). Equation (2.17) is in atomic unit.

We first introduce the electron density operator, $\hat{n}(\boldsymbol{r})$:

$$\hat{n}(\boldsymbol{r}) = \sum_i \delta\left(\boldsymbol{r} - \boldsymbol{r}_i\right). \tag{2.18}$$

The many-electron wavefunction $\Psi(\boldsymbol{r}_1, \boldsymbol{r}_2, \cdots, \boldsymbol{r}_N)$, contains a great deal of information. This is because it is a function of many variables, it is also not easy to calculate the wavefunction itself.

Using the density operator, Eq. (2.18), the electron density is written as

$$\begin{aligned} n(\boldsymbol{r}) &= \langle\Psi_i|\,\hat{n}(\boldsymbol{r})\,|\Psi_i\rangle \\ &= \int d\boldsymbol{r}_1 \cdots \Psi^*(\boldsymbol{r}_1, \cdots)\Big\{\sum_i \delta(\boldsymbol{r} - \boldsymbol{r}_i)\Big\}\Psi(\boldsymbol{r}_1, \cdots). \end{aligned} \tag{2.19}$$

In a similar way, the electron-nuclei interaction is expressed as

$$\begin{aligned}
\langle\Psi_i|\,\hat{V}_{ext}\,|\Psi_i\rangle &= \int d\boldsymbol{r}_1\cdots\Psi^*(\boldsymbol{r}_1,\cdots)\Big\{\sum_i \upsilon_{ext}(\boldsymbol{r}_i)\Big\}\Psi(\boldsymbol{r}_1,\cdots)\\
&= \int d\boldsymbol{r}_1\cdots\Psi^*(\boldsymbol{r}_1,\cdots)\Big\{\sum_i \int d\boldsymbol{r}\delta(\boldsymbol{r}-\boldsymbol{r}_i)\upsilon_{ext}(\boldsymbol{r}_i)\Big\}\Psi(\boldsymbol{r}_1,\cdots)\\
&= \int d\boldsymbol{r}\upsilon_{ext}(\boldsymbol{r})\int d\boldsymbol{r}_1\cdots\Psi^*(\boldsymbol{r}_1,\cdots)\Big\{\sum_i \delta(\boldsymbol{r}-\boldsymbol{r}_i)\Big\}\Psi(\boldsymbol{r}_1,\cdots)\\
&= \int d\boldsymbol{r}\upsilon_{ext}(\boldsymbol{r})n(\boldsymbol{r}). \qquad (2.20)
\end{aligned}$$

Hohenberg and Kohn presented the theoretical concept of DFT and the essential result is that, the particle density determines the ground-state properties of the many-body system in contrast to the Schroödinger formulation in which the many-body wavefunction does. Their theory is composed of two theorems with respective collaries. The first theorem states that, if a density $n(\boldsymbol{r})$ is the ground-state density of the hamiltonian $\hat{H}$ with some external or local potential $\upsilon_{ext}(\boldsymbol{r})$, then $\upsilon_{ext}(\boldsymbol{r})$ is uniquely defined up to an additive constant for a system of interacting particles. We prove the above theorem as follows; first we guess two different external potentials $\upsilon^1_{ext}(\boldsymbol{r})$ and $\upsilon^2_{ext}(\boldsymbol{r})$ which gives the same ground state density $n(\boldsymbol{r})$. Their corresponding hamiltonian ($\hat{H}^1$, $\hat{H}^2$), wavefunctions $\Psi^1(\boldsymbol{r}_1,\boldsymbol{r}_2,\cdots,\boldsymbol{r}_N)$, $\Psi^2(\boldsymbol{r}_1,\boldsymbol{r}_2,\cdots,\boldsymbol{r}_N)$ and ground state energies (E^1,E^1) are clearly different. It then follows from the Rayleigh-Ritz variational principle that the inequality

$$\begin{aligned}
E^1 &= \langle\Psi^1|\,\hat{H}^1\,|\Psi^1\rangle < \langle\Psi^2|\,\hat{H}^1\,|\Psi^2\rangle\\
&= \langle\Psi^2|\,\hat{H}^2\,|\Psi^2\rangle + \langle\Psi^2|\,\hat{H}^1-\hat{H}^2\,|\Psi^2\rangle\\
&= E^2 + \int d\boldsymbol{r}\{\upsilon^1_{ext}(\boldsymbol{r})-\upsilon^2_{ext}(\boldsymbol{r})\}n(\boldsymbol{r}), \qquad (2.21)
\end{aligned}$$

is strictly satisfied. Similarly

$$\begin{aligned}
E^2 &= \langle\Psi^2|\,\hat{H}^2\,|\Psi^2\rangle < \langle\Psi^1|\,\hat{H}^2\,|\Psi^1\rangle\\
&= \langle\Psi^1|\,\hat{H}^1\,|\Psi^1\rangle + \langle\Psi^1|\,\hat{H}^2-\hat{H}^1\,|\Psi^1\rangle\\
&= E^1 + \int d\boldsymbol{r}\{\upsilon^2_{ext}(\boldsymbol{r})-\upsilon^1_{ext}(\boldsymbol{r})\}n(\boldsymbol{r}). \qquad (2.22)
\end{aligned}$$

Addition of Eqs. (2.21) and (2.22) follows that:

$$E^1 + E^2 \; < \; E^1 + E^2. \tag{2.23}$$

Hence, the assumption that there exist two different potentials which yield the same ground state density is false. Therefore, the first theorem of Hohenberg and Kohn shows that the external potential $\upsilon_{ext}(\boldsymbol{r})$ uniquely determines the ground state density $n(\boldsymbol{r})$. The first corollary then suggests that the many-body wavefunction for all states are determined given only the ground state density because the hamiltonian is fully determined which means all physical properties are completely determined. This theorem and the corollary replaces the wavefunction $\Psi(\boldsymbol{r}_1, \boldsymbol{r}_2, \cdots, \boldsymbol{r}_N)$ with density $n(\boldsymbol{r})$ to represent the same many-body system.

As discussed above, the ground state energy is expressed as a functional of the ground state density, $n(\mathbf{r})$:

$$E[n(\boldsymbol{r})] \; = \; F[n(\boldsymbol{r})] + \int d\boldsymbol{r} \upsilon_{ext}(\boldsymbol{r}) n(\boldsymbol{r}), \tag{2.24}$$

where $F[n(\boldsymbol{r})]$ is universal in the sense that it refers neither to a specific system nor to the external potential $\upsilon_{ext}(\boldsymbol{r})$ and corresponds to the total kinetic plus electron-electron interaction energy. The functional $F[n(\boldsymbol{r})]$ is considered as the internal energy of the interacting electron system expressed as:

$$F[n(\boldsymbol{r})] \equiv \langle \Psi | \, \hat{T} + \hat{U} \, | \Psi \rangle \, . \tag{2.25}$$

The system of the ground state density $n(\boldsymbol{r})^1$ with external potential $\upsilon^1_{ext}(\boldsymbol{r})$ can be chosen, whose wavefunction is Ψ^1. The total energy functional is equal to the expectation value of the unique ground state.

$$\begin{aligned} E^1 \; &= \; \langle \Psi^1 | \, \hat{H}^1 \, | \Psi^1 \rangle \\ &< \; \langle \Psi^2 | \, \hat{H}^1 \, | \Psi^2 \rangle \; = \; E^2. \end{aligned} \tag{2.26}$$

Equation (2.26) means that, the energy of the ground state density is lower than any other density.

The second theorem of Hohenberg and Kohn is that the ground state energy, E, is obtained by minimization of the energy functional $E[n(\mathbf{r})]$ with respect to the density $n(\mathbf{r})$. For the trial density $\tilde{n}(\mathbf{r})$, which satisfies $\tilde{n}(\mathbf{r}) > 0$ and $\int d\mathbf{r}\tilde{n}(\mathbf{r}) = N$,

$$E \leqslant E[\tilde{n}(\mathbf{r})]. \tag{2.27}$$

The corollary of the second theorem is that the exact ground state energy and density are deduced only from the energy functional $E[\tilde{n}(\boldsymbol{r})]$. This is because, the ground state energy is found by searching the global minimum value of the energy functional with variation of the density. The Hohenberg and Kohn formulation is based on the treatment of the ground state density with some external potential which is called V-representability. Also, there is the case that even if the external potential is determined, the ground state density cannot be uniquely specified. For example, all the degenerate ground states density have the same external potential in a system. Besides, the density which is determined by some external potential is generally unknown.

Here, we show that the minimization can be performed with respect to the electron density, instead of the wavefunction. The crucial step in the formulation of DFT is the conversion of the familiar Rayleigh-Ritz variational principle of the quantum mechanical wavefunction into a variational principle of the density. This conversion is most elegantly accomplished by means of the constrained search algorithm. According to the Rayleigh-Ritz principle the ground-state energy, E_0, is found by minimizing the expectation value of the hamiltonian with respect to the wavefuncion Ψ, as follows:

$$\begin{aligned} E_0 &= \min_{\{\Psi\}} \langle\Psi|\, \hat{H}\, |\Psi\rangle \\ &= \min_{\{\Psi\}} \langle\Psi|\, \hat{T} + \hat{U} + \hat{V}_{ext}\, |\Psi\rangle\,. \end{aligned} \tag{2.28}$$

where Ψ must be an antisymmetric under interchange of two electrons because electrons are fermions and satisfy the boundary conditions appropriate to the system under study.

The search for the wavefunctions that minimizes equation (2.28) can be accomplished in two steps. First, we pick a density $n(\boldsymbol{r})$ and minimize equation (2.28) within the subset of wavefunctions that yield this density. Any reasonable density, must of course, be positive and continuous, and add up to the total number of electrons in the system, $\int n(\boldsymbol{r})d\boldsymbol{r} = N$,

the N-representable condition is satisfied because antisymmetric wavefunction is used. This gives the constraint search mnimum. It should be noted that Hohenberg and Kohn worked in the space V-reprentable densities, i.e., those that can be realized for some external potential which is a subspace of N-representable densities. Second step, we perform the minimization with respect to $n(\boldsymbol{r})$ as:

$$\begin{aligned}\min_{\{\Psi\}} \langle\Psi|\,\hat{T}+\hat{U}+\hat{V}_{ext}\,|\Psi\rangle &= \min_{n}\left\{\min_{\{\Psi\}\longrightarrow n}\langle\Psi|\,\hat{T}+\hat{U}+\hat{V}_{ext}\,|\Psi\rangle\right\}\\ &= \min_{n}\left\{\min_{\{\Psi\}\longrightarrow n}\langle\Psi|\,\hat{T}+\hat{U}\,|\Psi\rangle+\int d\boldsymbol{r}\upsilon_{ext}(\boldsymbol{r})n(\boldsymbol{r}\right\}. \qquad (2.29)\end{aligned}$$

The notation $_{\{\Psi\}\longrightarrow n}$ indicates that the search for the minimum is restricted to antisymmetric wave function which yield the density $n(\boldsymbol{r})$. Levy and Lieb [54] gave another definition of a universal functional based on the density obtained from the many-body wavefunctions satisfying the N-repsentability condition by the first term of right-hand side of Eq.(2.29) as:

$$F[n(\boldsymbol{r})] = \min_{\{\Psi\}\longrightarrow n}\langle\Psi|\,\hat{T}+\hat{U}\,|\Psi\rangle\,, \qquad (2.30)$$

Finally, by using the universal functional, $F[n(\boldsymbol{r})]$, the ground state energy is now expressed as:

$$E_0 = \min_{n}\left\{F[n(\boldsymbol{r})]+\int d\boldsymbol{r}\upsilon_{ext}(\boldsymbol{r})n(\boldsymbol{r}\right\} \qquad (2.31)$$

$$= \min_{n} E[n(\boldsymbol{r})]. \qquad (2.32)$$

Looking back at what we have just done we see that the complexity of the original Rayleigh-Ritz variational principle has been absorbed in the definition of the functional. Levy and Lieb reformulation lead to the guideline of minimization of energy functional for real practical application.

2.2.2 The Kohn-Sham Equation

The minimum principle of equation (2.31) offers an elegant approach to the problem of calculating the ground-state density and energy, but the functional $F[n(\boldsymbol{r})]$ is not known. It is very hard, if not impossible to calculate $F[n(\boldsymbol{r})]$ exactly and the obvious possibility is to embark immediately on an effort to find a suitable approximation. Kohn and

Sham came up with an ingenious strategy to accomplish this. The ground-state density of the interacting system, they argued, can be represented as the ground state density of a non-interacting system in some effective potential. This is of course, an unproven assumption. However, the Hohenberg-Kohn theorem guarantees that this potential, if it exists, is unique. This means the effective potential in the interacting and non-intereacting systems are not the same. Kohn and Sham introduced a virtual system, in which electrons do not interact with each other under an effective potential υ_{eff} and are described by the independent-single particle equation as:

$$\left\{ -\frac{1}{2}\nabla^2 + \upsilon_{eff}(\boldsymbol{r}) \right\} \psi_i(\boldsymbol{r}) = \varepsilon_i \psi_i(\boldsymbol{r}), \tag{2.33}$$

$$n(\boldsymbol{r}) = \sum_{occupied} |\psi_i(\boldsymbol{r})|^2, \tag{2.34}$$

where ψ_i and ε_i are the single-particle wavefunction (Kohn-Sham wavefunction) and the eigenvalue of the virtual system and the label i denotes each Kohn-Sham state. The above equations are called the Kohn-Sham equations. They have also decomposed $F[n(\boldsymbol{r})]$ into three parts:

$$F[n(\boldsymbol{r})] = T_s[n(\boldsymbol{r})] + U[n(\boldsymbol{r})] + E_{xc}[n(\boldsymbol{r})]. \tag{2.35}$$

The first term $T_s[n(\boldsymbol{r})]$ is the single particle non-interacting kinetic energy functional defined as:

$$T_s[n(\boldsymbol{r})] = \sum_i \langle \psi_i | -\frac{1}{2}\nabla^2 | \psi_i \rangle \tag{2.36}$$

$$= \sum_i \left\{ \varepsilon_i - \int d\boldsymbol{r} \upsilon_{eff}(\boldsymbol{r}) n(\boldsymbol{r}) \right\}. \tag{2.37}$$

The second term $U[n(\boldsymbol{r})]$ is the Hartree electrostatic interaction

$$U[n(\boldsymbol{r})] = \frac{1}{2} \int d\boldsymbol{r} \int d\boldsymbol{r}' \frac{n(\boldsymbol{r}) n(\boldsymbol{r}')}{|\boldsymbol{r} - \boldsymbol{r}'|}. \tag{2.38}$$

The last term $E_{xc}[n(\boldsymbol{r})]$ is the exchange-correlation energy including everything else omitted from the first two terms.

By the decomposition of equation Eq. (2.35), the Kohn-Sham total-energy functional

becomes:

$$E[n(\boldsymbol{r}),\{\boldsymbol{R_I}\}] \;=\; \sum_i \langle\psi_i| -\frac{1}{2}\nabla^2 |\psi_i\rangle \;+\; \int d\boldsymbol{r} v_{ext}(\boldsymbol{r}) n(\boldsymbol{r}) + \frac{1}{2}\int d\boldsymbol{r}\int d\boldsymbol{r}' \frac{n(\boldsymbol{r})n(\boldsymbol{r}')}{|\boldsymbol{r}-\boldsymbol{r}'|} + E_{xc}[n(\boldsymbol{r})], \tag{2.39}$$

according to Eq. (2.31). Usually, the system consists of electrons and nuclei (or ions). The total energy functional including the nuclei is thus expressed us:

$$E[n(\boldsymbol{r}),\{\boldsymbol{R_I}\}] \;=\; \sum_i \langle\psi_i| -\frac{1}{2}\nabla^2 |\psi_i\rangle \;+\; \int d\boldsymbol{r} v_{ion}(\boldsymbol{r}) n(\boldsymbol{r}) \;+\; \frac{1}{2}\int d\boldsymbol{r}\int d\boldsymbol{r}' \frac{n(\boldsymbol{r})n(\boldsymbol{r}')}{|\boldsymbol{r}-\boldsymbol{r}'|} + E_{xc}[n(\boldsymbol{r})] \;+\; \sum_{I\neq J}\frac{Z_I Z_J}{|\mathbf{R}_I-\mathbf{R}_J|}, \tag{2.40}$$

where $v_{ion}(\boldsymbol{r})$ is the electron-ion potential same as $v_{ext}(\boldsymbol{r})$ and the last term is the Coulomb energy interactions among the nuclei with $\{Z_I\}$ at positions $\{\boldsymbol{R_I}\}$. From the theorems previously discussed, we can obtain the ground state energy of any system by minimizing the energy with respect to the electron density $n(\boldsymbol{r})$. The variation of the total-energy $E[n(\boldsymbol{r})]$ with respect to the density as written in Eq. (2.40) is expressed as:

$$\delta E[n(\boldsymbol{r})] \;=\; \delta T_s[n(\boldsymbol{r})] \;+\; \int d\boldsymbol{r} v_{ion}(\boldsymbol{r})\delta n(\boldsymbol{r}) \;+\; \int d\boldsymbol{r}\int d\boldsymbol{r}'\delta n(\boldsymbol{r})\frac{n(\boldsymbol{r}')}{|\boldsymbol{r}-\boldsymbol{r}'|} + \int d\boldsymbol{r}\frac{\delta E_{xc}[n(\boldsymbol{r})]}{\delta n(\boldsymbol{r})}\delta n(\boldsymbol{r}). \tag{2.41}$$

If we substitute equation (2.41) into (2.37) accordingly, we obtain the following equation.

$$\delta E[n(\boldsymbol{r})] \;=\; \sum_i \delta\varepsilon_i \;-\; \int d\boldsymbol{r}\delta v_{eff}(\boldsymbol{r}) n(\boldsymbol{r}) \;-\; \int d\boldsymbol{r} v_{eff}(\boldsymbol{r})\delta n(\boldsymbol{r}) + \int d\boldsymbol{r} v_{ion}(\boldsymbol{r})\delta n(\boldsymbol{r}) \;+\; \int d\boldsymbol{r}\int d\boldsymbol{r}'\delta n(\boldsymbol{r})\frac{n(\boldsymbol{r}')}{|\boldsymbol{r}-\boldsymbol{r}'|} \;+\; \int d\boldsymbol{r}\frac{\delta E_{xc}[n(\boldsymbol{r})]}{\delta n(\boldsymbol{r})}\delta n(\boldsymbol{r}). \tag{2.42}$$

The Kohn-Sham equation under effective potential $v_{eff} + \delta v_{eff}$ is expressed as:

$$\left\{-\frac{1}{2}\nabla^2 \;+\; v_{eff}(\boldsymbol{r}) \;+\; \delta v_{eff}(\boldsymbol{r})\right\}(\psi_i(\boldsymbol{r}) \;+\; \delta\psi_i(\boldsymbol{r})) \;=\; (\varepsilon_i \;+\; \delta\varepsilon_i)\,(\psi_i(\boldsymbol{r}) + \delta\psi_i(\boldsymbol{r}))\,. \tag{2.43}$$

Further simplification yields the equation below:

$$\left\{ -\frac{1}{2}\nabla^2 \; + \; \upsilon_{eff}(\boldsymbol{r}) \; + \; \delta\upsilon_{eff}(\boldsymbol{r}) \right\} \delta\psi_i(\boldsymbol{r}) \; + \; \delta\upsilon_{eff}(\boldsymbol{r})\psi_i(\boldsymbol{r}) \; = \; \varepsilon_i\delta\psi_i(\boldsymbol{r}) \; + \; \delta\varepsilon_i \left(\psi_i(\boldsymbol{r}) \; + \; \delta\psi_i(\boldsymbol{r})\right). \tag{2.44}$$

Considering only the first-order variations, we obtain

$$\left\{ -\frac{1}{2}\nabla^2 \; + \; \upsilon_{eff}(\boldsymbol{r}) \right\} \delta\psi_i(\boldsymbol{r}) + \delta\upsilon_{eff}(\boldsymbol{r})\psi_i(\boldsymbol{r}) \; = \varepsilon_i\delta\psi_i(\boldsymbol{r}) \; + \; \delta\varepsilon_i\psi_i(\boldsymbol{r}), \tag{2.45}$$

which can be re-written as

$$\delta\upsilon_{eff}(\boldsymbol{r})\psi_i(\boldsymbol{r}) \; = \; \delta\varepsilon_i\psi_i(\boldsymbol{r}). \tag{2.46}$$

At this juncture, we multiply both sides of Eq. (2.46) with $\psi_i^*(\boldsymbol{r})$ and integrate with respect to $\boldsymbol{r}$,

$$\int d\boldsymbol{r}\psi_i^*(\boldsymbol{r})\delta\upsilon_{eff}(\boldsymbol{r})\psi_i(\boldsymbol{r}) \; = \; \int d\boldsymbol{r}\psi_i^*(\boldsymbol{r})\delta\varepsilon_i\psi_i(\boldsymbol{r}). \tag{2.47}$$

This follows that equation (2.47) becomes:

$$\int d\boldsymbol{r}\delta\upsilon_{eff}(\boldsymbol{r})|\psi_i(\boldsymbol{r})|^2 \; = \; \int d\boldsymbol{r}\delta\varepsilon_i|\psi_i(\boldsymbol{r})|^2 \; = \; \delta\varepsilon_i. \tag{2.48}$$

The summation of Eq. (2.48) with respect to the suffix i is given by

$$\begin{aligned} \int d\boldsymbol{r}\delta\upsilon_{eff}(\boldsymbol{r})\left\{ \sum_i |\psi_i(\boldsymbol{r})|^2 \right\} \; &= \; \sum_i \delta\varepsilon_i, \\ \int d\boldsymbol{r}\delta\upsilon_{eff}(\boldsymbol{r})n(\boldsymbol{r}) \; &= \; \sum_i \delta\varepsilon_i. \end{aligned} \tag{2.49}$$

Substituting Eq. (2.49) into Eq. (2.42)

$$\begin{aligned} \delta E[n(\boldsymbol{r})] \; &= \; -\int d\boldsymbol{r}\upsilon_{eff}(\boldsymbol{r})\delta n(\boldsymbol{r}) \\ &+ \int d\boldsymbol{r}\upsilon_{ion}(\boldsymbol{r})\delta n(\boldsymbol{r}) \; + \; \int d\boldsymbol{r}\int d\boldsymbol{r}'\delta n(\boldsymbol{r})\frac{n(\boldsymbol{r}')}{|\boldsymbol{r}-\boldsymbol{r}'|} \; + \; \int d\boldsymbol{r}\frac{\delta E_{xc}[n(\boldsymbol{r})]}{\delta n(\boldsymbol{r})}\delta n(\boldsymbol{r}) \\ &= \; \int d\boldsymbol{r}\delta n(\boldsymbol{r})\left\{ -\upsilon_{eff}(\boldsymbol{r}) \; + \; \upsilon_{ion}(\boldsymbol{r}) \; + \; \int d\boldsymbol{r}'\frac{n(\boldsymbol{r}')}{|\boldsymbol{r}-\boldsymbol{r}'|} \; + \; \frac{\delta E_{xc}[n(\boldsymbol{r})]}{\delta n(\boldsymbol{r})} \right\}. \end{aligned} \tag{2.50}$$

To satisfy the variational condition that $\delta E[n(\boldsymbol{r})]$ is equal to zero under the condition

$\int d\boldsymbol{r}\delta n(\boldsymbol{r}) = 0$, the effective potential $\upsilon_{eff}(\boldsymbol{r})$ is given by

$$\upsilon_{eff}(\boldsymbol{r}) = \upsilon_{ion}(\boldsymbol{r}) + \int d\boldsymbol{r}' \frac{n(\boldsymbol{r}')}{|\boldsymbol{r} - \boldsymbol{r}'|} + \frac{\delta E_{xc}[n(\boldsymbol{r})]}{\delta n(\boldsymbol{r})}. \tag{2.51}$$

Therefore, substituting Eq. (2.51) into Eq. (2.33) we obtain:

$$\left\{ -\frac{1}{2}\nabla^2 + \upsilon_{ion}(\boldsymbol{r}) + \upsilon_H(\boldsymbol{r}) + \upsilon_{xc}(\boldsymbol{r}) \right\} \psi_i(\boldsymbol{r}) = \varepsilon_i \psi_i(\boldsymbol{r}), \tag{2.52}$$

in more compact form

$$H_{KS}\psi_i(\boldsymbol{r}) = \varepsilon_i \psi_i(\boldsymbol{r}), \tag{2.53}$$

where $\upsilon_H(\boldsymbol{r})$ is the Hartree potential due to the electrons represented as

$$\upsilon_H(\boldsymbol{r}) = \int d\boldsymbol{r}' \frac{n(\boldsymbol{r}')}{|\boldsymbol{r} - \boldsymbol{r}'|}. \tag{2.54}$$

The exchange-correlation potential, $\upsilon_{xc}(\boldsymbol{r})$, is given formally by the functional derivative of the exchange-correlation energy $E_{xc}[n(\boldsymbol{r})]$ as

$$\upsilon_{xc}(\boldsymbol{r}) = \frac{\delta E_{xc}[n(\boldsymbol{r})]}{\delta n(\boldsymbol{r})}. \tag{2.55}$$

Equation (2.52) is the so called Kohn-Sham equations which must be solved self-consistently, leading to the solution of single-particle Kohn-Shame states. The occupied Kohn-Sham wavefunctions lead to electron density that produces the electronic potential and this potential should be the same as the potential used to construct the equation. Again, equation (2.52) contains the exchange-correlatin potential. If this term were known exactly, then taking the functional derivative with respect to the density would produce an exchange-correlation potential that included the effects of exchange and correlation exactly. Until now, the exact functional form is a big unknown and thus approximations are usually adopted. The simplest approximation methods describing the exchange-correlation energy is the local density approximation (LDA) proposed by Hohenberng-Kohn and appropriate for sufficiently slowly varying density and that the correlation-energy functional is purely local.

$$E_{xc}^{LDA}[n(\boldsymbol{r})] = \int d\boldsymbol{r}\varepsilon_{xc}(n(\boldsymbol{r}))n(\boldsymbol{r}), \tag{2.56}$$

wherer $\varepsilon_{xc}(\boldsymbol{r})$, is the exchange-correlation energy per electron in a homogenous electron

gas

$$\frac{\delta E_{xc}[n(\boldsymbol{r})]}{\delta n(\boldsymbol{r})} = \frac{d[n(\boldsymbol{r})\varepsilon_{xc}(\boldsymbol{r})]}{dn(\boldsymbol{r})}. \tag{2.57}$$

Ceperley and Alder [55] have calculated the energy of a uniform electron gas over a wide range of densities. They used Quantum Monte Carlo simulation techniques to sample a correlated wavefunction for electrons in a finite volume subject to periodic boundary conditions and extrapolated the energy per electron to infinite volume. Perdew and Zunger [56] have parmaterized the results of Ceperley-Alder by interpolation formular to link exact results for the exchange-correlation energy of high-density electron gas and calculations of intermediate and low-density electron gas. For an upolalrized electron gas, the exchange-correlation energy is given as:

$$\varepsilon_{xc} = \varepsilon_x + \varepsilon_c, \tag{2.58}$$

$$\varepsilon_x = -\frac{0.4582}{r_s}, \tag{2.59}$$

$$\varepsilon_c = \frac{-0.1432}{1 + 1.0529\sqrt{r_s} + 0.3334 r_s} \qquad (r_s) \geqslant 1, \tag{2.60}$$

$$= -0.0480 + 0.0311 ln r_s - 0.0116 r_{r_s} + 0.0020 r_s ln r_s \qquad (r_s) < 1, \tag{2.61}$$

where ε_x and ε_c are the exchange and correlation terms respectively, and the quantity r_s is the radius of a sphere whose volume is the effective volume of an electron. We can obtain the exchange-correlation potential as:

$$n(\boldsymbol{r}) = \frac{3}{4\pi r_s^3}. \tag{2.62}$$

By subtituting Eq. (2.56) into the exchange-correlation potential in Eq. (2.55) we obtain the following expression

$$\begin{aligned} \upsilon_{xc}(\boldsymbol{r}) &= \frac{\delta E_{xc}[n(\boldsymbol{r})]}{\delta n(\boldsymbol{r})}, \\ &= \varepsilon_{xc}\left(n(\boldsymbol{r})\right) + n(\boldsymbol{r})\frac{d\varepsilon_{xc}(n(\boldsymbol{r}))}{dn(\boldsymbol{r})}. \end{aligned} \tag{2.63}$$

Eq. (2.63) means that the exchange-correlation functional can be represented by the local energy functional $\varepsilon_{xc}\left(n(\boldsymbol{r})\right)$. That is, supposing the homogenous electrons gas of density $n(\boldsymbol{r})$ distributes at each point r, the local energy functional should be replaced with that of the homogenous electron gas $\varepsilon_{xc}^{hom}\left(n(\boldsymbol{r})\right)$.

More recently, generalized gradient approximations (GGA) has been proposed and the exchange-correlation energy is expressed as a functional of the density gradient in addition to the density

$$E_{xc}^{GGA}[(n(\boldsymbol{r})] \;=\; \int d\boldsymbol{r} f\left(n(\boldsymbol{r}), \nabla(\boldsymbol{r})\right), \tag{2.64}$$

where f is a parameterized analytic function.

2.2.3 Hellmann-Feynman force

Method to calculate the forces acting on nuclei is described in this section. Total energy is expressed as a functional with respect to the wavefunctions, $\{\psi\}$, and the position of nuclei $\{\mathbf{R}\}$:

$$E\left[\{\psi\}, \{\mathbf{R}\}\right]. \tag{2.65}$$

When each ψ_i is an eigenstate of the Hamiltonian, H, the total differentiation of the total energy with respect to the position of a nucleus, $\mathbf{R_I}$, gives the real physical force on the nucleus [57, 58]. The force acting on ion $\mathbf{F_I}$, is minus the total differentiation of the total energy of a system with respect to the position of a nucleus is written as:

$$\mathbf{F}_I \;=\; -\frac{dE[\{\psi_i\}, \{\mathbf{R}_I\}]}{d\mathbf{R}_I} \tag{2.66}$$

$$\;=\; -\frac{\partial E}{\partial \mathbf{R}_I} \;-\; \sum_i \int d\boldsymbol{r} \left[\frac{\delta E}{\delta \psi_i(\boldsymbol{r})} \frac{\delta \psi_i(\boldsymbol{r})}{\delta \mathbf{R}_I} \;+\; \frac{\delta E}{\delta \psi_i^*(\boldsymbol{r})} \frac{\delta \psi_i^*(\boldsymbol{r})}{\delta \mathbf{R}_I} \right]. \tag{2.67}$$

The total energy of the electron system is given as:

$$E[n(\boldsymbol{r})] \;=\; -\frac{1}{2} \sum_i \int d\boldsymbol{r} \psi_i^*(\boldsymbol{r}) \nabla^2 \psi_i(\boldsymbol{r}) \;+\; \int d\boldsymbol{r} \upsilon_{ion}(\boldsymbol{r}) n(\boldsymbol{r}) + \frac{1}{2} \int d\boldsymbol{r} \int d\boldsymbol{r}' \frac{n(\boldsymbol{r}) n(\boldsymbol{r}')}{|\boldsymbol{r} - \boldsymbol{r}'|}$$
$$+ E_{xc}[n(\boldsymbol{r})]. \tag{2.68}$$

The variation of the total energy of an electron system Eq. (2.68) with respect to ψ_i^*, is given by:

$$\frac{\delta E}{\delta \psi_i^*} = \left\{ -\frac{1}{2}\nabla^2 + \int d\boldsymbol{r}' \frac{n(\boldsymbol{r}')}{|\boldsymbol{r}-\boldsymbol{r}'|} + \frac{\delta E_{xc}[n(\boldsymbol{r})]}{\delta n(\boldsymbol{r})} + \upsilon_{ion}(\boldsymbol{r}) \right\} \psi_i(\boldsymbol{r}) \tag{2.69}$$

$$= \left\{ -\frac{1}{2}\nabla^2 + \upsilon_{eff}(\boldsymbol{r}) \right\} \psi_i(\boldsymbol{r})$$

$$= H_{KS}\psi_i, \tag{2.70}$$

where H_{KS} is the Kohn-Sham Hamiltonian for the effective potential as shown in Eq. (2.52). Now, we can re-write Eq. (2.67) by substituting (2.70) as:

$$\mathbf{F}_I = -\frac{\partial E}{\partial \mathbf{R}_I} - \left\{ \langle \psi_i | \hat{H}_{KS} | \frac{d\psi_i}{d\mathbf{R}_I} \rangle + \langle \frac{d\psi_i}{d\mathbf{R}_I} | \hat{H}_{KS} | \psi_i \rangle \right\}. \tag{2.71}$$

This is called Hellmann-Feynman force and expressed as:

$$-\frac{\partial E}{\partial \mathbf{R}_I} = \int d\boldsymbol{r} n(\boldsymbol{r}) \frac{\partial \upsilon_{ion}(\boldsymbol{r})}{\partial \mathbf{R}_I} - \frac{\partial E_{II}}{\partial \mathbf{R}_I}, \tag{2.72}$$

where

$$E_{II} = \sum_{I \neq J} \frac{Z_I Z_J}{|\mathbf{R}_I - \mathbf{R}_J|}, \tag{2.73}$$

is the nucleus-nucleus interactions. If a complete basis set is used, the second term in (2.71) becomes zero and then Hellmann-Feynman force coincides with the force on the nuclei. Otherwise, if some basis sets are introduced to represent the eigenstates, i.e.,

$$\psi_i(\mathbf{r}) = \sum_{\mu} C_{i\mu}\chi_\mu, \tag{2.74}$$

where χ_μ denotes the basis set, Eq. (2.71) is expressed as:

$$\mathbf{F}_I = -\frac{\partial E}{\partial \mathbf{R}_I} - \sum_i \left\{ \sum_{\mu\mu'} C^*_{i\mu'} C_{i\mu} \left(\left\langle \frac{d\chi_{\mu'}}{d\mathbf{R_I}} \middle| H - \varepsilon_i \middle| \chi_\mu \right\rangle + \left\langle \chi_{\mu'} \middle| H - \varepsilon_i \middle| \frac{d\chi_\mu}{d\mathbf{R_I}} \right\rangle \right) \right\}. \tag{2.75}$$

The second term of (2.75) contains the derivative of the basis set with respect to the positions of the nuclei. The contribution of this term to the force on the nuclei usually referred to as the Pulay force. If the basis functions do not depend on the positions of nuclei, the Pulay force becomes zero.

2.3 Total-Energy Electronic-Structure Calculations

In this section, we shall describe the method of performing total-energy electronic structure calculations based on DFT. As outlined in the previous section, DFT is a powerful scheme to reveal atom-scale mechanisms for a variety of phenomena in real materials. For example, it provides the theoretical framework for obtaining the ground state total energies, the ground state electronic charge densities and optimized atomic structures. In order to perform actual practical DFT calculations, several numerical methods are employed. The most important among them is the basis set used to expand the Kohn-Sham single-particle orbitals. This is because it determines the construction of the Hamiltonian matrix and its operations consist of selection of the exchange-correlation potential and external potential terms. Although there are several basis set such as Slater-type basis functions or Gaussian-type basis functions, Plane-wave basis is one of the most useful basis sets to facilitate DFT calculations. However, a similar scheme exists in which functions are not expanded in a basis set, but are sampled on a real-space mesh. The mesh is commonly chosen to be uniform although other options are possible. The calculations carried out in the present thesis are based on the real space formalism in reference to the implementation of the real space density functional theory (RSDFT) code developed in our group [59]. In the real-space approach, ionic potentials are replaced by smoother pseudopotentials. The Schrödinger-type quantum mechanical equations are discretized on three-dimensional spatial grids and solved by treating them as finite-difference (FD) equations. In this section, we begin the discussion by introducing the real-space grid method of Kohn-Sham energy functional, describe the pseudopotential scheme and electronic structure calculations based on the real-space scheme.

2.3.1 Real-space grid scheme

The standard approach of doing total-energy electronic-structure calculations are based on density-functional theory. The method is used to provide theoretical framework for interpreting experimental results and even to accurately predict properties before experimental data are made available. The usual way to solve the Kohn-Sham equation which is a variational equation of the total energy with respect to the electron density is to use a basis set. In the real-space formulation grids (in real space) are introduced instead of

basis sets and wavefunctions, electron density and potentials are computed on each grid point which are very simple to visualize. Accuracy of the computation is guaranteed by systematically decreasing the separation between the grid points. This corresponds to the systematic increase of the number of plane waves in the plane-wave basis set approach and thereby provides practically accurate solutions of Kohn-Sham equations.

Although the traditional plane-wave methods are highly successful, the method is constrained by the necessity of performing fast Fourier transforms (FFT's) between real and reciprocal spaces. One of the several advantages in real-space formulation is its being almost free from the spell of FFT. While FFT's maybe implemented in a highly efficient manner on traditional vector supercomputers, the current trend in supercomputer design is massively parallel multi-core architectures. It is difficult to implement an efficient FFT algorithms on such machines due to the required long-range routine communications tasks among all processors so that the large-scale calculations are indeed formidable. Real-space methods are inherently local, and therefore do not lead to large overhead burden in communication. The choice to overcome this numerical difficulty is to compute all the necessary quantities in real-space, for example it is unnecessary to use FFT in Hamiltonian operations. In calculations of long-range Hartree potentials, it may be useful to use FFT. Even for the calculations of Hartree potentials, solving Poisson equations in real space may be an alternative to massive parallel computations. In the present version of the RSDFT code, we use FFT only in calculating Hartree potentials. This makes the scheme almost FFT-free and the efficiency of the computation is expected to be high.

The scaling of several critical parts of large calculations is improved from $O(N^2 log_2 N)$ in a plane-wave representation to $O(N^2)$ where N is the number of atoms. Furthermore, preconditioning and convergence acceleration are most effectively carried out in real space. The real-space formulation is required for an efficient implementation of $O(N)$ electronic structure methods in which computational work require scales linear with the number of atoms. The method imposes a localization constraint on the electronic orbital or the electronic charge density, which eliminates the $O(N^3)$ orthogonalization step.

Another advantage in real-space formulation is the flexibility to treat boundary conditions of wavefunctions. In plane-wave basis set approach, supercell models where all electrons wavefunctions satisfy periodic boundary conditions are imperative. The real-space approach is capable of treating cluster models as well as supercell models in prin-

ciple. In this formalism, one can study a finite system, a molecule or a cluster without the need of a supercell, simply by imposing that the wavefunctions are zero at a surface far enough from the system. In this way, an infinite system, a polymer, a surface or bulk material can be studied by imposing the appropriate cyclic boundary conditions [61–63].

In RSDFT formulation, the kinetic energy operator is represented by the high-order finite difference operator using values of corresponding functions at nearby grid points. The order of the finite-difference formula suitable for practical computations is linked to a choice of the spacing of grid points. Another big advantage of this approach is that the potential operator is diagonal and that the Hartree potential is evaluated via solving the Poisson's equations rather than the direct integration.

The Hartree potential in the integral form is given by

$$\upsilon_H(\boldsymbol{r}) \;=\; \int d\boldsymbol{r}' \frac{n(\boldsymbol{r}')}{|\boldsymbol{r}-\boldsymbol{r}'|}, \tag{2.76}$$

or in the differential form also known as Poisson equation is given as

$$\nabla^2 \upsilon_H(\boldsymbol{r}) \;=\; -4\pi n(\boldsymbol{r}). \tag{2.77}$$

The Laplacian operator entering the kinetic energy in equation (2.52) and Poison equation (2.77) is discretized at the grid points $\mathbf{r}_i$ by the higher-order difference method. The formula for the discretized Laplacian operators is given by

$$\begin{aligned}
\nabla^2\nabla\psi(x_i,y_i,z_i) \;&=\; \left(\frac{\partial^2}{\partial x^2} \;+\; \frac{\partial^2}{\partial y^2} \;+\; \frac{\partial^2}{\partial z^2}\right)\psi(x_i,y_i,z_i) \\
&\approx \sum_{m_1=-M_d}^{M_d} C_{m_1}\psi(x_i \;+\; m_1H_x, y_i, z_i) \\
&+ \sum_{m_1=-M_d}^{M_d} C_{m_2}\psi\left(x_i, y_i \;+\; m_2H_y, z_i\right) \\
&+ \sum_{m_1=-M_d}^{M_d} C_{m_3}\psi(x_i, y_i, m_3H_z \;+\; z_i),
\end{aligned} \tag{2.78}$$

where H_x, H_y, H_z are the grid spacings in each direction and C_m's are the coefficients of the M_d-order finite difference. The approximation is accurate to order $O(H^{2N_d+2})$ upon the assumption that $\{\psi\}$ can be approximated accurately by a power series in the grid spacing. The numerical errors can adequately be reduced by using higher order-finite difference.

In practice, it is sufficient to use order $M_d = 6$ to avoid errors.

For solids or periodic systems, the unit cell is a parallelepiped which is specified by three lattice vectors $\tilde{\mathbf{a}}_1, \tilde{\mathbf{a}}_2$ and $\tilde{\mathbf{a}}_3$. The spatial grid is defined by dividing each lattice vector by an integer, so that the grid spacing $H_i (i = 1, 2, 3)$ is

$$H_i = \frac{|\tilde{\mathbf{a}}_i|}{M_i},$$

and total number of grid points as $M_L = M_1 M_2 M_3$.

During parallel computation, we divide the target system into blocks, depending on the available resources. Each processor is responsible for each block. Values of required functions in each block are stored in each local memory. Most computations are performed locally on each processor. Communications among different processors occur only when the computation of finite-difference operations and inner products are performed. In the case that we use FFT to compute Hartree potentials, it is convenient to store electron density at all memories and perform FFT at all processors. The computational cost for FFT of the present target system size is of small portion.

Calculations using the real-space grid can be performed on cubic silicon carbide and silicon interface system by using a supercell approach. Although the interface system is periodic in the lateral directions, it has no periodicity in the perpendicular direction. We use the repeating slab model in which thick enough atomic layers are cleaved out from the individual bulk crystals of silicon carbide and silicon and the interface slab made from them. The interface slabs are isolated by thick enough vacuum region from their mirror images. To ensure accuracy of the calculation, the interface slabs and the vacuum regions must be thick enough so that interactions between neighboring sides of the slab and the periodically repeated adjacent surfaces are negligible. Details of the model calculation are discussed in section 2.5.

2.3.2 Pseudopotential

It is well known that most physical and chemical properties of atoms, molecules or solids are dependent on re-arrangement of valence electrons. The core electrons are strongly bound and do not play any meaningful role in the chemical binding of atoms. The pseudo

potential method exploits the importance of valence electrons by replacing the core electrons and the strong ionic potential with a weaker pseudopotential that acts on a set of pseudo wavefunctions rather than the true wavefunctions. In this section, we briefly describe both the conceptual and practical aspects of the pseudoptential method.

The Pseudopotential Concept

The many-electron Schrödinger-type equation can be very much simplified if electrons are divided in two groups: valence electrons and inner core electrons. The electrons in the inner shells are strongly bound and do not play a significant role in the chemical binding of atoms, thus forming with the nucleus an almost inert core. Binding properties are almost completely due to the valence electrons, especially in metals and semiconductors. This separation suggest that the inner electrons can be ignored in a large number of cases, thereby reducing the atom to an ionic core that interacts with the valence electrons. The use of an effective interaction, a pseudopotential that approximates the potential felt by the valence electrons, was first proposed by Fermi in 1934 [60].

Let the exact solutions of the Schrödinger-type equation for the inner core electrons be denoted by $|\psi_c\rangle$ and $|\psi_v\rangle$ those for the valence electrons. Then, the Schrödinger-like equation of the atom can be written as:

$$\hat{H}\,|\psi_n\rangle \;=\; E_n\,|\psi_n\rangle\,, \tag{2.79}$$

with $n \;=\; c, v$. The valence orbitals can be written as the sum of a smooth functions (called the pseudo wavefunction) $|\varphi_v\rangle$ and an oscillating function that results from the orthogonalization of the valence to the inner core orbitals:

$$|\psi_v\rangle \;=\; |\varphi_v\rangle \;+\; \sum_c \alpha_{cv}\,|\psi_c\rangle\,, \tag{2.80}$$

where

$$\alpha_{cv} \;=\; -\langle\psi_c|\varphi_v\rangle\,. \tag{2.81}$$

The pseudo wavefunctions for the smooth orbital $|\varphi_v\rangle$ satisfy a Schrödinger-like equation

with a pseudopotential $\hat{V}^{PP}$:

$$\left(\hat{T} + \hat{V}\right)|\varphi_v\rangle \;=\; E_v\,|\varphi_v\rangle \;+\; \sum_c (E_c - E_v)\,|\psi_c\rangle\,\langle\psi_c|\varphi_v\rangle\,, \tag{2.82}$$

$$\hat{H}\,|\varphi_v\rangle \;=\; E_v\,|\varphi_v\rangle \;+\; \sum_c (E_c - E_v)\,|\psi_c\rangle\,\langle\psi_c|\varphi_v\rangle\,, \tag{2.83}$$

and then

$$\left(\hat{T} + \hat{V}^{PP}\right)|\varphi_v\rangle \;=\; E_v\,|\varphi_v\rangle\,. \tag{2.84}$$

Substitute equation (2.82) into (2.84) yields $\hat{V}^{PP}$as:

$$\hat{V}^{PP} \;=\; \hat{V} \;-\; \sum_c (E_c - E_v)\,|\psi_c\rangle\,\langle\psi_c|\,, \tag{2.85}$$

where $\hat{V}$ is the true potential, in which valence electrons move. The equation (2.85) indicates that there is almost complete cancelation between the large negative potential energy $V(\mathbf{r})$ felt by a valence electron when it is inside the core of an atom, and its large positive kinetic energy which is inherent in the oscillations of its wavefunction $|\psi_c\rangle$.

It is clear that this pseudopotential acts differently on wavefunctions of different angular momentum. In the region near the core, the orthogonalization of the valence orbitals to the strongly oscillating core orbitals forces the valence electrons to have a high kinetic energy (The kinetic energy density is essentially a measure of the curvature of the wavefunctions). The valence electrons feel an effective potential which is the result of screening of the nuclear potential by the core electrons, the Pauli repulsion and exchange-correlation effects between the valence and core electrons. The second term in Eq. (2.85) represents a nonlocal repulsive potential, making the pseudopotential $\hat{V}^{PP}$ much weaker than the true potential $\hat{V}$ in the vicinity of the core. These imply that the pseudo wavefunctions $|\varphi_v\rangle$ will be smooth and will not oscillate in the core region, as desired [63]. The equation (2.85) has a non unique $|\varphi_v\rangle$ [64]

$$\left(\hat{T} \;+\; \hat{V}^{PP}\right)|\varphi'_v\rangle \;=\; E_v\,|\varphi'_v\rangle\,, \tag{2.86}$$

where

$$|\varphi'_v\rangle \;=\; |\varphi_v\rangle \;+\; \sum_c \beta_c\,|\psi_c\rangle\,,$$

and β_c is arbitrary. By using this feature, the pseudopotential $\hat{V}^{PP}$ is generalized to

$$\hat{V}^{PP}_{F_c} \;=\; \hat{V} \;+\; \sum_c |\psi_c\rangle \langle F_c| \,. \tag{2.87}$$

where F_c are arbitrary functions [65]. Therefore the eigenvalues and eigenfunctions of the pseudo-Hamiltonian are given by:

$$\left(\hat{H} \;+\; \hat{V}^{PP}_{F_c}\right) |\varphi'_\upsilon\rangle \;=\; E_\upsilon \, |\varphi'_\upsilon\rangle \,, \tag{2.88}$$

and the β_c are determined by the set of linear equations

$$\sum_{c'} \Big\{ (E_c - E_\upsilon)\, \delta_{cc'} \;+\; \langle F_c|\psi_{c'}\rangle \Big\} \beta_{c'} \;=\; -\langle F_c|\psi_\upsilon\rangle \,. \tag{2.89}$$

It is important to note that one can make an arbitrary selection of pseudopotentials only if one wants to calculate eigenvalues and that the form of the pseudo wavefunction depends on the adopted pseudopotential.

Norm-conserving pseudopotentials

The norm-conserving pseudoptentials are obtained by forcing the pseudo wavefunctions to coincide with the true valence wavefunctions beyond a certain distance called cutoff radius and to have the same norm as the true wavefunction. To generate such pseudopotentials, DFT calculations are performed for an isolated atom for a given reference electron configuration. In this discussion, we outline a pseudopotential generation recipe proposed by Troullier and Martins [66].

The norm-conserving pseudopotentials are constructed such that they satisfy the following four general conditions. First, the normalized atomic radial pseudopotential wavefunction with angular momentum l (R^{PP}_l) is equal to the normalized radial all-electron wavefunction with principal quantum number n and angular momentum l (R^{AE}_{nl}) beyond a chosen cutoff radius r_{cl},

$$R^{PP}_l(r) \;=\; R^{AE}_{nl}(r) \qquad \text{if } r \geqslant r_{cl}. \tag{2.90}$$

Second, the norm of the true and pseudo wavefunctions inside the pseudized region must

be the same (norm-conservation condition)

$$\int_0^{r_{cl}} dr|R_l^{PP}(r)|^2 r^2 \;=\; \int_0^{r_{cl}} dr|R_{nl}^{AE}(r)|^2 r^2. \tag{2.91}$$

Third, the eigenvalues of the pseudo wavefunctions coincide with those of the all-electron wavefunctions for a chosen electronic configuration of the atom

$$\varepsilon_l^{PP} \;=\; \varepsilon_{nl}^{AE}. \tag{2.92}$$

Finally, the valence pseudo wavefunctions generated from the pseudopotential should be nodeless. Several schemes have been proposed to generate first-principles pseudopotentials that satisfy the above conditions. These flavors differ mostly in the functional form of the potentials and the smoothness conditions. Presently, some of the smoothest norm-conserving pseudopotentials are obtained by Troullier and Martines. To obtain the norm-conserving pseudopotential the procedure is outlined below [63, 66]

1. The single atom Kohn-Sham radial equations are solved self-consistently in a given reference configuration (i.e. for a given distribution of electrons in the atomic energy levels) and by assuming spherical approximation to Hartree and exchange correlation potential and relativistic effects are ignored.

$$\left\{ -\frac{1}{2}\frac{d^2}{dr^2} \;+\; \frac{l(l+1)}{2r^2} \;+\; \upsilon_{KS}^{AE}[n^{AE}](r) \right\} rR_{nl}^{AE}(r) \;=\; \varepsilon_{nl}^{AE} rR_{nl}^{AE}(r), \tag{2.93}$$

   where $n^{AE}(r)$ is the total electron densities for the occupied all-electron wavefunctions. The Kohn-Sham potential for the one-electron self-consistent solution, υ_{KS}^{AE} is given by

$$\upsilon_{KS}^{AE}[n^{AE}] \;=\; -\frac{Z}{r} \;+\; \upsilon_H[n^{AE}](r) \;+\; \upsilon_{xc}[n^{AE}](r), \tag{2.94}$$

   where $\upsilon_H[n^{AE}](r)$ is the Hartree potential and $\upsilon_{xc}[n^{AE}](r)$ is the exchange-correlation potential.

2. Construct the pseudo wavefunctions on the basis of the above results. We defined

the pseudo wavefunctions as

$$R_l^{PP}(r) \;=\; \begin{cases} R_{nl}^{AE}(r) & \text{if } r \geqslant r_{cl} \\ r^l exp[p(r)] & \text{if } r < r_{cl} \end{cases} \tag{2.95}$$

with

$$p(r) \;=\; c_0 \;+\; c_2 r^2 \;+\; c_4 r^4 \;+\; c_6 r^6 \;+\; c_8 r^8 \;+\; c_{10} r^{10} \;+\; c_{12} r^{12}. \tag{2.96}$$

The coefficients of $p(r)$ are adjusted by imposing norm conservation condition, the continuity of the pseudo wavefunctions and their first four derivatives at $r \;=\; r_{cl}$ which in effect imposes the continuity of the screen pseudopotential and its first two derivatives and that the screen pseudopotential has zero curvature at the origin. This condition implies that

$$c_2^2 \;+\; c_4(2l+5) \;=\; 0, \tag{2.97}$$

and is the origin of the enhanced smoothness.

3. The pseudopotential is screened (scr) by inverting the Kohn-sham equation as

$$\upsilon_{scr,l}^{PP}(r) \;=\; \varepsilon_l^{PP} \;-\; \frac{l\,(l+1)}{2r^2} \;+\; \frac{1}{2rR_l^{PP}(r)}\frac{d^2}{dr^2}[rR_l^{PP}(r)]. \tag{2.98}$$

The resulting pseudopotential, $\upsilon_{scr,l}^{PP}$, still contains the screening effects due to the valence electrons. These effects needs to be subtracted and they include Hartree υ_H^{PP} and exchange-correlation υ_{xc}^{PP} potentials calculated from the valence pseudo wavefunction from the screened potential yields an ionic pseudopotential $\upsilon_{ion,l}^{PP}$:

$$\upsilon_{ion,l}^{PP}(r) \;=\; \upsilon_{scr,l}^{PP}(r) \;-\; \upsilon_H^{PP}(r) \;-\; \upsilon_{xc}^{PP}(r). \tag{2.99}$$

This form contains a nonlocal operator which requires a huge operational time.

4. Form the ionic pseudopotential operator which is defined as

$$\hat{\upsilon}_{ion}^{PP}(r) \;=\; \sum_l \upsilon_{ion,l}^{PP}(r)\hat{P}_l, \tag{2.100}$$

where $\hat{P}_l$ projects out the lth angular-momentum component from the wavefunction. This summation, however, needs to be truncated at some value of l in practice. This suggests that local potential, $v^{PP}_{ion,local}(r)$ which is independent of l acting on electrons with higher angular momentum than l_{max} can be replaced as $v^{PP}_{ion,local}(r) = v^{PP}_{ion,l_{max}}(r)$. The ionic pseudopotential can be re-written in a mathematical form as follows

$$\begin{aligned}
\hat{v}^{PP}_{ion}(r) &= \sum_{l=0}^{\infty} v^{PP}_{ion,l}(r)\hat{P}_l \\
&= \sum_{l=0}^{l_{max}} v^{PP}_{ion,l}(r)\hat{P}_l + \sum_{l=l_{max}+1}^{\infty} v^{PP}_{ion,l}(r)\hat{P}_l \\
&\approx \sum_{l=0}^{l_{max}} v^{PP}_{ion,l}(r)\hat{P}_l + v^{PP}_{ion,local}(r)\sum_{l=l_{max}+1}^{\infty}\hat{P}_l \\
&= \sum_{l=0}^{l_{max}} v^{PP}_{ion,l}(r)\hat{P}_l + v^{PP}_{ion,local}(r)\Big\{1 - \sum_{l=0}^{l_{max}}\hat{P}_l\Big\} \\
&= v^{PP}_{ion,local}(r) + \sum_{l=0}^{l_{max}}\Big[v^{PP}_{ion,l}(r) - v^{PP}_{ion,local}(r)\Big]\hat{P}_l. \qquad (2.101)
\end{aligned}$$

We now define the nonlocal potential which can be written in a form that separates long and short range components. The long range component is local and corresponds to the Coulomb tail. Choosing an arbitrary angular-momentum l component (usually the most repulsive one) is written as

$$v^{PP}_{nonlocal,l}(r) = v^{PP}_{ion,l}(r) - v^{PP}_{ion,local}(r). \qquad (2.102)$$

Hence the practical form of the ionic pseudopotential operator is thus given as

$$\hat{v}^{PP}_{ion}(r) = v^{PP}_{ion,l}(r) + \sum_{l=0}^{l_{max}} |l\rangle\, v^{PP}_{nonlocal,l}(r)\, \langle l|\,. \qquad (2.103)$$

This is the procedure of constructing the pseudopotential proposed by Troullier-Martins.

The cutoff radii, r_{cl}, are not adjustable pseudopotential parameters. The choice of a given set of cutoff radii establishes only the region where the pseudo and true wavefunctions coincide. Therefore, the cutoff radii can be considered as a measure of the quality of the pseudopotential. Their smallest possible value is determined by the location of the

outermost nodal surface of the true wavefunction. For cutoff radii close to this minimum value, the pseudopotential is considered realistic, but also very strong. If very large cutoff radii are selected, the pseudopotentials will be smooth and almost angular momentum independent, but of very low quality. A smooth potential leads to a fast convergence of calculation. The choice of the ideal cutoff is then the result of a balance between cost of calculations and pseudopotential accuracy. Now that we have obtained the pseudopotential for an isolated ion, we substitute equation Eq. (2.103) into (2.52), the Kohn-Sham equation of valence electrons in a system consisting of many atoms is represented as follows

$$\left\{ -\frac{1}{2}\nabla^2 \; + \; \sum_I \left[\sum_{l=0}^{l_{max}} |l\rangle \, \upsilon^{PP}_{nonlocal,l}(\mathbf{r}-\mathbf{R}_I) \, \langle l| \; + \; \upsilon^{PP}_{ion,local}(\mathbf{r}-s\mathbf{R}_I) \right] \; + \; \upsilon_H(\mathbf{r}) \; + \; \upsilon_{xc}(\mathbf{r}) \right\} \psi_i(\mathbf{r}) = \varepsilon_i \psi_i(\mathbf{r}). \tag{2.104}$$

Here, $\upsilon_{ion}(\mathbf{r})$ in (2.52) is replaced as

$$\upsilon_{ion}(\mathbf{r}) \; = \; \sum_I \hat{\upsilon}^{PP}_{ion}(\mathbf{r}-\mathbf{R}_I). \tag{2.105}$$

Kleinman and Bylander [64] suggested that the nonlocal part (the second term which is semi-local) in Eq. (2.103) can be written as a separable potential, thus transforming semi-local potential into a truly nonlocal pseudopotential, if $\varphi_{lm} \; = \; R^{PP}_l(r) Y_{lm}(r)$ are the solutions to the atomic pseudopotential for the valence states of interest, then the Kleinman and Bylander separable form is given by

$$\hat{\upsilon}^{KB}_{nonlocal,l}(r) \; = \; \sum_{l=0}^{l_{max}} \sum_{l=-m}^{l} \frac{|\varphi_{lm}(r)\upsilon^{PP}_{nonlocal,l}(r)\rangle \, \langle \varphi_{lm}(r)\upsilon^{PP}_{nonlocal,l}(r)|}{\langle \varphi_{lm}(r)| \, \upsilon^{PP}_{nonlocal,l}(r) \, |\varphi_{lm}(r)\rangle}. \tag{2.106}$$

The advantages of the separable form is that its operations need only the products of projection operators and that it is suited for time-saving calculations. However, there is a report of possibility of unphysical states appearing at energies below the true ground states eigenvalues of a specific angular momentum [67] resulting in what is called *ghost states* and can be graphically observed as divergences in the energy plot of the logarithmic derivative at unphysical low energies.

We replace the first term in the bracket of Eq. (2.104) by Eq. (2.106) and obtain the

complete expression of Kohn-Sham equations within Kleinman-Bylander approximation,

$$\left\{ -\frac{1}{2}\nabla^2 \; + \; \sum_I \left[\hat{v}^{KB}_{nonlocal,I}(\mathbf{r}-\mathbf{R}_I) \; + \; v^{PP}_{ion,local}(\mathbf{r}-\mathbf{R}_I) \right] \; + \; v_H(\mathbf{r}) \; + \; v_{xc}(\mathbf{r}) \right\} \psi_i(\mathbf{r}) \\ = \; \varepsilon_i \psi_i(\mathbf{r}). \tag{2.107}$$

Pseudopotential Transferability

The generated pseudopotential must at least reproduce the following features of a free atom in the reference configuration

1. The pseudo eigenvalues obtained by using pseudopotential are equal to the all-electron ones, and the corresponding orbitals agree exactly out side the cutoff radii.

2. The scattering properties are correct at each ε_i, in the sense that the logarithmic derivative and its energy derivative match the all-electron one at the same energy.

A useful pseudopotential needs to be transferable, i.e., it needs to describe accurately the behavior of the valence electrons in several different chemical environment. The logarithmic derivatives provide a first test of the transferability of the screened pseudopotential: The logarithmic derivative of the pseudo wavefunction determines the scattering properties of the pseudopotential. As long as the norm-conserving pseudopotential is concerned, the following relation is fulfilled:

$$\int_0^{rcl} dr\{rR_l(r,\varepsilon)\}^2 \; = \; -\frac{1}{2}\left\{ [r_{cl}R_l(r_{cl},\varepsilon)]^2 \, \frac{\partial}{\partial\varepsilon}\frac{d}{dr} lnR_l(r,\varepsilon) \right\}_{r=r_{cl}}^{\varepsilon=\varepsilon_k} \tag{2.108}$$

where $R_l(r,\varepsilon)$ is the radial wavefunction corresponding to energy ε, ε_k is the eigenvalue used in the pseudopotential-preparation, and r_{cl} is the radius of the core sphere. This suggests that the energy derivative of the logarithmic derivative obtained by using the norm-conserving pseudopotential coincides with the all-electron one to the the first order with respect to $\delta\varepsilon$. Logarithmic derivative is not an absolute test of the transferability of a pseudopotential. The ideal method to assess the transferability of a potential consists of testing it in diverse chemical environments.

2.3.3 Kohn-Sham Equation on three dimensional grid

In a real-space grid implementation, the Kohn-Sham equations must be discretized explicitly, the quantum-mechanical operators are known only at a discrete set of grid points. The wavefunctions, electron charge density, and potentials are directly represented on a three dimensional real-space grid of M_L grid points with linear grid spacing H. The kinetic-energy operator is expanded by using the higher order finite difference method as shown in equation (2.78). Following that, we set up a one-particle Kohn-Sham equation in real space using equations (2.107) and (2.106) of Kleinman-Bylander approximation. We assume a uniform grid over the three dimensions, but this is not a necessary assumption of equation (2.107). Over these grid points, we must solve the Kohn-Sham equation in real-space mesh as:

$$
\begin{aligned}
&-\frac{1}{2}\Bigg\{\sum_{m_1=-M_d}^{M_d} C_{m_1}\psi(x_i + m_1H_x, y_j, z_k) + \sum_{m_1=-M_d}^{M_d} C_{m_2}\psi(x_i, y_j + m_2H_y, z_k) \\
&+ \sum_{m_1=-M_d}^{M_d} C_{m_3}\psi(x_i, y_j, m_3H_z + z_k)\Bigg\} \\
&+ \left[\sum_I \upsilon^I_{ion}(X_i, Y_j, Z_k) + \upsilon_H(x_i, y_j, z_k) + \upsilon_{xc}(x_i, y_j, z_k)\right]\psi(x_i, y_j, z_k) \\
&= \varepsilon\psi(x_i, y_j, z_k).
\end{aligned}
\tag{2.109}
$$

When the separable form of the pseudopotential given by Kleinman and Bylander is used as a nonlocal component, the inner product between the pseudopotential and wavefunction is given by

$$
\begin{aligned}
\upsilon^I_{ion}(X_i, Y_j, Z_k)\psi(x_i, y_j, z_k) &= \upsilon^{PP,I}_{ion,local}(X_i, Y_j, Z_k)\psi(x_i, y_i, z_k) \\
&+ \sum_{l=0}^{l_{max}} \sum_{l=-m}^{l} G^I_{lm}\upsilon^{PP,I}_{nonlocal,l}(X_i, Y_j, Z_k)\varphi^I_{lm}(X_i, Y_j, Z_k).
\end{aligned}
\tag{2.110}
$$

Here

$$
G^I_{lm} = \frac{\sum_{i,j,k}\varphi^{*I}_{lm}(X_i, Y_j, Z_k)\upsilon^{PP,I}_{nonlocal,l}(X_i, Y_j, Z_k)\psi(x_i, y_i, z_k)\,H_xH_yH_z}{\sum_{i,j,k}\varphi^{*I}_{lm}(X_i, Y_j, Z_k)\upsilon^{PP,I}_{nonlocal,l}(X_i, Y_j, Z_k)\varphi^I_{lm}(X_i, Y_j, Z_k)H_xH_yH_z},
\tag{2.111}
$$

is the projection coefficients. Now, $(X_i, Y_j, Z_k) = (x_i - R^I_x, y_j - R^I_y, z_k - R^I_z)$ and (R^I_x, R^I_y, R^I_z) is the location of the $I-th$ pseudopotential ion υ^I_{ion} interacting with an electron. The nonlo-

cality in υ^I_{ion} is reflected by the occurrence of $\psi(x_i, y_i, z_k)$ in G_{lm}. The Kleinman-Bylander form is advantageous in real space formulations because outside the pseudopotential core radius, $\mathrm{r_{cl}}$, $\upsilon^{PP,I}_{nonlocal,l}(X_i, Y_j, Z_k) = 0$. This limited nonlocality means that the discrete representation of υ^I_{ion} is sparse [68]. Additionally, it means in periodic systems only the local pseudopotential has infinit periodic replicas, and that those replicas behave in the usual $\sim \frac{1}{\mathrm{r}}$ manner of the true ionic potential.

If there are M_L grid points, the size of the full matrix resulting from the above eigenvalue problem is $M_L \times M_L$. Here υ^I_{ion} contains the nonlocal ionic pseudopotential, υ_H is the Hartree potential and υ_{xc} the exchange and correlation potential in real space representation. Two fixed grid parameters used in setting up the matrix are the grid spacing H and the order M_d.

2.3.4 Bloch theorem

Bloch's theorem states that the electronic wavefunctions can be expanded in terms of a discrete plane-wave basis set: According to the Bloch's theorem, in a periodic solid each electronic wavefunction can be written as the product of a cell-periodic part and a wavelike part.

$$\psi_{n\mathbf{k}}(\mathbf{r}) = exp\,[i\mathbf{k}\cdot\mathbf{r}]\cdot u_{n\mathbf{k}}(\mathbf{r}) \tag{2.112}$$

$$u_{n\mathbf{k}}(\mathbf{r}+\mathbf{R}) = u_{n\mathbf{k}}(\mathbf{r}), \tag{2.113}$$

where $n, \mathbf{k}, \mathbf{R}$ represents, band index of a particular wavefunction, wave vector and Bravais lattice vector respectively. The cell-periodic part of the wavefunction can be expanded using a basis set consisting of a discrete set of plane waves whose wave vectors are reciprocal lattice vectors of the crystal,

$$u_{n\mathbf{k}}(\mathbf{r}) = \sum_{\mathbf{G}} c_{n\mathbf{kG}}(\mathbf{r}) exp[i\mathbf{G}\cdot\mathbf{r}], \tag{2.114}$$

where the reciprocal lattice vectors $\mathbf{G}$ are defined by $\mathbf{G}\cdot\mathbf{l} = 2\pi m$ for all $\mathbf{l}$ where $\mathbf{l}$ is a lattice vector of the crystal and m is an integer, therefore each electronic wavefunction

can be written as sum of plane waves

$$\psi_{n\mathbf{k}}(\mathbf{r}) \;=\; \sum_{\mathbf{G}} c_{n\mathbf{k}+\mathbf{G}}(\mathbf{r}) exp[i(\mathbf{k}+\mathbf{G})\cdot\mathbf{r}]. \tag{2.115}$$

In principle, accurate physical quantities such as total energies and electronic charges are obtained by solving the Kohn-Sham equations at infinite **k** points. It is impossible to perform calculations at infinite **k** points within finite time frame. However, the electronic wavefunctions at **k** points which are very close to each other will be almost identical. Hence it is possible to represent the electron wavefunctions in a region of **k** space by the wavefunction at a single **k** points in the region. In this case, the electron wavefunctions at only a finite number of **k** points are required to calculate physical quantities such as total energies, electron charges and so on of the solid. Methods for generating the sets of special **k** points in the Brillouin zone exist which provides efficient means of integrating periodic functions of the wave vector [69–71]. Efficient methods have been devised to obtain accurate physical quantities of an insulator and semiconductor by calculating the electron wavefunctions at a very small number of **k** points. On the other hand, the electronic potential and total energy are more difficult to calculate in metallic system because a dense set of **k** points are required to define the Fermi surface precisely. In principle, a converged electronic potential and total energy can always be obtained provided that the computational time is available to calculate the electronic wavefunctions at sufficiently dense sets of **k** points.

2.3.5 Grid spacing

When plane waves are used as a basis set for the electronic wavefunctions, the Kohn-Sham equations assume a particular simple form. Substituting equation (2.115) into (2.52) and integration carried out over **r** gives the secular equation

$$\sum_{\mathbf{G}'} \Big\{ \frac{1}{2}|\mathbf{k}+\mathbf{G}|^2\delta_{\mathbf{G}\mathbf{G}'} \;+\; \mathbf{V}_{ion}(\mathbf{G}-\mathbf{G}') \;+\; \mathbf{V}_H(\mathbf{G}-\mathbf{G}') \;+\; \mathbf{V}_{xc}(\mathbf{G}-\mathbf{G}') \Big\} c_{n\mathbf{k}+\mathbf{G}'} \;=\; \varepsilon_n c_{n\mathbf{k}+\mathbf{G}}. \tag{2.116}$$

The kinetic energy is diagonal in this form and various potentials have been described in their Fourier transforms. The solution of equation (2.116) is done by diagonalizing

the hamiltonian matrix given by the terms in the brackets. The size of the matrix is determined by the kinetic energies $\frac{1}{2}|\mathbf{k}+\mathbf{G}|^2$. However, the choice of the minimum kinetic energy needed to determine the matrix size sufficient for accurate calculation is called the cutoff energy given by

$$E_c = \frac{|\mathbf{G}_{cut}|^2}{2}. \tag{2.117}$$

In the real space grid method, this cutoff energy is determined by the grid spacing H given as

$$E_c = \frac{1}{2}\left[\frac{\pi}{H_i}\right]^2, \tag{2.118}$$

where $H_i (i = 1, 2, 3)$ for each spatial direction.

2.4 Flow Chart of Total-Energy Electronic-Structure Calculations

Total-energy electronic-structure calculations in the norm conserving pseudopotential scheme can be performed in real-space scheme discussed below for massively parallel calculations [59]. DFT calculations in real-space can be classified in two categories (1) system with periodic boundary conditions, this is typical of crystalline solids or supercell geometries: (2) systems with decaying boundary conditions, usual for molecules or clusters. Calculations in this present thesis is based on the former. First we set up the initial coordinates and the species of each atom in the unit cell. Second we construct the Kohn-Sham equation Eq. (2.109). Third we perform the self-consistency calculation to solve the Kohn-Sham equation. Fourth we calculate the Hellmann-Feynman forces. Figure 2.1 outlines the basic steps of such calculations. In the geometry optimization procedure, the ionic configuration $\mathbf{R}_I$ are updated according to their Hellmann-Feynman forces until the residual forces on all the ions are smaller than a given value. In the Hellmann-Feynman force calculations, the Kohn-Sham equations under given configuration are solved iteratively until self-consistency is achieved. This means, there are two main loops in the total-energy electronic structure calculations. In the following, we briefly explain each step of the calculations. Note that, $f(\mathbf{r})$ is a general function defined by its Fourier trans-

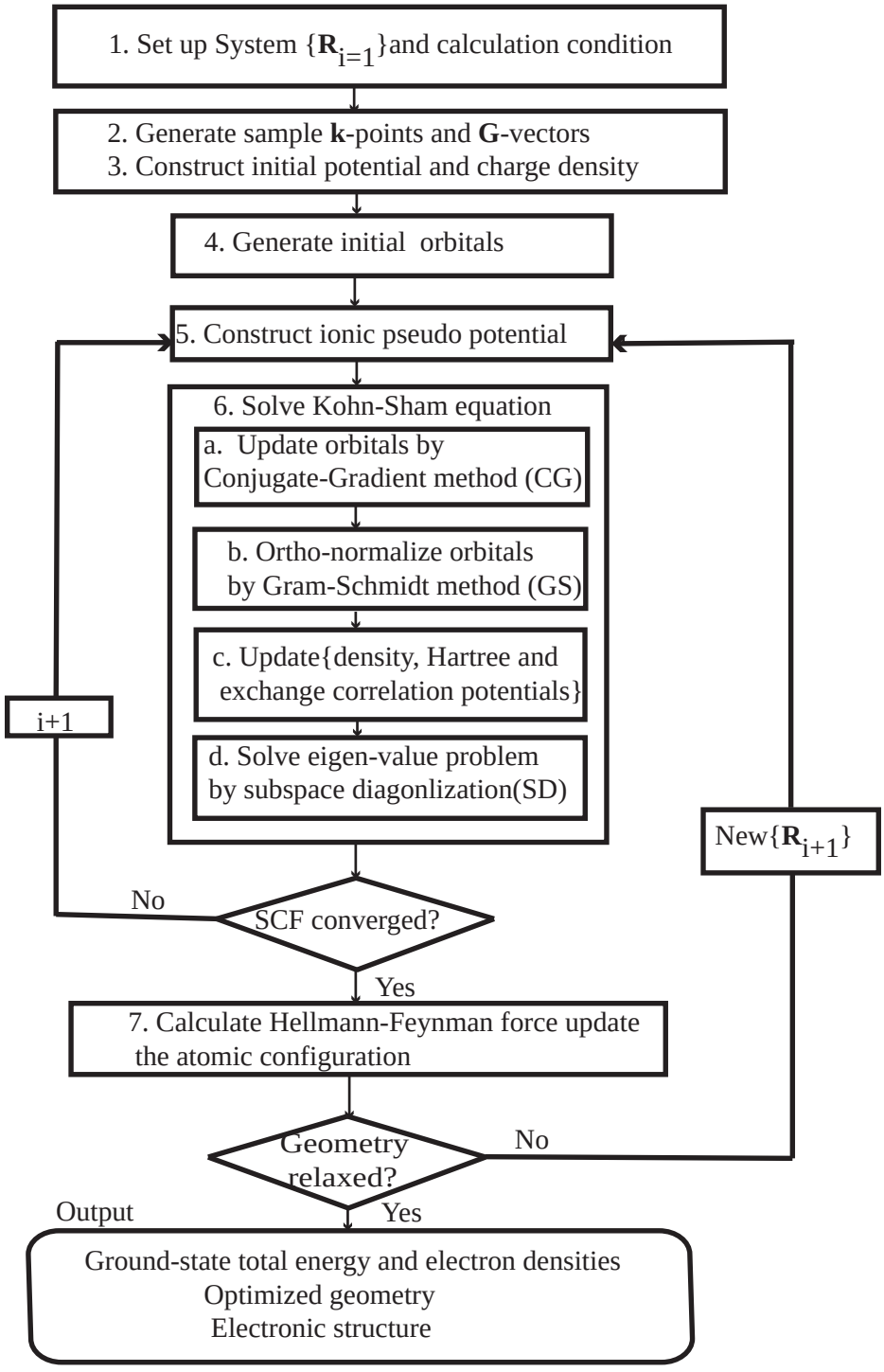

Figure 2.1: Flow chart of total-energy electronic-structure calculations by using norm-conserving pseudopotential in the real-space grid.

form as:

$$f(\mathbf{r}) = \sum_{\mathbf{G}} f(\mathbf{G}) e^{i\mathbf{G}\cdot\mathbf{r}} \tag{2.119}$$

$$f(\mathbf{G}) = \frac{1}{\Omega} \int_{\Omega} d\mathbf{r} f(\mathbf{r}) e^{-i\mathbf{G}\cdot\mathbf{r}}, \tag{2.120}$$

where Ω is the crystal volume.

1. Set up a system and calculation conditions such as: Unit cell, symmetry, initial ionic configuration $\mathbf{R}_I$, grid spacing, convergence conditions, pseudopotentials, etc. The pseudo potentials are prepared and stored to external files before the DFT calculation begins.

2. Generate sample $\mathbf{k}$-points and the reciprocal lattice vectors $\mathbf{G}$, according to the calculation conditions.

3. Pseudopotentials data from external files are read and then prepared on each grid point by interpolation. In actual fact, raw data are not used for the interpolation but rather preconditioned by Fourier-filtering or double grid method to avoid the so-called egg-box effect which is a spurious energy dependence on atomic position relative to neighboring grid points. We obtain the local potential $V_{ion,local}(\mathbf{r})$ by placing an ionic local pseudopotential at the position of every ion in a periodic system. First construct the local potential $V_{ion,local}(\mathbf{G})$ from $V^{\mathbf{R}_I}_{ion,local}(\mathbf{G})$, which is the Fourier components of the ionic local pseudopotential for the ion located at $\mathbf{R}_I$ in the unit cell. $V^{\mathbf{R}_I}_{ion,local}(\mathbf{G})$ are parts of those of the total ionic local pseudopotential

$V_{ion,local}(\mathbf{G})$ The pseudopotential is considered in its more general non-local form

$$
\begin{aligned}
V_{ion,local}(\mathbf{r}) &= \sum_{I,\mathbf{l}} V_{ion,local}\left(\mathbf{r}-\mathbf{R_I}-\mathbf{l}\right) \\
&= \sum_{I,\mathbf{l}} \left\{ \frac{1}{\Omega} \sum_{G} V^{R_I}_{ion,local}(\mathbf{G}) e^{i\mathbf{G}\cdot(\mathbf{r}-\mathbf{R_I}-\mathbf{l})} \right\} \\
&= \sum_{\mathbf{G}} e^{i\mathbf{G}\cdot\mathbf{r}} \left\{ \frac{1}{\Omega} \sum_{I,\mathbf{l}} V^{\mathbf{R_I}}_{ion,local}(\mathbf{G}) e^{-i\mathbf{G}\cdot\mathbf{R_I}} e^{-i\mathbf{G}\cdot\mathbf{l}} \right\} \\
&= \sum_{\mathbf{G}} e^{i\mathbf{G}\cdot\mathbf{r}} \left\{ \frac{1}{\Omega_0} \sum_{I} V^{\mathbf{R_I}}_{ion,local}(\mathbf{G}) e^{-i\mathbf{G}\cdot\mathbf{R_I}} \right\} \\
&\equiv \sum_{\mathbf{G}} e^{i\mathbf{G}\cdot\mathbf{r}} V_{ion,local}(\mathbf{G}), \qquad (2.121)
\end{aligned}
$$

$$
\begin{aligned}
V^{\mathbf{R_I}}_{ion,local}(\mathbf{G}=\mathbf{0}) &= \int d\mathbf{r} V^{\mathbf{R}_I}_{ion,local}(r) e^{-i\mathbf{0}\cdot\mathbf{r}} \\
&= 4\pi \int dr r^2 V^{\mathbf{R}_I}_{ion,local}(r) \qquad (2.122)
\end{aligned}
$$

$$
\begin{aligned}
V^{\mathbf{R_I}}_{ion,local}(\mathbf{G}\neq\mathbf{0}) &= \int d\mathbf{r} V^{\mathbf{R}_I}_{ion,local}(r) e^{-i\mathbf{G}\cdot\mathbf{r}} \\
&= 4\pi \int dr r^2 V^{\mathbf{R}_I}_{ion,local}(r) \frac{\sin(Gr)}{Gr}, \qquad (2.123)
\end{aligned}
$$

where Ω_0 is the volume of the unit cell and $V^{\mathbf{R_I}}_{ion,local}(r)$ corresponds to ionic species are calculated during the pseudopotential generation. It is important to recognize that the pseudopotential is a pure Coulomb potential of the form Z_υ/r, where Z_υ is the number of valence electrons, at large distance and thus the pseudopotential diverges as $1/G^2$ at small wave vectors. Yet there are similar divergences in the Coulomb energies due to the ion-ion interactions and the electron-electron interactions. These three divergence terms of the total energy exactly cancel out due to charge neutrality.

4. Initial orbitals are prepared using a random-number generator and ortho-normalized by Gram-Shmidt procedure.

5. We generate an initial electron density n_{in} as a superposition of the isolated pseudo atom densities which are accompanied with the pseudopotentials and calculate initial local potential $V_{local} = V_{ion,local} + V_H + V_{xc}$. Construct the initial charge density $n(\mathbf{G})$ from $n^{\mathbf{R_I}}(\mathbf{G})$, which is the Fourier components of the atomic charge density for the local atom at $\mathbf{R}_I$ in the unit cell. $n_{in}(\mathbf{r})$ is obtained by placing a charge density

at the position of every atom in a periodic system

$$
\begin{aligned}
n_{in}(\mathbf{r}) &= \sum_{I,l} n(\mathbf{r}-\mathbf{R_I}-\mathbf{l}) \\
&= \sum_{I,l}\left\{\frac{1}{\Omega}\sum_{\mathbf{G}} n^{\mathbf{R}_I}(\mathbf{G})e^{i\mathbf{G}\cdot(\mathbf{r}-\mathbf{R_I}-\mathbf{l})}\right\} \\
&= \sum_{\mathbf{G}} e^{i\mathbf{G}\cdot\mathbf{r}}\left\{\frac{1}{\Omega}\sum_{I,\mathbf{l}} n^{\mathbf{R_I}}(\mathbf{G})e^{-i\mathbf{G}\cdot\mathbf{R_I}}e^{-i\mathbf{G}\cdot\mathbf{l}}\right\} \\
&= \sum_{\mathbf{G}} e^{i\mathbf{G}\cdot\mathbf{r}}\left\{\frac{1}{\Omega_0}\sum_{I} n^{\mathbf{R_I}}(\mathbf{G})e^{-i\mathbf{G}\cdot\mathbf{R_I}}\right\} \\
&\equiv \sum_{\mathbf{G}} e^{i\mathbf{G}\cdot\mathbf{r}} n(\mathbf{G}), \qquad (2.124)
\end{aligned}
$$

$$
\begin{aligned}
n^{\mathbf{R_I}}(\mathbf{G}=\mathbf{0}) &= \int d\mathbf{r} n^{\mathbf{R}_I}(r)e^{-i\mathbf{0}\cdot\mathbf{r}} \\
&= 4\pi\int dr r^2 n^{\mathbf{R}_I}(r) \qquad (2.125)
\end{aligned}
$$

$$
\begin{aligned}
n^{\mathbf{R_I}}(\mathbf{G}\neq\mathbf{0}) &= \int d\mathbf{r} n^{\mathbf{R}_I}(r)e^{-i\mathbf{G}\cdot\mathbf{r}} \\
&= 4\pi\int dr r^2 n^{\mathbf{R}_I}(r)\frac{\sin(Gr)}{Gr}, \qquad (2.126)
\end{aligned}
$$

$$
n^{\mathbf{R_I}}(r) = \sum_{l} N_{occ}(l)|R_l^P|^2, \qquad (2.127)
$$

where $N_{occ}(l)$ is the number of occupied electron at l orbital. When we calculate the initial charge density from the atom pseudo wavefunction, the initial Hartree potential V_H, and exchange-correlation potential V_{xc}, are obtained from the initial electron density:

$$
V_{local}(\mathbf{G}) = V_{ion,local}(\mathbf{G}) + V_H(\mathbf{G}) + V_{xc}(\mathbf{G}), \qquad (2.128)
$$

where

$$
V_{ion,local}(\mathbf{G}) = \frac{1}{\Omega_0}\sum_{I} V^{\mathbf{R}_I}_{ion,local}(\mathbf{G})e^{-i\mathbf{G}\cdot\mathbf{R_I}}, \qquad (2.129)
$$

$$
V_H(\mathbf{G}) = \frac{4\pi}{|\mathbf{G}|^2}n(\mathbf{G}), \qquad (2.130)
$$

$$
V_{xc}(\mathbf{G}) = \frac{1}{\Omega_0}\int d\mathbf{r}\upsilon_{xc}(\mathbf{r})e^{-i\mathbf{G}\cdot\mathbf{r}}. \qquad (2.131)
$$

$$
(2.132)
$$

Therefore, the initial local potential $V_{local}(\mathbf{r})$ is obtained by Fourier transforming $V_{local}(\mathbf{G})$ as:

$$V_{local}(\mathbf{r}) \;=\; \sum_{\mathbf{G}} V_{local}(\mathbf{G}) e^{i\mathbf{G}\cdot\mathbf{r}}. \tag{2.133}$$

6. Construct the Kohn-Sham equations by using the initial electron densities $n_{in}^{(i)}(\mathbf{r})$ and the ionic configuration $\{\mathbf{R_I^{(i)}}\}$, and solve the equations to obtain new Kohn-Sham wavefunction $|\psi_{n\mathbf{k}}^{(i+1)}\rangle$ and their eigenvalues $\varepsilon_{n\mathbf{k}}^{(i+1)}$. The procedure to obtain the Kohn-Sham wavefunction and eigenvalues under fixed potential are outlined in steps (a)~(d) below

   (a) We find the subspace spanned by the eigenfunctions associated with the smallest M_B eigenvalues of the Hamiltonian H_{KS} in M_L dimension and minimize the Rayleigh quotients (RQ) to update the orbitals as:

$$\varepsilon_{n\mathbf{k}} \;=\; \frac{\langle\psi_{n\mathbf{k}}|\, H_{KS}\, |\psi_{n\mathbf{k}}\rangle}{\langle\psi_{n\mathbf{k}}|\psi_{n\mathbf{k}}\rangle}. \tag{2.134}$$

   The minimization is performed using conjugate gradient (CG) method, but other schemes can be used. The intention is, we numerically solve $M_L \times M_L$ hermitian matrix eigenvalue problem for the lowest M_B eigen-pairs since $M_L \gg M_B$.

   (b) Following the minimization, we update the wavefunction by performing Gram-Schmidt (GS) procedure to recover the ortho-normalization relations among the orbitals as follows:

$$|\phi_{n\mathbf{k}}\rangle \;=\; |\psi_{n\mathbf{k}}\rangle \;-\; \sum_{m=1}^{n-1} \psi_{m\mathbf{k}}\langle\psi_{m\mathbf{k}}|\psi_{n\mathbf{k}}\rangle, \tag{2.135}$$

$$\langle\phi_{m\mathbf{k}}|\phi_{n\mathbf{k}}\rangle \;=\; \delta_{mn}. \tag{2.136}$$

   (c) We calculate the Fermi energy, update the new electron densities $n^{(i+1)}$ by using $\varepsilon_{n\mathbf{k}}^{(i+1)}$ and $\psi_{n\mathbf{k}}^{(i+1)}$. The electron densities are calculated by using the Fermi energy, compute new local potential $V_{local}^{(i+1)}$ by using the new electron densities $n^{(i+1)}$ as follows:

$$V_{local}^{(i+1)}(\mathbf{r}) \;=\; V_{local}^{ion}(\mathbf{r}) \;+\; V_H\left[n^{(i+1)}(\mathbf{r})\right] \;+\; V_{xc}\left[n^{(i+1)}(\mathbf{r})\right]. \tag{2.137}$$

Compare the present local potential $V^{(i)}_{local}(\mathbf{r})$ with the new one $V^{(i+1)}_{local}(\mathbf{r})$, the self-consistency loop is stopped when some convergence criterion is reached (then follow on to step 7). For instance, one can use the averaged-squared error between the two local potentials, $\langle\{V^{(i)}_{local} - V^{(i+1)}_{local}\}^2\rangle_{\mathbf{r}} < \epsilon$ where ϵ is a given value typically $\sim 10^{-16}[Ht^2]$. If the criterion is not satisfied, one restarts the self-consistency cycle with the new local potential $V^{(i+1)}_{local}$ starting from step 6(a).

(d) We perform subspace diagonalization (SD) to reduce the M_L-dimension of $H_{ML\times ML} = H_{KS}$ hamiltonian to M_B-dimension of $H_{M_B} = H_{M_B\times M_B}$ hamiltoinian eigenvalue problem. The subspace is refined through subspace diagonalization. Approximate eigenvectors are obtained as resultant Ritz vectors, and are used as the initial vectors for the next iteration. The procedure *a, b* and *c* are performed until the subspace converges sufficiently to be that spanned by the eigenvectors. This operation results in an improved wavefunctions by linear combination of the updated wavefunctions as:

$$|\psi_{n\mathbf{k}}\rangle \;=\; \sum_{m=1}^{M_B} c^n_m\,|\phi_{m\mathbf{k}}\rangle\,. \tag{2.138}$$

The optimal coefficients for the linear combinations can be obtained as follows:

$$H_{KS}\,|\psi_{n\mathbf{k}}\rangle \;=\; \varepsilon_n\,|\psi_{n\mathbf{k}}\rangle\,, \tag{2.139}$$

substitute Eq. (2.139) into (2.138) we obtain

$$\sum_{m=1}^{M_B} c^n_m H_{KS}\,|\phi_{m\mathbf{k}}\rangle \;=\; \varepsilon_n \sum_{m=1}^{M_B} c^n_m\,|\phi_{m\mathbf{k}}\rangle\,. \tag{2.140}$$

We then multiply $\langle\phi_{l\mathbf{k}}|$ from the left hand side and re-write the equation as:

$$\sum_{m=1}^{M_B} c^n_m\,\langle\phi_{l\mathbf{k}}|\,H_{KS}\,|\phi_{m\mathbf{k}}\rangle \;=\; \varepsilon_n \sum_{m=1}^{M_B} c^n_m\,\langle\phi_{l\mathbf{k}}|\phi_{m\mathbf{k}}\rangle \tag{2.141}$$

$$\begin{aligned}\sum_{m=1}^{M_B} c^n_m\{H_{M_B\times M_B}\}_{lm} \;&=\; \varepsilon_n \sum_{m=1}^{M_B} c^n_m\delta_{lm}\\ &=\; \varepsilon_n c^n_l,\end{aligned} \tag{2.142}$$

where

$$\{H_{M_B\times M_B}\}_{lm} \;=\; \langle\phi_{l\mathbf{k}}|\, H_{KS}\,|\phi_{m\mathbf{k}}\rangle \;=\; \langle\phi_{l\mathbf{k}}|\, H_{ML\times ML}\,|\phi_{m\mathbf{k}}\rangle\,. \tag{2.143}$$

This matrix equation is expanded as

$$\begin{pmatrix} H_{1,1} & H_{1,2} & \cdots & H_{1,n} \\ H_{2,1} & H_{2,2} & \cdots & H_{2,n} \\ \vdots & \vdots & \ddots & \vdots \\ H_{M_B,1} & H_{M_B,2} & \cdots & H_{M_B,M_B} \end{pmatrix} \begin{pmatrix} c_n^1 \\ c_n^2 \\ \vdots \\ c_n^{M_B} \end{pmatrix} \;=\; \varepsilon_n \begin{pmatrix} c_n^1 \\ c_n^2 \\ \vdots \\ c_n^{M_B} \end{pmatrix} \tag{2.144}$$

The matrix equation (2.144) is an eigenvalue problem from which the optimal coefficients and eigenvalues can be obtained by solving its corresponding circular equation. The coefficients are used to compute the Ritz vectors in equation (2.138). The adopted M_B Ritz vectors are used as the approximate initial eigenvectors for the next subspace diagonalization. The procedure $a \sim d$ is repeated until self-consistency field (SCF) is achieved among the orbitals, density and potential.

7. Calculate the Hellmann-Feynman forces using the converged self-consistent electronic structures. The geometry-optimization loop is stopped when the residual forces on all the ions are smaller than a given value, typically $\sim 10^{-3}$[Ht/a.u.]. If the criterion is not fulfilled, one moves the ions according to their Hellmann-Feynman forces and restart the geometry-optimization loop with new ionic configuration $\{\mathbf{R_I^{(i+1)}}\}$ (go to step 5).

2.5 Models and Calculation Conditions

In this thesis, nuclei and core electrons are simulated by norm-conserving pseudopotentials generated by Troullier-Martins scheme [66]. The ground-state atomic configuration of C and Si are $(1s)^2(2s)^2(2p)^2$ and $(1s)^2(2s)^2(2p)^6(3s)^2(3p)^2$ respectively. We regard $2s$ and $2p$ of C as well as $3s$ and $3p$ of Si as valence orbitals. Nonlocality for both s and p potentials are considered. We examined the transferability of the pseudopotentials by changing their hardness and computing the structural parameters of 3C-SiC, C and Si

Table 2.1: Condition for constructing C, Si and H pseudopotentials using Troullier-Martins scheme.

species	Carbon	Silicon	Hydrogen
configuration	$1s^2 2s^2 2p^2$	$1s^2 2s^2 2p^6 3s^2 3p^2$	$1s^1$
core	$1s$	$1s, 2s, 2p$	–
valence	$2s, 2p$	$3s, 3p$	$1s$
local	$3d$	$3d$	$1s$
r_{cl} [$a.u.$]	1.50($2s$)	2.25($3s$)	1.68($1s$)
	1.54($2p$)	2.25($3p$)	
	1.54(local)	2.25(local)	1.68(local)

crystals and similarly have compared the vibrational properties of SiH_4 and CH_4 in the breathing mode. We find that the core radius r_{cl} of 1.50 a.u and 1.54 a.u for $2s$ and $2p$ of C and 2.25 a.u for both $3s$ and $3p$ of Si as shown in Table 2.5 accordingly. Similarly, we have also prepared hydrogen pseudopotential for the slab model, where r_{cl} = 1.68 a.u is taken for 1s orbital of H. We used the reference configuration of C and Si as empty d-orbital for the generation of the local pseudopotential. The nonlocal angular-momentum-dependent wavefunctions and pseudopotentials of carbon and silicon atoms are shown in Figure 2.2 and Figure 2.3 respectively.

We use the local density approximation (LDA) functional to express the exchange-correlation energy. The functional as parametrized by Perdew and Zunger [56] is used. The conjugate gradient scheme [72] is used for solving Kohn-Sham equations in order to obtain wavefunctions and also when optimizing atomic geometries according to Hellmann-Feynman forces. Forces on acting atoms in fully relaxed positions are less than 1.0×10^{-3} eV/Å.

For the calculation of 3C-SiC(111) on Si(110) surface, the mesh size of the grid used is determined by calculating total energies of bulk carbon changing the mesh size in the range 0.25~0.18Å equivalent to 44~85 Ry. We find that 0.21Å (~62Ry) grid spacing is enough cutoff energy sufficient to assure the convergence in reproducing physical properties of the materials. Calculated bond lengths of CH_4 and SiH_4 and the lattice constants of C, Si and 3C-SiC crystals using these calculational parameters r_{cl} and E_c agree with the experimental values within acceptable errors as indicated in Table 2.2 and 2.3. These results are consistent with the trend that, LDA underestimate lattice constant and overestimate bulk modulus [73, 74]. Calculated vibrational frequencies and bulk modulus of

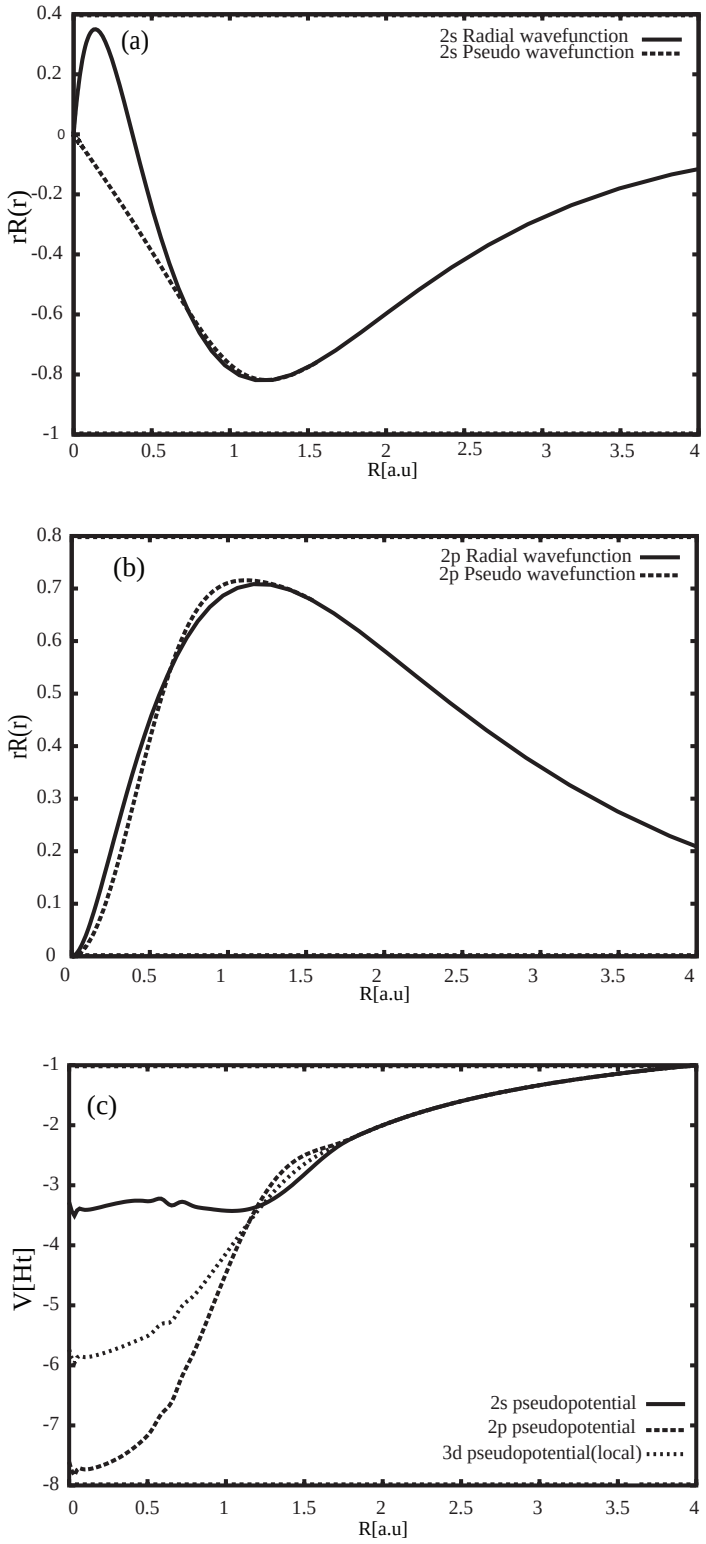

Figure 2.2: Real and pseudo radial wavefunctions are shown for the 2*s* (a) and the 2*p* (b) states of C. The norm conserving pseudopotential of 2*s*, 2*p* and 3*d* states with 3*d* state being local potential of C are shown in (c).

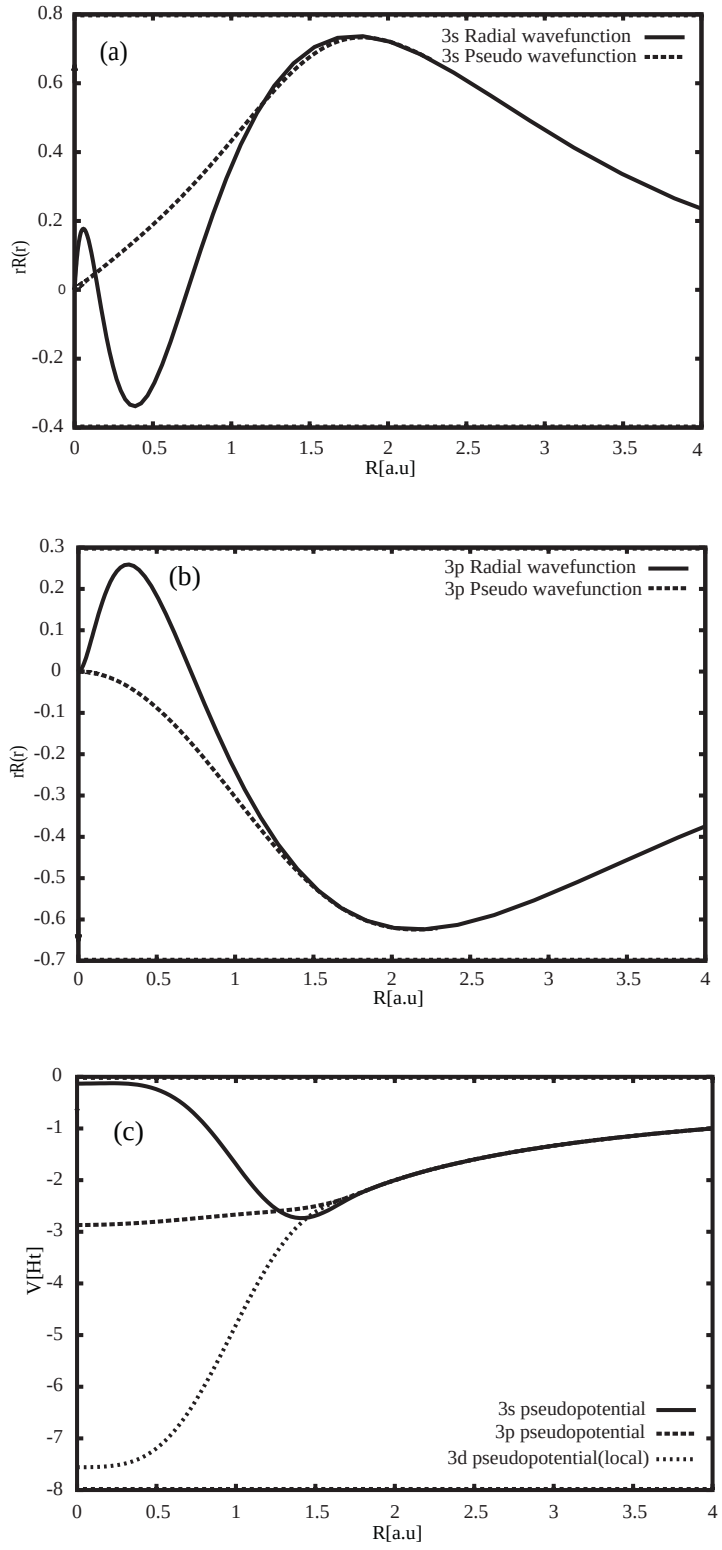

Figure 2.3: Real and pseudo radial wavefunctions are shown for the 3*s* (a) and the 3*p* (b) states of Si. The norm conserving pseudopotential of 3*s*, 3*p* and 3*d* states with 3*d* state being local potential of Si are shown in (c).

Table 2.2: Comparison between calculated and experimental values of lattice constant and bulk modulus.

species	C	
	lattice constant (Å)	bulk modulus (Mbar)
calculation	3.502	5.064
experiment	3.567	4.440
error in %	-1.6	+14

species	Si	
	lattice constant (Å)	bulk modulus (Mbar)
calculation	5.372	1.042
experiment	5.429	0.990
error in %	-1.06	+5

species	SiC	
	lattice constant (Å)	bulk modulus (Mbar)
calculation	4.289	2.461
experiment	2.461	2.240
error in %	-1.62	+9.8

these materials are in good agreement with experimental values within several percent. We calculate 3C-SiC(111)/Si(110) interface energies and the surface energies of clean Si(110) surface, Si- and C-terminated clean surfaces using these pseudopotential and the mesh size used is 0.21Å (~62Ry) throughout this thesis. The reason for this is, we find that surface and interface energies are strongly sensitive to the mesh spacing hence the decision to treat all calculations on equal footing. The surface energies of Si(110), Si- and C-terminated surfaces are found to converge within 0.05, 0.01 and 0.001 eV/atom respectively when the surfaces primitive cells are used.

We converge the 3C-SiC(111)/Si(110) interface slab thickness by displacement of atomic positions from the ideal configuration instead of interface energy. The initial attempts to converge the interface energy proved difficult, because we realized that Si- and C-terminated surfaces are polar and Si(110) surface nonpolar, trying to converge the interface energy of these polar and nonpolar materials is a hard task so we avoided it after several efforts. As a result we used mean atom displacement per layer and find that 8L/8L atomic layers converge to value less than 0.1Å of the layers far from the interface. We

Table 2.3: Comparison between calculated and experimental values of bond length and phonon frequency of CH_4 and SiH_4.

species	CH_4	
	bond length (Å)	Phonon frequency (cm^{-1})
calculation	1.093	2947.00
experiment	1.089~1.095	2917.00~3137
error in %	+0.3	+1.03

species	SiH_4	
	bond length(Å)	Phonon frequency (cm^{-1})
calculation	1.478	2127.70
experiment	1.480	2186.84
error in %	-0.14	-2.7

believe this is sufficient to discuss convergence of the slab thickness as LDA is unlikely to give accuracy better than 0.1Å.

The surface properties of Si(110), 3C-SiC(111) and 3C-SiC($\bar{1}\bar{1}\bar{1}$) were simulated using repeated slab model. The calculation model is shown in Figure 2.4 schematically. The slabs are cut out from bulk Si and 3C-SiC crystals and put in a supercell with sufficient vacuum thickness. Si crystal has equivalent symmetry and thus we can make two equivalent surfaces at both ends of the slab. This property allows us to calculate the surface energy without resorting to passivating the dangling bonds.

We systematically increase the atomic layers in the supercell until the surface energy is converged. Figure 2.4(a) shows Si(110) surface supercell model calculation. We investigate surface and not thin film, therefore the possible interaction between the upper and lower surfaces is avoided. As a result, the thickness of the slab has to be thick enough that interaction between the two surfaces is negligible for which surface energy can converge. We achieve that by gradually increasing the atomic layers and keeping the vacuum thickness within the supercell constant. The model has the periodicity in the direction perpendicular to the surface. The vacuum layer must be thick enough so that the interaction between the periodically repeated adjacent surfaces in the direction perpendicular to the surface is negligible. We use 12 Å for all surface calculations after careful check.

When calculating the Si- and C-terminated surface energies of 3C-SiC, the supercell similar to Si(110) surface as previously described in Figure 2.4(a) is prepared and same

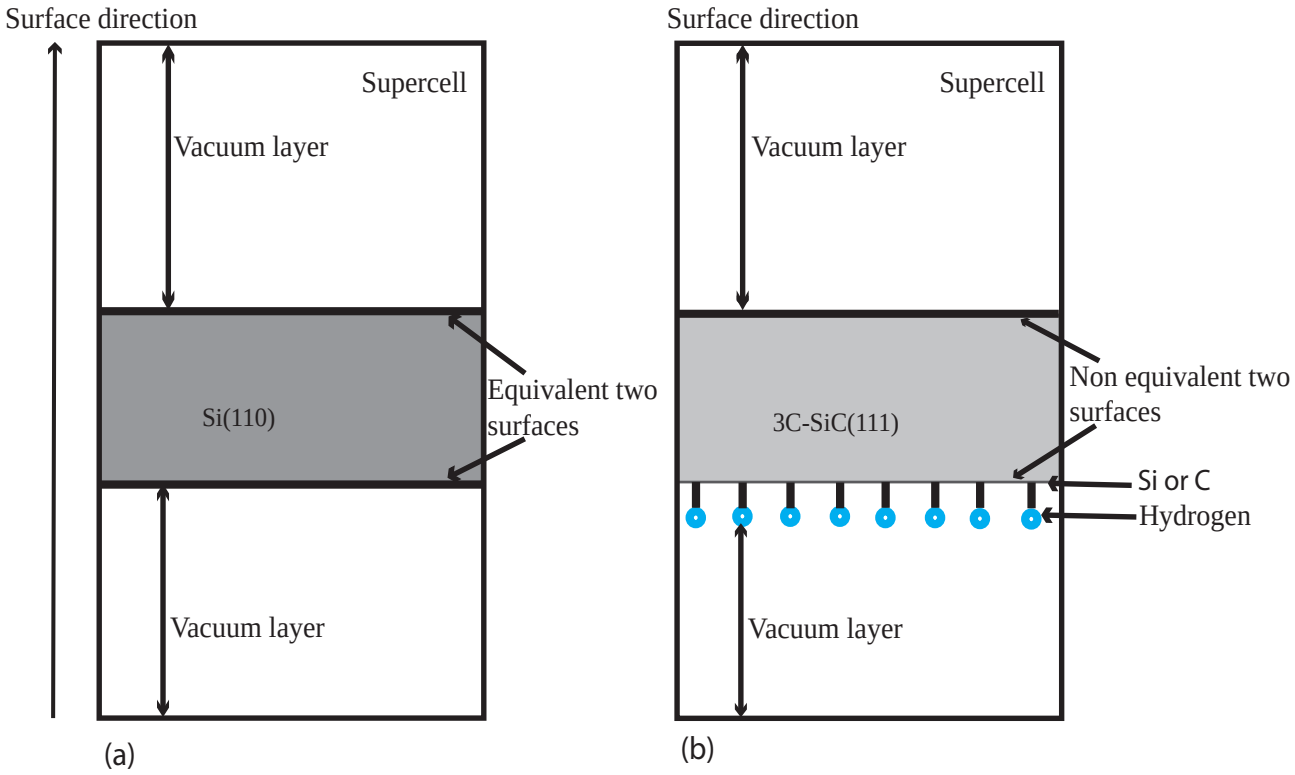

Figure 2.4: Schematic drawings of slab model cut out completely from bulk Si and 3C-SiC crystals respectively (a) two equivalent clean Si(110) surfaces (b) two inequivalent surfaces, one clean surface and other hydrogen passivated of 3C-SiC(111) surface. Small thick blue circles indicate hydrogen passivating the dangling bonds.

calculation conditions apply. However the crystal symmetry of Si- and C-terminated surfaces are different from Si(110) surface as shown in Figure 2.4(b). Because these two surfaces are inequivalent, several problems can occur during the self consistency cycle. At first, there might occur an artificial charge transfer to give rise to long-range electrostatic potentials, since the surface states of the cation (Si-terminated) dangling bonds lie above those of the anion (C-terminated) dangling bonds when the two surfaces are clean for a given slab. As a result, these surface states on both sides could interact with each other through the slab. Several possibilities exist to avoid these artificial effects. One way is to construct a slab containing a mirror plane. However, this slab would contain twice as many atoms, since the mirror plane had to lie in the 'bulk' of the slab. The approach we have taken is to saturate the dangling bonds of one surface with hydrogen atoms and the other allow to be clean surface as adopted by these workers [75, 76]. Detail discussion is given in section 3.1. For relaxed atomic geometry calculation, the atomic positions of the bottom-most atoms as well as the H atoms attached are fixed to their ideal positions. Technically, the surface energy calculated by this approach is not very correct since the hydrogen terminated surface energy part has not been removed from it and needs to be corrected. However we observed that, the surface energy calculated by this approach compares favorably well with the experimental value which suggests that calculation error due to the non-removal of the hydrogen terminated surface is insignificant or minimal.

Next we consider the 3C-SiC(111) on Si(110) surface system. The interface model is constructed by cutting out the required surfaces from the individual bulk crystals of 3C-SiC and Si and put together in a supercell simulated by repeated slab model as shown in Figure 2.5(a). The two outer-most surfaces are passivated with hydrogen which are fixed including the atomic layer the hydrogen is attached to and the rest of the atoms are allowed to relax completely. The supercell consists of two possible candidate interfaces. (i) silicon-carbon (Si-C) that is 3C-SiC($\bar{1}\bar{1}\bar{1}$)/Si(110) and (ii) silicon-silicon (Si-Si) that is 3C-SiC(111)/Si(110) interfaces as shown in Figure 2.5[(b), (c)] respectively.

When interface structures are discussed, one takes slab model and terminate it with hydrogen. The hydrogen and the atomic layer it is attached to are fixed and the remaining layers are relaxed. The atomic layers are then subsequently increased until the desired convergence is achieved. In this case, we encounter several problems. The obvious examples are, in the lateral direction there are many atoms which means large degrees of

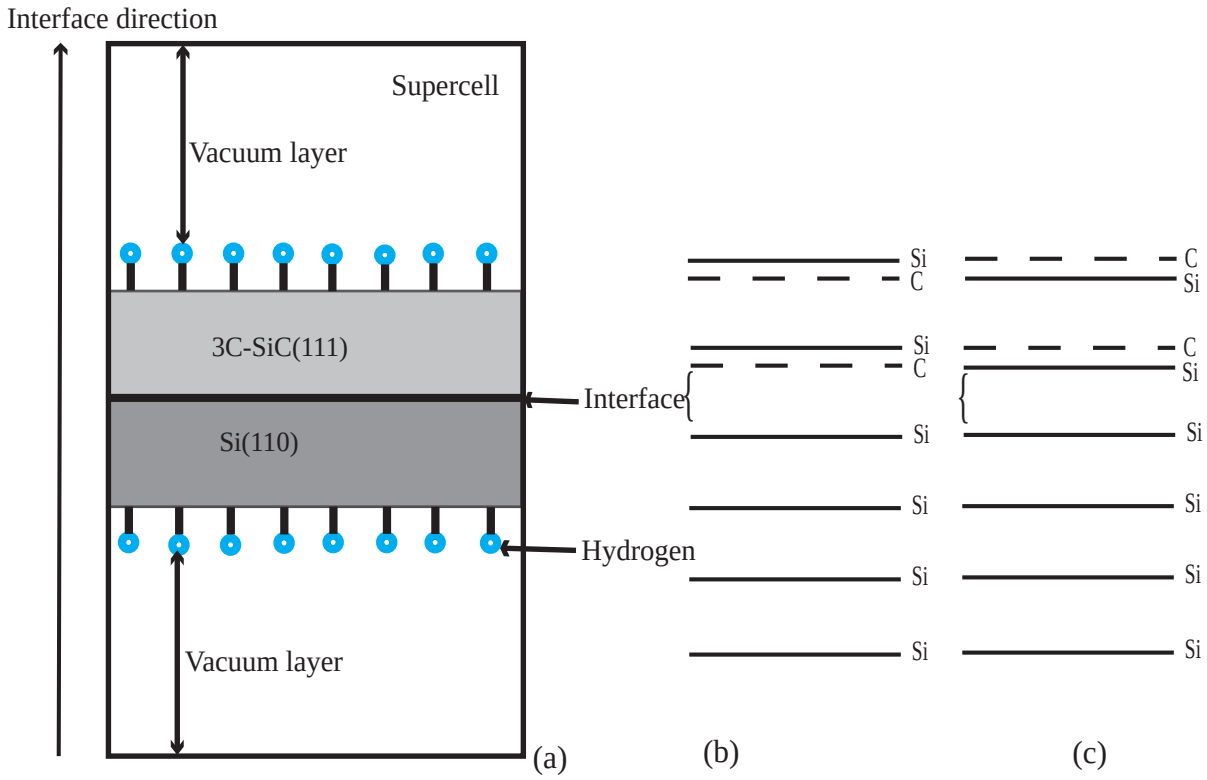

Figure 2.5: Schematic drawing of 3C-SiC(111) on Si(110) surface slab model cut out completely from both Si and 3C-SiC crystals and put together to construct the interface (a) interface slab model with hydrogen passivation on the outer surfaces of Si(110) and the 3C-SiC bulk terminated surface (b) interface where silicon face and carbon face meet form the Si-C interface (c) similarly interface where silicon and silicon faces meet form Si-Si interface. Small thick blue circles indicate hydrogen passivating the dangling bonds.

freedom. It is unknown the relative atomic positions of Si(110) face which meets 3C-SiC(111) face to form the interface system and secondly the interface separation between the two crystals together. This nobody knew before the present calculations and therefore we will determine by extensive total energy calculation in this thesis.

As for the separation between the two materials, we first assume Si-C and Si-Si bond distances as an initial interface separation and perform structural optimization to reach the most stable geometries. Of course the result converged with a number of atomic layers is the only meaningful quantity here. We perform careful convergence test and reached a conclusion that 8L/8L slab is sufficient enough to compute the real interface energy.

2.6 Mean atomic displacement

We treat the slab convergence as a function of mean displacement of relaxed atom position from the ideal per atomic layer. We separate the individual crystals for this treatment after relaxation accordingly.

$$\mathbf{d}_i^{\mathbf{A}} = \mathbf{R}_i^{\mathbf{A}} - \mathbf{R}_{i,ideal}^{\mathbf{A}}, \tag{2.145}$$

$$\triangle \mathbf{d}^i = \|\mathbf{d}_i^{\mathbf{A}}\| \tag{2.146}$$

$$\delta_{mean} = \frac{\sum \triangle \mathbf{d}^i}{N}, \tag{2.147}$$

where $\mathbf{R}_i^A$, $\mathbf{R}_{i,ideal}^A$ are the atomic position of the i-th atom in the relaxed and ideal structures and N is the number of atoms per layer in each component atomic layers. We find that N is 10 for 3C-SiC(111) side per atomic layer and 8 for Si(110) surface accordingly.

2.7 Integrated density and average potential

We analyze the charge density profile $\rho(x, y, z)$ by integrating it over x and y grid points as follows:

$$\tilde{\rho}(z) = \int \int \rho(x, y, z) dx dy, \tag{2.148}$$

which is a function of z-coordinate. we call this $\tilde{\rho}(z)$ "integrated density" hereafter. For example, integrated density of i-th Kohn-Sham wavefunction $\psi_i(x, y, z)$ is represented as:

$$\tilde{\rho}_i(z) = \int\int |\psi_i(x, y, z)|^2 dxdy. \tag{2.149}$$

In the same fashion, we use "average potential" $\tilde{V}(z)$ instead of $V(x, y, z)$ for analysis. The average potential $\tilde{V}(z)$ is defined as:

$$\tilde{V}(z) = \frac{1}{A}\int\int V(x, y, z)dxdy, \tag{2.150}$$

where A is the area of the base of the supercell.

Chapter 3

Energetics of Si(110) and 3C-SiC(111) Surfaces

In this chapter, we present atomic and electronic structure calculations of Si(110), Si- and C-terminated surfaces by real space density functional formalism. The systematic convergence of the above mentioned surfaces energies with corresponding relaxation is discussed. We shall similarly show the electronic structure properties of these surfaces and compare the results with experimental and other theoretical works whenever available.

3.1 Surface energy of Si(110) and 3C-SiC(111) crystals

Surface energy is defined as the work done required to separate a crystal into two parts along a given plane. The value of the surface energy of a crystalline solid is one of the most important fundamental quantities which characterizes a large number of physical phenomena. Among them are crystal growth, surface faceting, growth of thin layers and the shape of small crystallites. Due to their technological significance, a thorough microscopic understanding of their surface structures is highly desired. One of the fascinating problems concerns the equilibrium shape of nanocrystallites fabricated from solid state materials such as Si and 3C-SiC. The formation of self-assembled islands or quantum dots during the epitaxial growth of Ge on Si(100) [4, 77] and Si on α-SiC(0001) [78] is characterized by several distinct island shapes and unusual size distribution.

Apart from knowledge of the strain, the construction of the crystal shape requires com-

plete determination of the surface energy γ as a function of the surface orientation. In spite of its importance, there are few experimental data concerning surface energies due to the fact that they are difficult to measure [79]. By studying equilibrium shape of voids in silicon allows one to extract the surface energies for three orientations [110], [100] and [311] [80]. As for the 3C-SiC(111) surface energy, the experimental data available presently is obtained based on a simple formula similarly applied to lead chalcogenides with NaCl structure as carried out by Oshcherin [81].

There is almost a dearth of theoretical data available; the reason for this lack is that surface energy is very difficult to calculate. Calculation of surface energies are mainly restricted to semi-empirical methods such as tight binding approach [82, 83] or use of classical interaction potentials [84]. Surface energy values obtained from first-principles calculations are only available for 1×1 and 2×1 reconstructions of diamond surfaces [87–89] as well as for Si(111) and (100) surfaces [90–92].

Takai and coworkers calculated the surface energy of 3C-SiC(111) surface from empirical potential in conjunction with Monte Carlo procedure [85]. From the first-principles calculation view point, only Si(110) surface energy is reported [86] using planes basis set and no report on 3C-SiC(111) surface energy. It is therefore imperative we calculate the surface energies of Si- and C-termination of 3C-SiC and Si(110) surfaces to augment the existing data for comparison with real-space formulation.

3.1.1 Si(110) and 3C-SiC(111) surface energy determination

In order to model the two dimensional surfaces, a study within primitive surface cell of 1×1 translational symmetry should give the basic structural and electronic features of such surfaces. We consider periodic arrangement of slabs along the surface normal starting from 2-atomic layers and increase the slab thickness systematically to 20-atomic layers of Si(110) and 24-atomic layers (12-bilayers) of 3C-SiC terminated surface. The atomic layer is defined as a monoatomic layer of either (111) or $(\bar{1}\bar{1}\bar{1})$ surface plane of Si- or C-termination. The lattice constants are fixed to the theoretical equilibrium values of Si and 3C-SiC crystals. In each supercell, the number of atoms in a layer is restricted to the surface lateral cell. The slabs are separated by sufficiently thick vacuum regions. For Si(110) surface, two surfaces of the slab are symmetrically equivalent as shown in Figure

2.4(a) and allow for direct calculation of the surface energy. Another advantage is that the same surface reconstruction $n \times m$ occurs at both sides of the surfaces. However, this is completely different for the 3C-SiC terminated surfaces as indicated in Figure 2.4(b). With regards to the surface energy of Si(110) $n \times m$, we follow similar ideas used by Stekolnikov and coworkers [86] where none of the two equivalent surfaces of Si(110) is hydrogen passivated. Consider a given atomic geometry $\{\mathbf{R}_i\}$ in such a slab the surface energy $\mathbf{E}_{surf}^{n\times m}$ can directly be inferred from the total energy of the slab $\mathbf{E}_{tot}(N, \{\mathbf{R}_i\})$ with N atoms by subtracting N times the bulk energy $\mu_{Si(bulk)}$ per atom as:

$$\mathbf{E}_{surf}^{n\times m} = \frac{1}{2nm}\{\mathbf{E}_{tot}(N, \{\mathbf{R}_i\}) - \mu_{Si(bulk)} N_{Si}\}. \tag{3.1}$$

The presence of the chemical potential $\mu_{Si(bulk)}$ of the constituent atoms allows one to compare surfaces with different numbers of atoms in the 2D surface unit cell, where $n \times m$ in the case of reconstruction gives the number of 1×1 unit cells. The prefactor $\frac{1}{2}$ in equation Eqs. (3.1) indicates that the two surfaces of the slab are involved in the calculation. The surface energy per unit area is given by

$$\gamma^{n\times m} = \frac{\mathbf{E}_{surf}^{n\times m}}{A}, \tag{3.2}$$

which immediately follows by dividing expression (3.1) with the surface area A of 1×1 supercell surface orientation. Physically, $\gamma^{n\times m}$ is the energy increase due to dangling bonds. In principle, Eq. (3.1) and (3.2) gives the precise expressions applicable to arbitrary surface translational symmetries and reconstruction.

Now let us consider the surface energy of an inequivalent 3C-SiC(111) surface with lateral periodicity 1×1 which is equivalent to 3C-SiC($\bar{1}\bar{1}\bar{1}$). We define the surface energy as:

$$\gamma^{n\times m} = \frac{1}{A}\{\mathbf{E}_{tot}(N, \{\mathbf{R}_i\}) - \mu_{SiC(bulk)} N_{SiC} - \mu_H N_H\}. \tag{3.3}$$

Since the two surfaces are not equivalent, Eq. (3.3) is used to compute the surface energy. As we pointed out in the last section of chapter 2, there are two methods often used to calculate surface energy of inequivalent surfaces and unfortunately neither are accurate. The first approach is, one has to artificially impose inversion symmetry of which each

slab will actually consist of double slabs, the centre of which contains two planes of the same kind of atoms [76]. The other approach due to Käckell and collaborators [75], one of the two inequivalent surfaces is passivated with hydrogen leaving the other surface clean for surface energy calculation. This is what we have adopted because the goal is the convergence of the surface energy and not just a single calculation with sufficient thick slab to determine the surface energy. It is computationally inexpensive compared with the former. We find that the converged calculated results compare favorably well with other empirical calculations.

What we have done is that, each broken sp^3 bond at the bottom layer atom in either Si- or C-terminated supercell is saturated with hydrogen and lowest bilayer atoms together are kept fixed in order to hold the characteristics of a more realistic surface, while the rest of the atoms in the supercell are allowed to relax during the geometry optimization procedure. With all the model systems considered for 1×1 surfaces, we used 36 sampling **k** points in the lateral plane, that is, xy-plane of the Brillouin zone (BZ) (20-**k** points in the irreducible wedge by symmetry operation) are taken for the BZ integration. Only 1-**k** is used in the z-direction. The **k**-points meshes used are tested and sufficient enough to give accurate results after we performed **k**-point convergence test.

We determine the chemical potentials of $\mu_{Si(bulk)}$ and $\mu_{SiC(bulk)}$ pair from their corresponding bulk systems of Si and 3C-SiC by filling the vacuum regions with atoms in bulk positions and same slab orientation and size of the two-dimensional unit cells. We use 18-atomic layers for Si and 3C-SiC bulk in the supercell to calculate the chemical potential accordingly. In 3C-SiC(111) surface, H is attached to the C whereas it is attached to Si in 3C-SiC($\bar{1}\bar{1}\bar{1}$) surface. Therefore, the correct H chemical potential must be determined with respect to the corresponding environment. For this reason, we determine hydrogen chemical potential from SiH_4 and CH_4 by calculating their corresponding minimum energy. We calculate the H chemical potentials as follows:

$$\mu_{H_{Si}} = \frac{\mathbf{E}_{SiH_4} - \mu_{Si(bulk)}}{4}, \tag{3.4}$$

and

$$\mu_{H_C} = \frac{\mathbf{E}_{CH_4} - \mu_{C(bulk)}}{4}, \tag{3.5}$$

where $\mathbf{E}_{SiH_4}$, $\mathbf{E}_{CH_4}$, are the total energy per SiH_4 and CH_4 molecules respectively.

We calculate the chemical potential of C($\mu_{C(bulk)}$) with the same number of atomic layers as Si and similar calculation condition. It should be noted that, C has several allotropes and any one of them can be used in this work. There is no special reason for use of diamond crystal to determine C chemical potential. Using hydrogen chemical potentials calculated from Eq. (3.4) and Eq. (3.5), chemical potentials of Si, C and 3C-SiC crystals and all substituted in Eq. (3.3) depending on the particular surface of interest, we can evaluate the respective surface energies of Si- and C-terminated surfaces accordingly. In the same fashion, substituting chemical potential of Si into equation (3.1), the surface energy of Si(110) surface can be evaluated.

Figure 3.1 shows the dependence of surface energy as a function of slab thickness for a constant vacuum width of 12Å. The convergence for an infinite limit of Si(110) surface energy is quite rapid and smooth as indicated in Figure 3.1(a) but slight oscillation exists at the Si- and C-terminated surfaces as illustrated in Figure 3.1[(b) and (c)] respectively. It should be noted that the scale of Si(110) surface energy graph is quite different from the Si- and C-terminated surfaces graphs and not withstanding that, we confirm that Si(110) surface energy has no oscillation due to non-polarity of the surface. The 3C-SiC terminated surfaces under consideration are polar due to the electronegativity difference between Si and C atoms and therefore, charge transfer forces may be operational [85] which can be responsible for the observed oscillations and absent on Si(110) surface. While the Si-terminated surface energy monotonically decrease to convergence, that is not the case for C-terminated surface which appear to oscillate around a mean value. It is found that the surface energy per atom of the C-terminated surface is comparatively larger than that of Si-terminated surface.

As shown in Tables 3.1 and 3.2, the converged 1×1 surface energies of Si(110), Si- and C-terminated surfaces are summarized. We perform one calculation to determine the surface energies of the relaxed surfaces using 10-atomic layers for Si(110) surface and 9-bilayers or 18-layers for Si- or C-terminated surfaces. We observe in general that, quantitatively, the empirical calculations values are in better agreement with experiment than with first principles calculations. However, the present results are consistent with other *ab initio* calculations for Si(110) surface, but no available data exists for Si- and C-terminated surfaces for comparison.

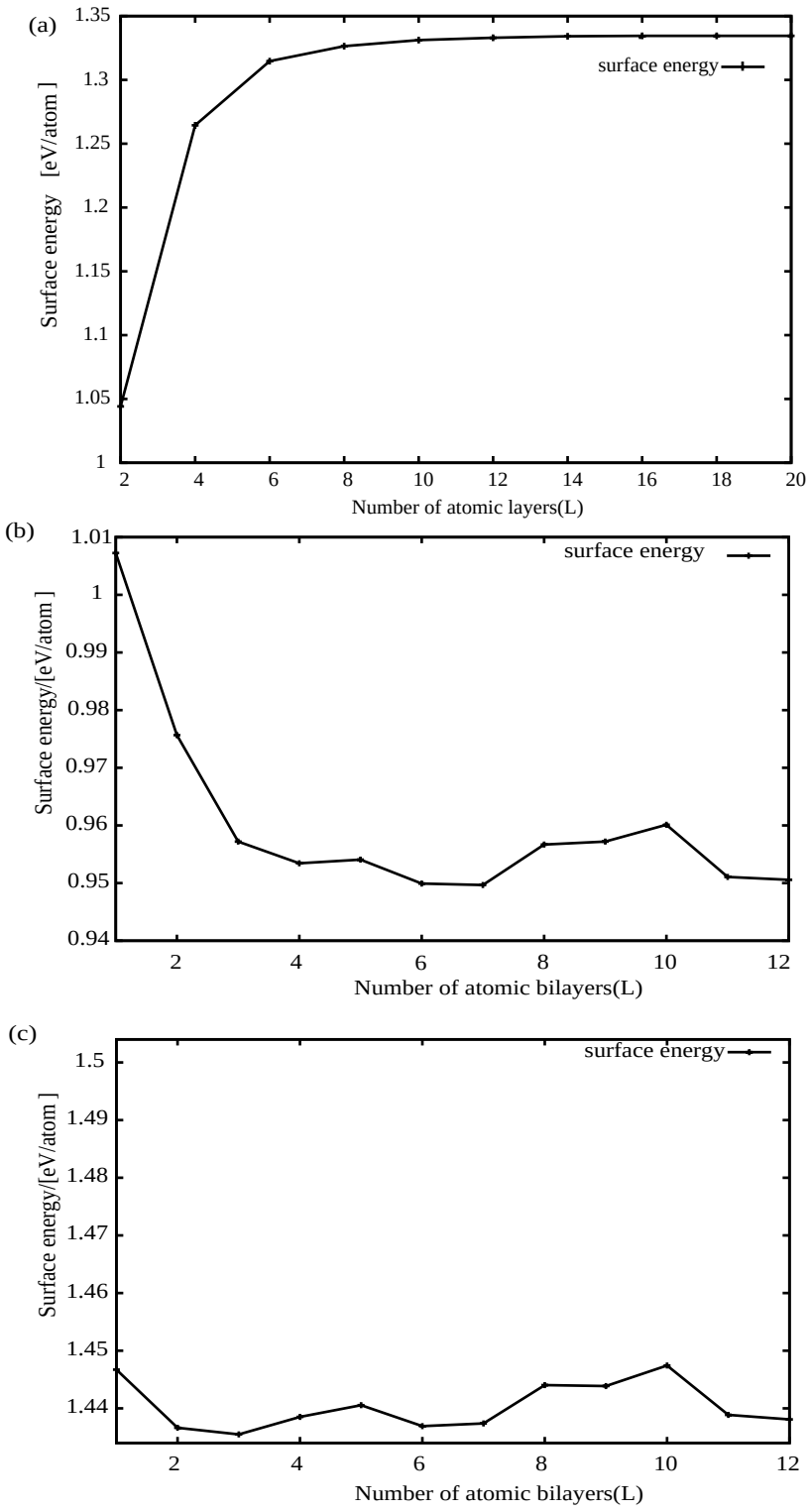

Figure 3.1: Variation of surface energy per atom as a function of slab atomic (layer for Si or bilayer for 3C-SiC) thickness of 1×1 cell (a) Si(110) (b) 3C-SiC(111) and (c) 3C-SiC($\bar{1}\bar{1}\bar{1}$) surface energies respectively.

Table 3.1: Calculated converged Si(110) surface energy per atom in eV or per area in mJ are indicated for 1×1 surface

Type of species:	Si(110) (mJm^{-2})	
Method of calculation	Unrelaxed	Relaxed
Empirical potential(MD)	1573[a]	–
Semi-empirical (TB bond order)	1721[b]	1573[b]
DFT(LDA)	2040[c]	1700[c]
RSDFT (LDA)	2100	1745
RSDFT (LDA) eV/atom	(1.334)	(1.111)
Experiment		1430[d]

[a] Reference [83]
[b] Reference [82]
[c] Reference [86]
[d] Reference [80]

Table 3.2: Calculated converged Si- and C-terminated surface energy per atom in eV or per area in mJ for 1×1 surfaces

Type of species:	3C-SiC(111) mJm^{-2}		3C-SiC($\bar{1}\bar{1}\bar{1}$) mJm^{-2}	
Method of calculation	Unrelaxed	Relaxed	Unrelaxed	Relaxed
Empirical potential	2525[e]	–	–	–
Semi-Empirical	2446[f]	718.4[f]	2584[f]	1767[f]
DFT (GGA-PW91)	2700[g]	–	–	–
RSDFT (LDA)	2856	1830	3065	2720
RSDFT (LDA) eV/atom	(0.951)	(0.910)	(1.438)	(1.272)
Experiment	–	2180[h]	–	–

[e] Reference [84]
[f] Reference [85]
[g] Reference [93]
[h] Reference [81]

3.2 Surface Relaxation

In this section, we present and discuss the results of atomic structure relaxation of non-polar Si(110) surface, polar (111) Si-terminated and C-terminated surfaces calculation using 10-atomic layers of Si(110) surface and 9-bilayers of the 3C-SiC terminated surfaces. Since atoms at surfaces are ideally truncated, they are under-coordinated, the surface atoms experience nonzero forces until they relax to new equilibrium positions. This is the process of surface relaxation. All atoms are allowed to relax completely in Si(110) surface while the bottom layer of Si- and C-terminated surfaces are fixed at their equilibrium positions. We find that relaxation of Si(110) surface involves both vertical and lateral

Table 3.3: Summary of cartesian coordinates of surface atom displacements from ideal position after atomic structure relaxation of Si(110)-i (where i=1, 2 represents the two equivalent surfaces), Si- and C-terminated surfaces. dE is the energy gain due to surface atomic relaxation per atom, and dH_n is the atom displacement from the ideal position in the lateral cell relative to the surface (where n=1, 2, 19, 20 indicates the surface atom of interest). Negative (or positive) sign represents inward (or outward) movement of a surface atom toward (or away from) the bulk position.

Surface atomic relaxation :

Si(110) −1 atoms :					
Displacement :		Δx[Å]	Δy[Å]	Δz[Å]	magnitude[Å]
dH_1		0.0841	-0.0019	0.2175	0.2332
dH_2		0.3753	-0.0034	-0.5432	0.6602
Si(110) −2 atoms :					
dH_{19}		0.1216	0.0002	- 0.2056	0.2389
dH_{20}		0.4079	-0.0009	0.5593	0.6922
dE[eV/surface atom]	0.219(0.220[a])				
3C-SiC(111) :					
dH_1		-0.0019	0.0025	- 0.1027	0.1027
dE[eV/surface atom]	0.094(0.090[b])				
3C-SiC($\bar{1}\bar{1}\bar{1}$) :					
dH_1		-0.0452	0.0106	- 0.1550	0.1618
dE[eV/surface atom]	0.343(0.300[b])				

[a]Refeference [98]
[b]Refeference [95]

displacement whereas the Si- and C- terminated (111) surface involves only vertical displacements due to the hexagonal symmetry of the lattice. In Table 3.3, we summarize the results of energy gain and atom displacements during the atomic structure relaxation.

Clearly, the two equivalent Si(110) surfaces show characteristic surface atomic relaxation feature of outward (away from bulk atoms) and inward motions of the two atoms in the 2D surface unit cell. These outward and inward atomic motions due to relaxations were first pointed out by Chadi [84,94]. With the two equivalent surfaces, the magnitudes of the relative outward displacements are almost identical. In the vertical direction, the two atoms move in the opposite direction which confirms the equivalence of the surfaces hence the energy gain by surface relaxation is halved per each surface.

For the (111) surface atomic relaxations, the C-terminated surface atoms exhibit relatively larger inward displacement and gain more energy over three times larger per atom than the Si-terminated surface atoms, and this is related to the difference in bond-bending and angular forces at the second-layer C or Si atoms from the surface. These results are

in very good agreement with Pollmann and coworkers who studied the relaxation of 6H-SiC(0001)1×1 surface atomic relaxation [95]. We compare these two surfaces because the first 4-bilayers of 6H-SiC(0001) is geometrically equivalent to the cubic structure.

In an unrelaxed surface atomic position, the Si(110) surface atoms each have a back bond in the sp^3 configuration. However after the surface relaxation, the new atomic rearrangements are such that the inwardly displaced atom has three bonds which are almost co-planar. For the (111) surfaces, each surface Si(C) atom is coordinated to three C(Si) in the layer underneath. The downward displacement suggest planar configuration rather than tetrahedral. As suggested by Lee and Joannopoulos, it is energetically favorable for an atom with s^2p^2 valence electronic configuration having three bonds to have a planar structure (sp^2 hybridization) and single electron in the p-state perpendicular to the plane. The (111) surface Si (or C) atoms, are therefore expected to undergo downward displacement toward a planar configuration with the next layer below atoms. Since the second-layer atoms are restricted by the bulk lattice, the surface atoms will not be able to assume an exactly planar geometry. Nevertheless, there will be an optimal vertical relaxation of the top layer, and the influence of the surface is expected to extend more than one layer into the bulk, with rapidly decreasing vertical displacements [96, 97].

We examine the surface relaxations of Si(110), Si- and C-terminated surfaces with respect to the average local potentials and the ideal surfaces. Perhaps if there is a significant departure of the average potentials from the bulk-like behavior due to the surface truncation or not. The average local potentials of these ideal and relaxed surfaces structures are shown in Figure 3.2. Where the vacuum levels are set to zero, $\bar{V}_{Si}$ and $\bar{V}_{SiC}$ correspond to the bulk Si and 3C-SiC local potential average values respectively. The local potential is averaged parallel to the surface normal as a function of the distance z-direction. The vertical lines as shown in the case of Si(110) surface graph indicate two equivalent surfaces, whereas for the C- and Si-terminated surfaces graphs, each of the vertical lines indicate the bottom most layer which is fixed. In all the surfaces considered, the vacuum levels are set to zero of energy. As one can observe, each of the Si(110) equivalent surfaces experiences same relaxation pattern as shown in Figure 3.2(a) on both sides. This is reflected in an equal amount of potential change due to the relaxation of the surface atoms. The maximum amount of atomic displacement of Si(110) surface atom is ~0.70Å. From the second layers of both sides of the surfaces away into the bulk, the potential assumes the

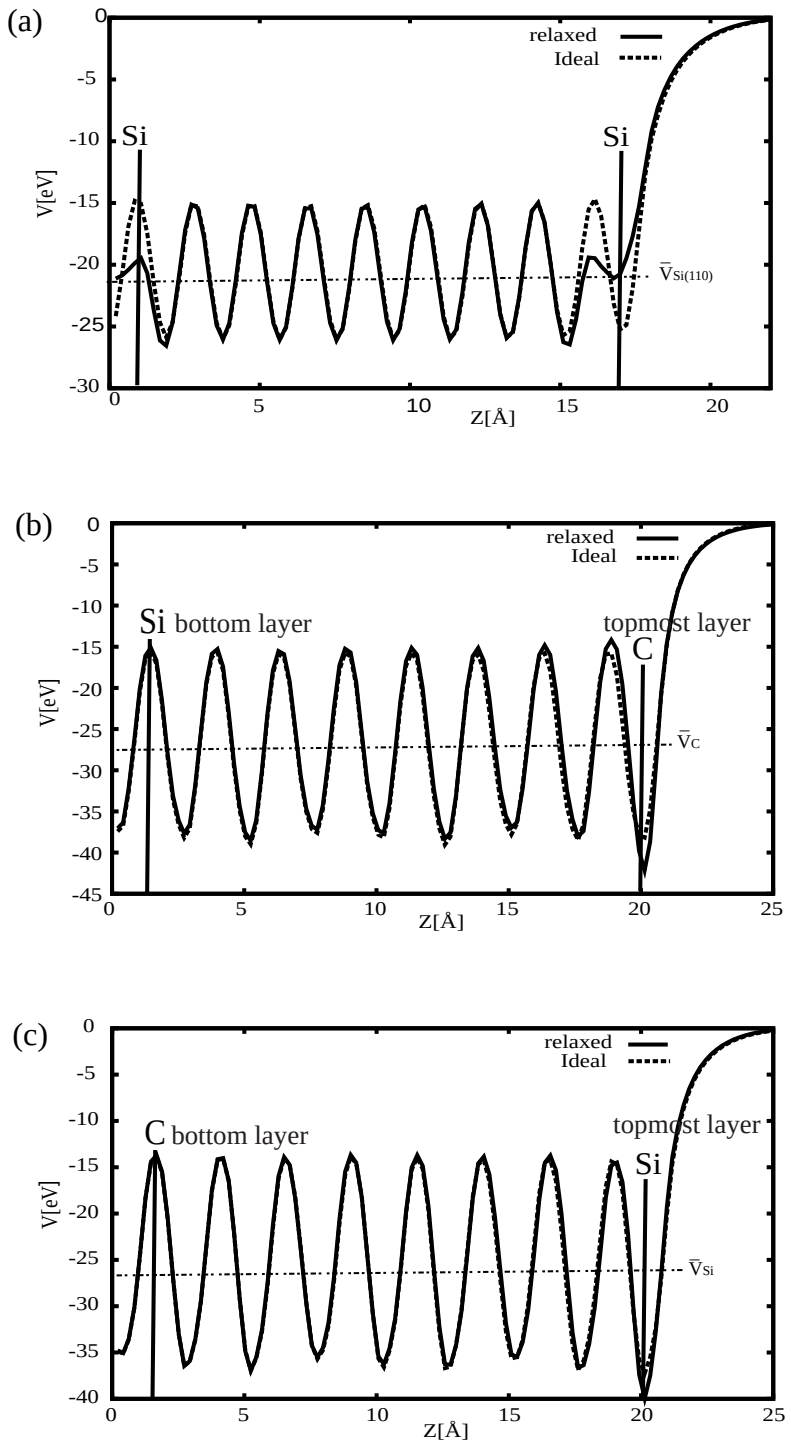

Figure 3.2: Average local potentials of 1×1 relaxed and ideal atomic surfaces: The solid and dashed lines indicate the relaxed and ideal average local potentials. The potentials are averaged parallel to the surface and plotted as a function of Z-component normal to the surface (a) Si(110) (b) 3C-SiC($\bar{1}\bar{1}\bar{1}$) and (c) 3C-SiC(111) surfaces respectively. Energies are in eV and vacuum levels are set to be zero.

form of the bulk. Even though all atoms are allowed to move during the relaxation, the bulk behavior is clearly visible.

As Figures 3.2 [(b) and (c)] show, the C- and Si-terminated surfaces average potential variation respectively. We observe that relaxation occurs slightly up to the third bilayers that is, the atoms in these layers slightly move from their equilibrium positions, but they remain relatively prominent in the first layers. The change is attributed to the polar behavior of these two distinctive surfaces. The potentials of 3C-SiC terminated surfaces already show bulk-like character in the deeper layers. However they reach the same value in the vacuum region for both relaxed and unrelaxed surfaces. The results indicate that the vacuum region is large enough to permit the full decay of the electron density.

3.3 Band dispersions of the surfaces

The different structural geometries influence the band dispersion of the surface structures. Their occupied parts give an explanation of the energetics discussed previously. The most important feature of Si(110) relaxation is the outward and inward motions of the two atoms in the surface unit cell. Occupied surface states near the valence-band maximum are associated with the outwardly relaxed atoms. In the same way, the empty surface states near the conduction band minimum arise from the inwardly relaxed atoms. Usually, the group IV semiconductors which show this kind of feature of raising and lowering atoms are referred to as anions and cations even though the same atomic species are involved [94]. Figure 3.3(a) represents the band dispersion of the clean relaxed Si(110)1×1 two equivalent surface with solid lines representing the bulk bands and the remaining lines showing dangling bonds bands. There are two dangling bonds per surface unit cell which leads to four bands in total located in the fundamental gap region for the two equivalent surfaces. We define D_{S1} and D_{S2} to represent two bands for each respective surface. Each dangling bond is half occupied because there are two atoms per surface unit cell. Clearly, we find that two pairs of bands are degenerate along the XM and $MX^{'}$directions and split at $\Gamma X'$ and ΓX. One remarkable feature is that, two dangling bonds are almost fully occupied and the other two almost empty re-enforceing the argument that the occupied states are related to the outwardly relaxed atoms while the inwardly relaxed atoms are related to the empty surface states. The Si(110) surface is a metal as expected.

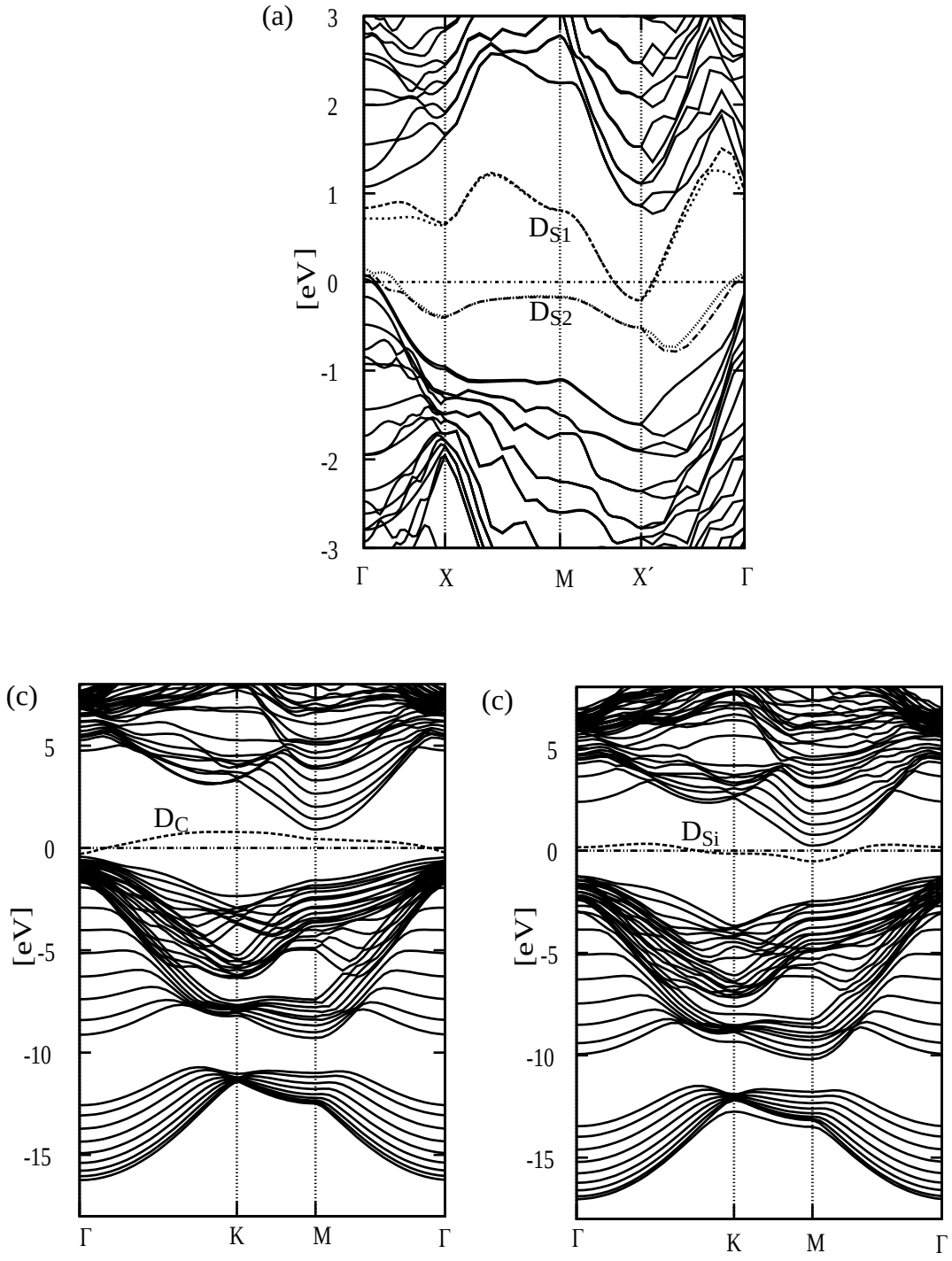

Figure 3.3: Surface band structures of the optimized 1×1 terminated surfaces of (a) Si(110) (b) 3C-SiC($\bar{1}\bar{1}\bar{1}$) and (c) 3C-SiC(111) respectively. Fermi energy level is set to zero of energy.

Table 3.4: Dangling bond energy positions

Relaxed (1×1)	C-terminated D_C[eV]	Si-terminated D_{Si} [eV]	Relative position [eV]
3C-SiC(111)	0.288	1.418	1.130
6H-SiC(0001)	-	-	1.500[a]

[a]Refeference [95]

Similarly, Figure 3.3[(b) and (c)] indicates the surface band dispersions of the relaxed C- and Si- terminated surfaces. The relaxed C- and Si-terminated surfaces each has one dangling bond with corresponding band located in the band gap region. These dangling bonds bands are indicated as D_C and D_{Si} and originate from the localized C or Si top layer atom respectively. Each dangling bond band is partially occupied since there is only one top layer atom per 1×1 unit cell in both surfaces. The resulting band structures are thus metallic. Comparing the energetic positions of D_C and D_{Si} located at 0.29 and 1.42 eV respectively, it is evident that D_C occurs approximately 1.13 eV lower in energy than D_{Si} which is due to the stronger C potential, as compared to that of Si potential first suggested by Pollman and coworkers when they calculated the surface states of $\alpha - 6H(0001)$ [95]. This suggests that, 3C-SiC(111) and $\alpha - 6H(0001)$ hexagonal surfaces are symmetrically identical but electronically different due to the difference in dangling bonds energy positions. The dispersion of this dangling bond band D_{Si} is more pronounced than that of D_C, because D_{Si} is laterally more extended. Obviously, the dangling bonds are predominately localized at the top layer atoms and oriented perpendicularly to the surface making both surfaces metallic.

3.4 Summary

In conclusion of this chapter, we performed total-enegy electronic structure calculations based on real space density functional theory that provides firm theoretical foundation to discuss the surface energies of Si(110), 3C-SiC(111) and 3C-SiC($\bar{1}\bar{1}\bar{1}$) terminated surfaces respectively. We systematically converged the surface energy of Si(110) surface and find it to be 1.334 eV/atom (2100 mJm^{-2}) for unrelaxed and 1.111 eV/atom (1745 mJm^{-2}) for relaxed surfaces. We find that the results are in excellent agreement with other first

principle calculations. However, when the relaxed surface energy value is compared with experiment we find an overestimation of about 22%. Similarly, we calculated for the first time the relaxed surface energies of C- and Si-terminated polar surfaces of 3C-SiC using density functional theory. The calculated values are 1.272 eV/atom (2720 mJm^{-2}) and 0.910 eV/atom (1830 mJm^{-2}) respectively for C- and Si -terminated surfaces, the disagreement in these calculations compared with experiment are 24% and -16% accordingly. The ideal converged surface energies for both surfaces are also calculated. It has been remarked elsewhere that charge transfer can be operative for C- and Si-terminated surfaces owing to their polar character. However Si(110) surface is not polar and therefore the exact cause of the large differences in the calculated surface energies compared with experiment is not understood yet. Therefore, caution should be taken in the interpretation of these values. The relaxation pattern of the 3C-SiC(111) surface is similar to the $\alpha - 6H(0001)$ owing to the same symmetry similarity between the two surfaces.

We find that owing to the presence of dangling bonds, all the surfaces investigated in this work exhibit metallic behavior. Of much interest is the dangling bond positions of the Si- and C-terminated surfaces. We find that the relative energy positions of D_{Si} with respect to D_C is about 1.13eV making it different from $\alpha - 6H(0001)$ surface as reported by Pollman and collaborators as 1.5eV [95]. This further indicates that indeed, electronic structures of the alpha and cubic silicon carbide terminated hexagonal surfaces are symmetrically identical, but they are not the same electronically owning to the difference in the relative dangling bonds positions.

Chapter 4

Atomic and Electronic Structures of Si(110) on 3C-SiC(111) Surface

In this chapter, we shall explain the calculation method of 3C-SiC(111) on Si(110) surface. We report total-energy electronic structure calculation results based on real-space density functional theory scheme which elucidates new atomic and geometric properties of the interface systems. We shall give detailed analysis of the relaxed interface structures, energetics and electronic properties. We conclude with the result of pre-relaxed 3C-Si(111) surface and Si(110) surface put together to form interface geometry and then perform atomic structure calculation for comparison.

4.1 Interface structural models

As already been explained in Chapter 1, there is significant lattice mismatch between 3C-SiC and Si as large as 20% making it impossible for epitaxial growth to take place between the two crystals. However, Nishiguchi and collaborators [34] discovered a special crystallographic orientation such that the two crystals can match for epitaxial growth to occur but this matching is fake. They found that at certain periodicity, the crystal plane of 3C-SiC(111) surface could grow on the substrate of Si(110) crystal plane with minimal lattice match. They deduced that separation of Si atoms along the Si[001] direction on the Si(110) surface agrees with the separations along the direction $[\bar{1}\bar{1}2]$ on 3C- SiC(111) plane with a deviation of 1.6%. That is, along the Si$[\bar{1}10]$ direction 4-time periodicity

Table 4.1: Lattice vectors of the supercell of the fake lattice matched geometry of Si(110) on 3C-SiC(111) surface. All values are in angstrom.

vector	direction[Si][3C-SiC]	norm	x	y	z
$\mathbf{a_1}$	[001][$\bar{1}\bar{1}$2]	5.372	5.372	0.000	0.000
$\mathbf{a_2}$	[$\bar{1}$10][$\bar{1}$10]	15.195	0.000	15.192	0.000
$\mathbf{a_3}$	[110][111]	33.983	0.000	0.000	33.983

agrees with 5-time periodicity of 3C-SiC[$\bar{1}$10] direction on the 3C-SiC(111) plane to become 0.2% mismatch.

We then assume lateral unit cells of Si(110) and 3C-SiC(111) surfaces as shown in Figure 4.1[(a) and (b)] with surface perpendicular into the paper. To construct the interface model of 3C-SiC(111) on Si(110), the two surfaces must commensurate to reduce undue stress on the crystals and to avoid artifact relaxation. We choose vectors $\mathbf{a_1}$ and $\mathbf{a_2}$ in the lateral plane and the additional vector $\mathbf{a_3}$ perpendicular to this plane. We indicate in Table 4.1 the vectors with the directions of Si and 3C-SiC terminated surfaces used to construct the supercell. The interface structure of 3C-SiC(111) on Si(110) is simulated by repeating interface slab model in which an atomic slab consisting of atomic layers is arranged periodically in the direction perpendicular to the layers with 8Å vacuum thickness (chosen after test) between interface slabs as illustrated in Figure 2.5(a). For visual understanding of the two types of interfaces considered, Figure 4.2 shows the unrelaxed stick and balls construction of 8L/8L 3C-SiC(111) on Si(110) surface models of Si-C and Si-Si interfaces. In all interface calculations, the outer surfaces of the supercell are hydrogen passivated.

For detailed calculations, first is the determination of relative atom positions in the lateral plane of 3C-SiC(111) on Si(110) substrate. It is a very hard task to determine the stable structures of many degrees of freedom. In this regard, the strategy we adopted is to introduce grid on the surface primitive cell (this contains all space) of Si(110) surface as shown in Figure 4.1(c) and choose at least nine geometries (actually each site atom on a grid point is associated with several equivalent site atoms when viewed from the 3C-SiC(111) surface) with top and bottom surface dangling bonds saturated with hydrogen. We prepare 4-atomic layers of each 3C-SiC(111) on Si(110) surface to construct the 4L/4L supercell as prototype interface. The calculation model is schematically shown in Figure 4.3(a). The purpose of this calculation is to obtain the optimized interspacing distance between 3C-SiC(111) on Si(110) surface for realistic interface calculation when the

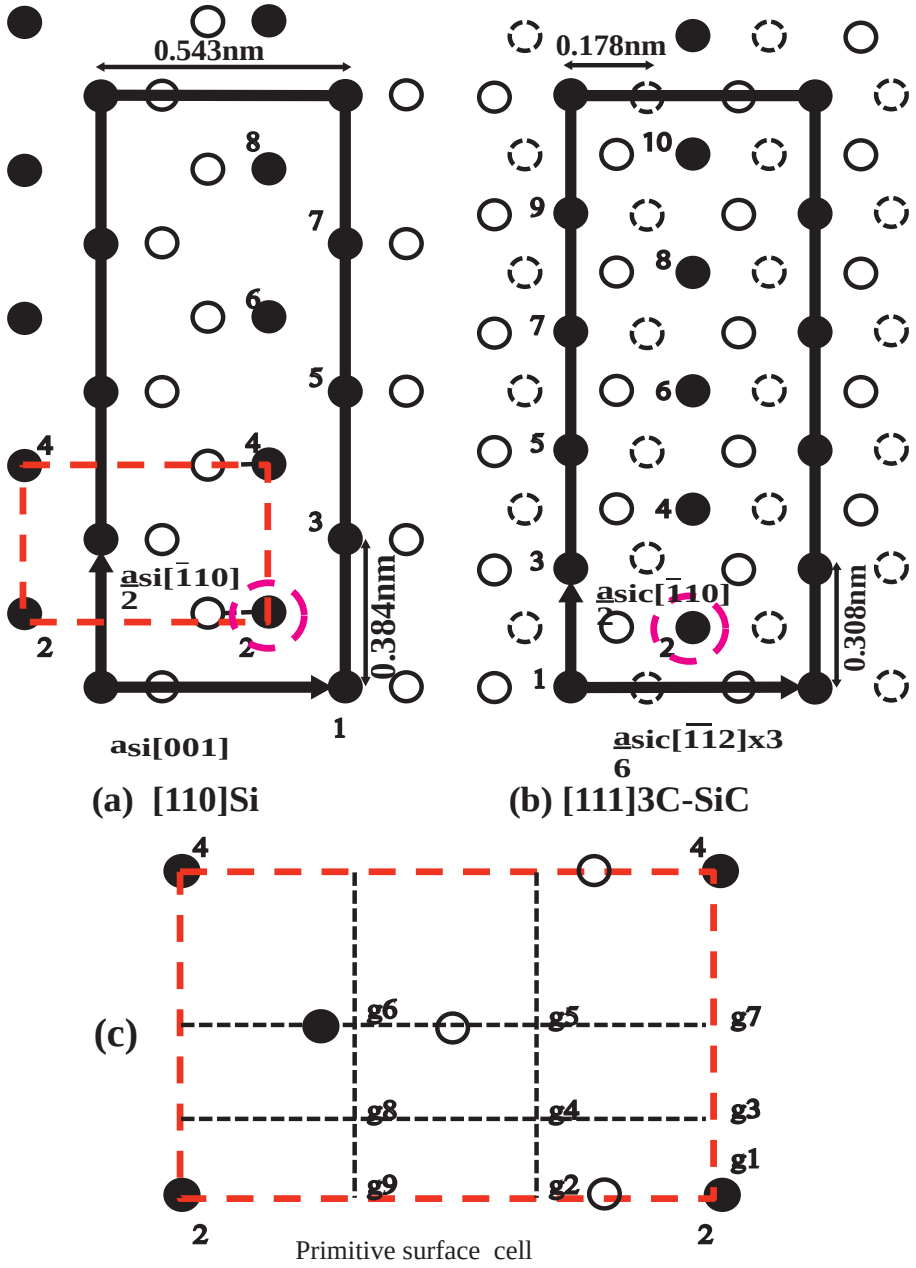

Figure 4.1: The schematic atomic projections of {(a) [110] Si and (b) [111] 3C-SiC} with label numbers indicating the very topmost surface atoms and (c) enlarged primitive surface cell of Si(110) surface showing grids (g_i,i= $1, 2, 3, \cdots 9$) points along which 3C-SiC(111) are used to search for stable interface geometry. Solid black, circles and hatched circle represent first, second and fourth atomic layers of each surface which exist within the same plane.

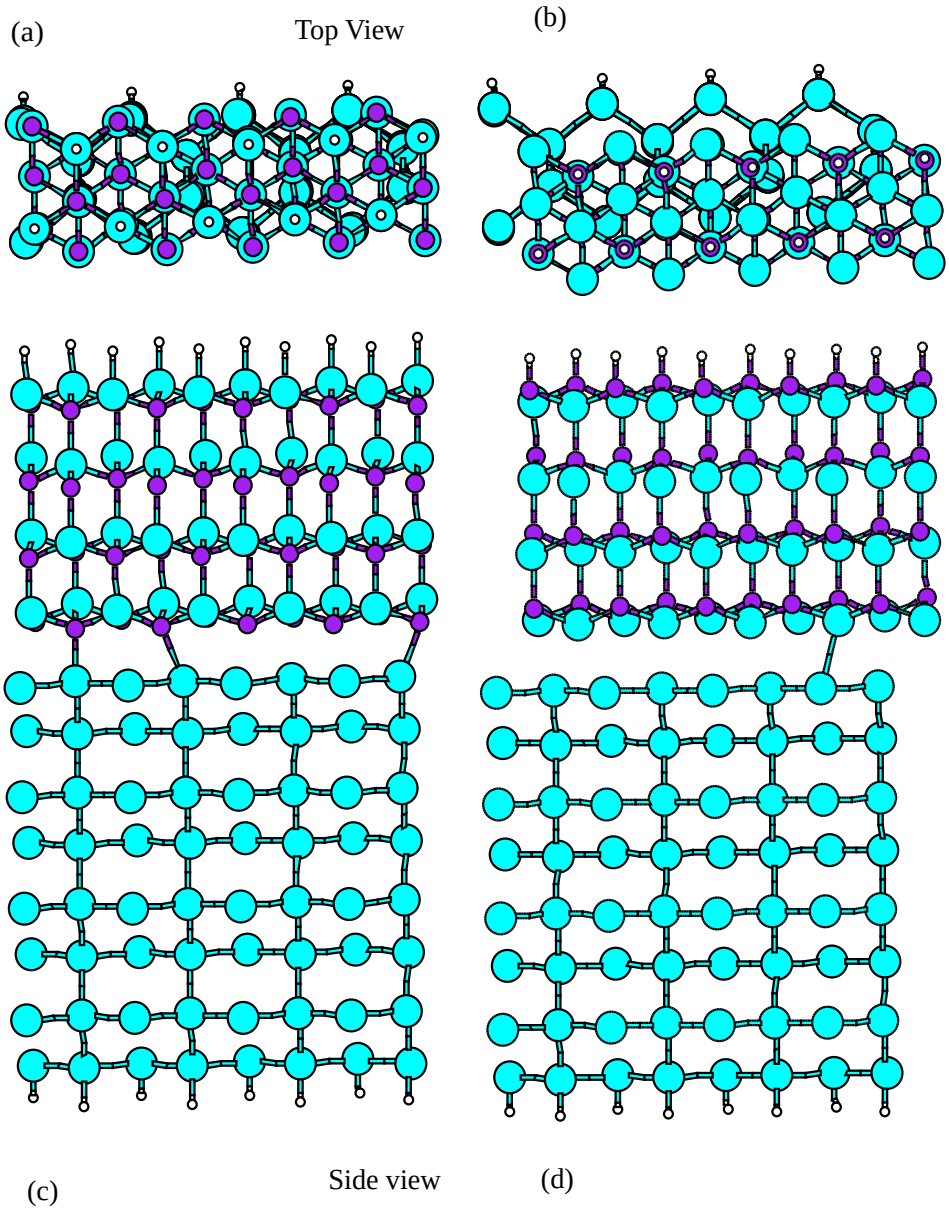

Figure 4.2: 3C-SiC(111) on Si(110) surface with 8L/8L atomic layers prepared using stick and balls to illustrate the interface atomic configurations. The figures show top and side views of Si-C [(a) and (c)] and Si-Si [(b) and (d)] interfaces. Interface distances are set based on ideal bond length. In this figure and all other interface related figures cyan, purple and white spheres which indicates respectively silicon, carbon and hydrogen atoms.

atomic layers are increased. For this reason, we set the initial distance of 3C-SiC(111) on Si(110) surface depending on the type of interface, according to the theoretical bond distance of either Si or 3C-SiC bulk crystal for Si-Si or Si-C interfaces respectively. Finally, the determination of the relative atomic positions yielded two most stable geometries which are bistable. We called them type I and type II interfaces. In all, four geometries are found two for each Si-Si interface and Si-C interface accordingly.

We then increased the number of atomic layers to 6L/6L and performed two different types of calculations as shown in Figure 4.3(b) starting from the initial position of 4L/4L structure that gives the minimum energy. For the first calculation, the bottom layer of Si(110) including attached hydrogens are kept fixed to simulate the semi-infinite bulk region whilst the other remaining atoms in the supercell are optimized completely. In the second calculation, we allow every atom to relax just like the case of 4L/4L calculation. The aim of this two 6L/6L calculations is to compare the relaxation pattern and the interface distance between the 3C-SiC(111) on Si(110) and those of the 4L/4L if significant difference exists. We find that the two calculations performed for 6L/6L relaxation patterns are not significantly different near the interface as well as the interface distance. Following that, we increased the system size to 8L/8L starting from the same initial atoms positions as 4L/4L system. In these calculations, we fix the top and bottom layers as well as the attached hydrogen as indicated in Figure 4.3(c) and relax the remaining atoms. With regards to the interface distance for this calculation, we find that using the ideal bond distance values or the optimized interface distance of 6L/6L system for the 8L/8L supercell calculation, the relaxation patterns near the interface remain unchanged. This is because the observed interface distance differs by less than ~0.03Å.

After careful testing, we find that 2**k**-points for the Brillouin zone (BZ) integration are sufficient to assure a reliable calculation. One **k**-point is located at the centre and the other at the edge of the (BZ). The optimized geometries obtained for all calculations are shown in Figures 4.4 for type I interface geometries and Figure 4.5 for type II interface geometries appropriately. As we have pointed out before, converged atomic layers are the only important quantity to discuss a realistic system. We perform careful convergence test with these three slabs models and reach a conclusion that 8L/8L slab is appropriate enough to describe the real interface structure using equation (2.147). The final results are shown in Figure 4.6 which indicates the mean displacement of the relaxed atoms

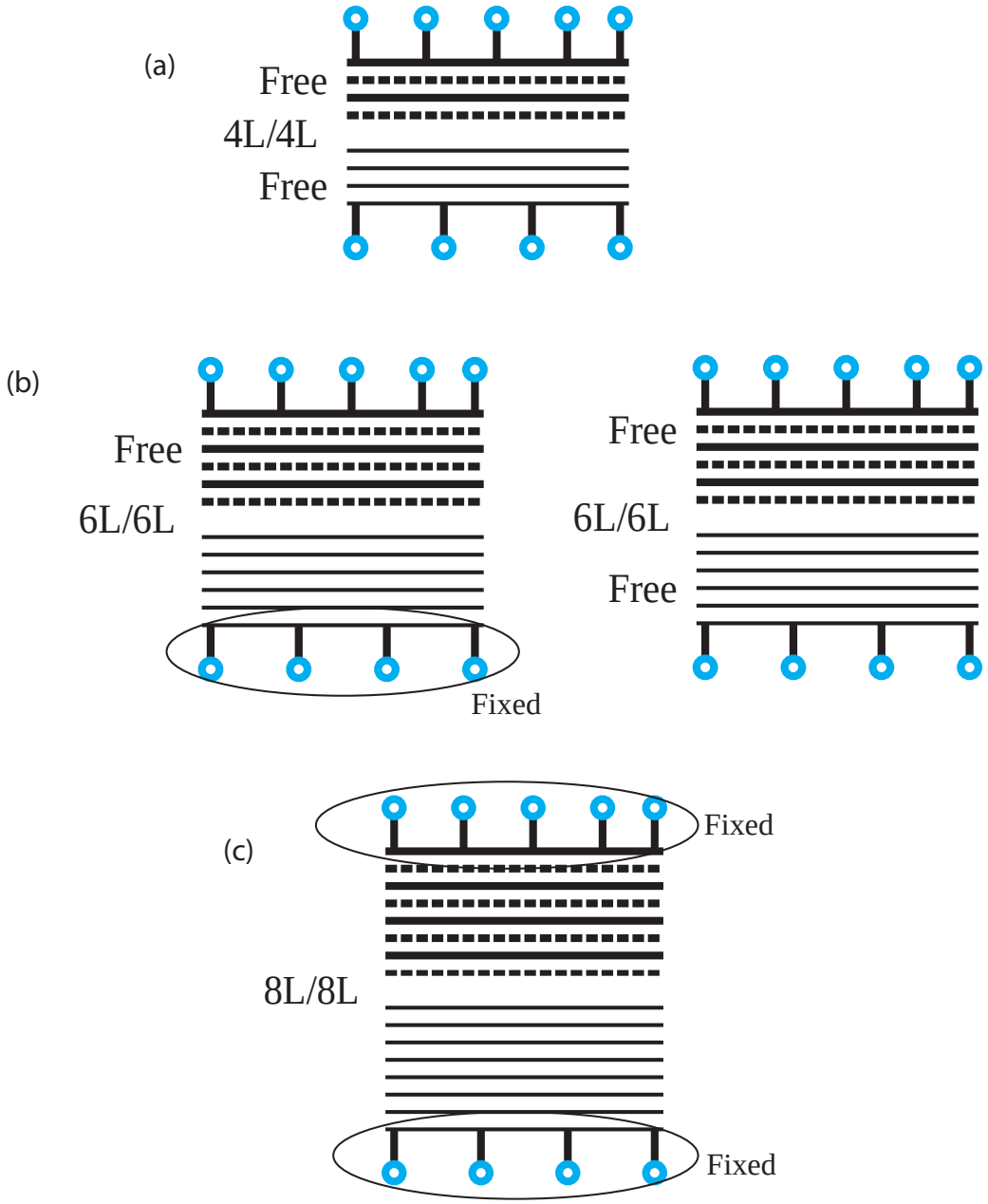

Figure 4.3: Schematic representation of 3C-SiC(111) on Si(110) surface calculation models (a) 4L/4L as prototype (b) 6L/6L (c) 8L/8L for Si-C interface (when the layers are reversed Si-Si interface is obtained). These two set calculation models are carried out separately. 'Free' here means all atoms in supercell are allowed to move whereas 'Fixed' indicates the bottom atomic layer is restricted including the attached hydrogen. Small thin and large continuous lines represent Si atomic layers in Si(110) and 3C-SiC(111) region and hatched lines indicate C atomic layers in 3C-SiC(111).

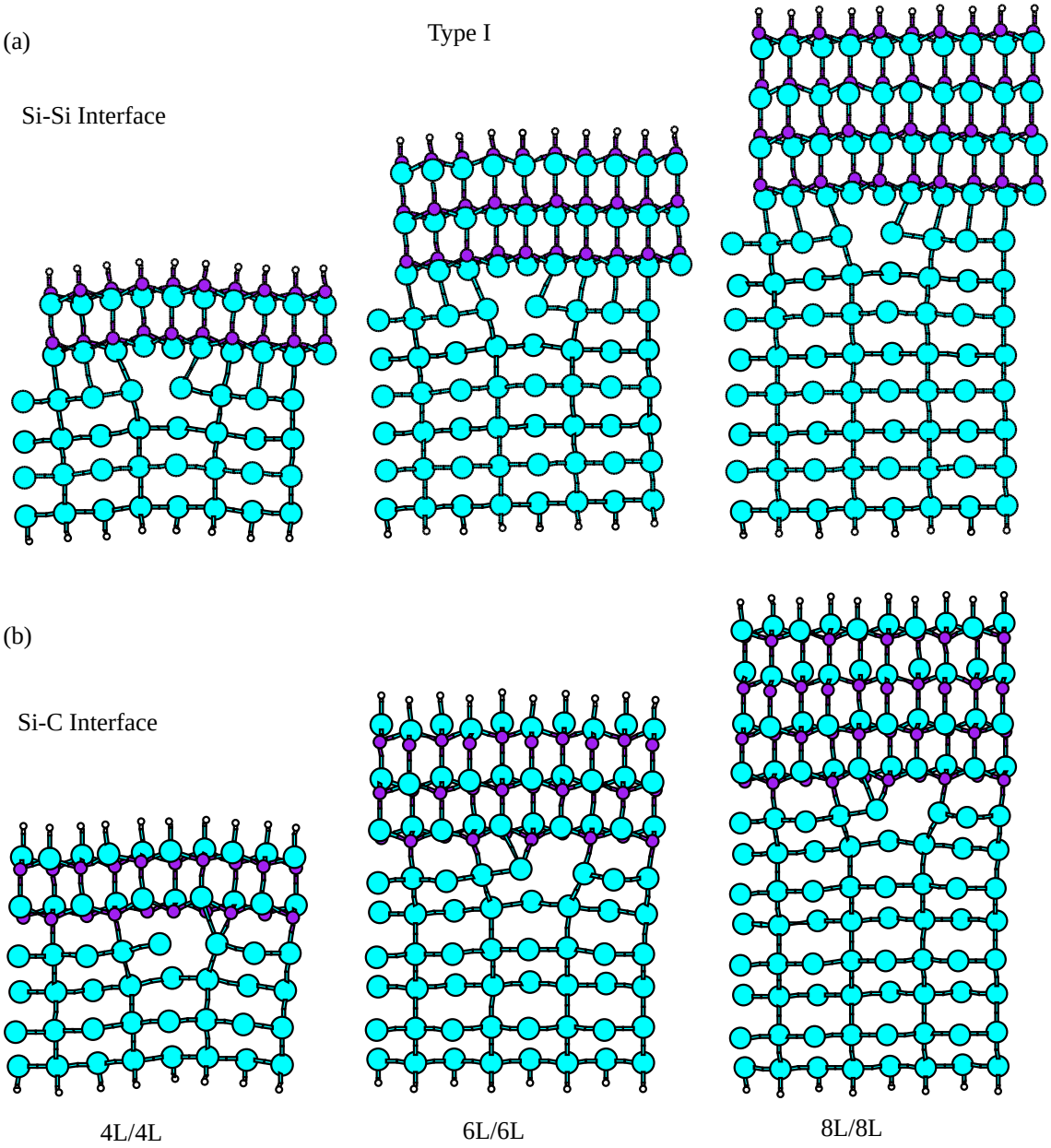

Figure 4.4: All relaxed geometries of type I interfaces (a) Si-Si interface (b) Si-C interface of 3C-SiC(111)/Si(110) respectively.

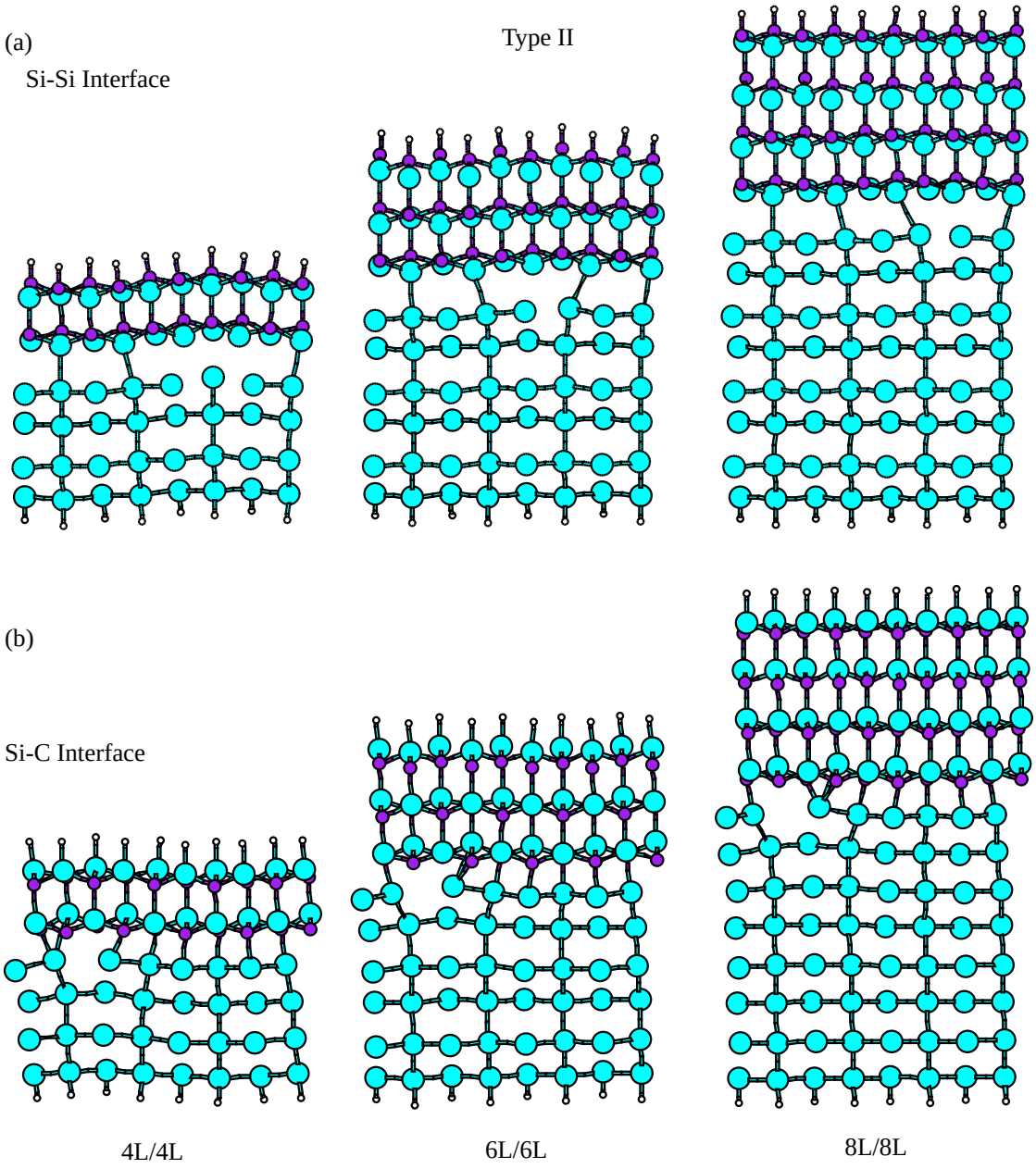

Figure 4.5: All relaxed geometries of type II interfaces (a) Si-Si interface (b) Si-C interface of 3C-SiC(111)/Si(110) respectively.

from the ideal atoms positions as a function of the atomic layers of the two separate crystals. One can see from the displacements graphs that, the very first layer near interface experiences the most displacements and decreases as the atomic layers increase. The 7th layer displacements in Si(110) and the 6th layer displacements in 3C-SiC(111) surfaces from the ideal positions are small less than 0.1Å. This displacement value is small enough to discuss the convergence of each individual bulk structures in 8L/8L system since LDA cannot provide accuracy better than this. It is important to recognize that, the 8th layer of Si(110) surface and the 4th bilayer of 3C-SiC(111) surface are held fixed, therefore atomic displacements in these layers are zero.

4.2 Effects of interfacial relaxation

We have performed extensive first principles calculations to search for the relative stable atomic positions of the heterostructure configuration of 3C-SiC(111) on Si(110) surface. We explored several candidate geometries and reached two distinctive types called type I and type II after atomic geometry optimizations and find that they are bistable as depicted in Figure 4.4 and Figure 4.5 for the respective interface geometries with corresponding energy differences listed in Table 4.2 of the various interface layers considered. As one can see, the energy differences varies depending on the thickness of the interface layers.

We find that near the interface, atom bond distances and interface pair connecting atom distances are in the range of (1.80~2.08)Å on the 3C-SiC(111) surface side and (2.29~2.38)Å on the Si(110) surface side. The bond distances in these ranges are characteristically found almost within 4-atomic layers. For the deeper layers, the bond distances are very much similar to the respective equilibrium bulks. In general, the number of 3C-SiC (111) or 3C-SiC($\bar{1}\bar{1}\bar{1}$) terminated surface atoms concentration at the interface are dense compared with those of Si(110) surface atoms which are sparse. For this reason,

Table 4.2: List of energy differences between the bistable type I and type II geometries of Si-C and Si-Si interfaces respectively. The values are in eV per supercell.

	Si-C interface	Si-Si interface
4L/4L	0.1079	0.1252
6L/6L	0.0057	0.1251
8L/8L	0.4372	0.3229

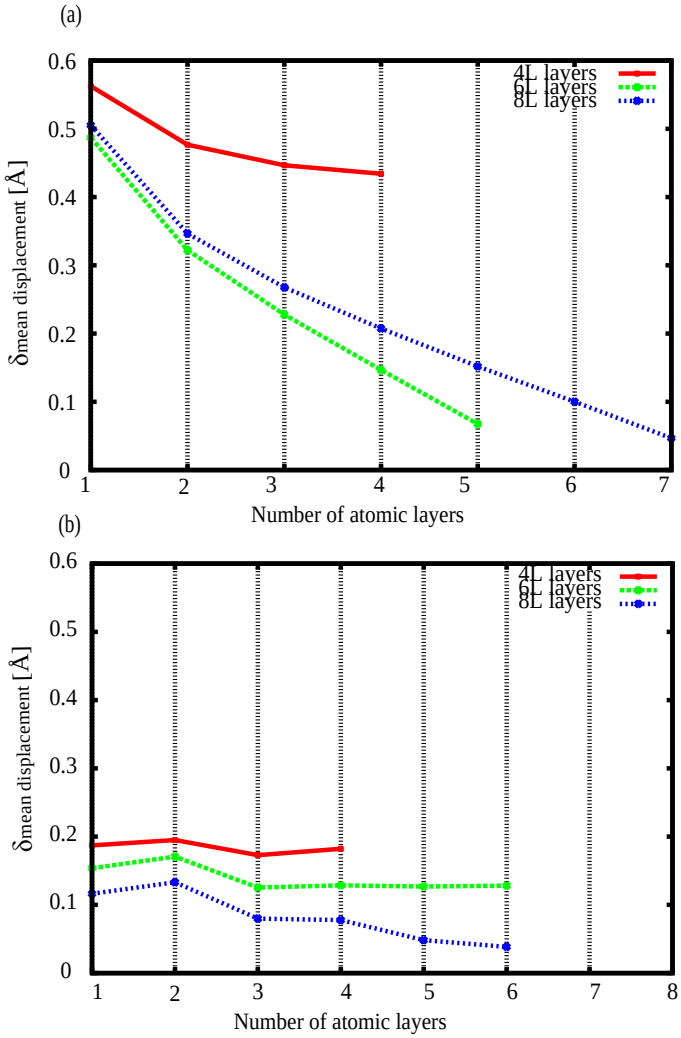

Figure 4.6: The convergence test for minimum atomic layers needed to perform realistic interface calculation. The mean displacement of atom coordinates from the ideal positions as dependence of atomic layers of 3C-Si(111) on Si(110) surface after relaxation (a) Si(110)-side and (b) 3C-SiC-side. Note, only the Si-Si interface supercell calculation is indicated.

one of the most striking observable effects resulting from the first-principles calculation is the pronounced undulation as an intrinsic feature near the interface. The noticeable undulation effect can be observed about 4-atomic layers of the constituent slabs. This suggests that, probably the interface is not flat at the atom level since the experiment [34] can not probe into such thin layer structures. An important pronounced effect is the breaking of exactly one Si(110) surface atom nearest neighbor (NN) bond in this model.

The reason for this effect can be explained that there is large difference in angular forces occurring at the interface constituent atoms when the tetrahedral bonds to their nearest neighbour become bent upon interface relaxation and this might be the case in the present work. The force is much larger at 3C-SiC(111) surface compared with the Si(110) surface atoms so that structural changes at the interface tetrahedral configuration around C atoms involve a much larger contribution of strain during the relaxation than around Si atoms at the respective junction. That is, the Si-Si bond bending is more flexible compared with Si-C at the interface. In general, 3C-SiC crystal is a very strong material compared with Si crystal. This is because the bulk modulus of 3C-SiC is about 2.3 times larger than Si. Therefore, matching these two materials will result in bond bending and the overall effect is what appears as the undulation near the flexible Si(110) side.

To confirm the bond breaking at the interface, Figure 4.7 depicts the optimized interface structures and the isosurface of the total electron density of the interface structures under consideration. From the spatial distribution of the electron density, we find that the electron densities symmetrically distribute between the neighboring atomic bonds as usually seen in a typical sp^3 hybridized materials. However the electron densities around the broken bond area at the interface varnishes compared with the other atomic bonds. It is interesting that the bond breaking creates a hole perpendicular to the interface around which spatial distribution of electrons occurs. This new bonding re-arrangement of electrons results in an energy gain. We believe the bond breaking is necessary and that it might relate to the effect of lattice mismatch. We speculate that the combined effects of the observed undulation and bond breaking near the interface are likely to be one of the factors responsible for the reported stacking faults and twinning during the carbonization process of the growth, which depends on the flow rate of the source gas [34].

SiC is a group-IV semiconductor compound and ionic, the ionicity of 3C-SiC amounts to g=0.475 compared with Si on Garcia-Cohen scale [99]. The ionic character of the

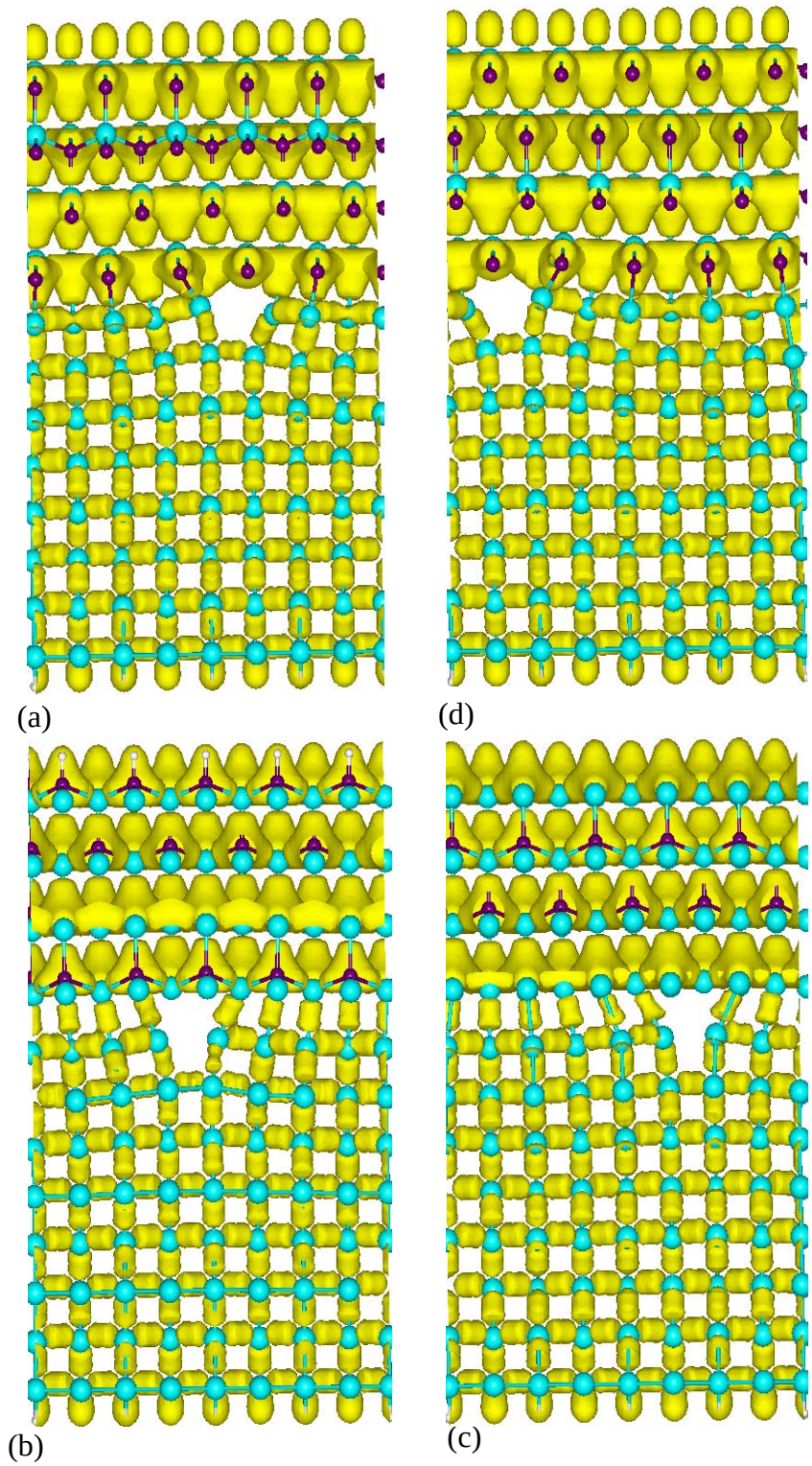

Figure 4.7: The optimized atomic structures of 8L/8L 3C-SiC(111) on Si(110) surface and the corresponding isosurface of total electron charge density of [(a) Si-C and (b) Si-Si] of type I and [(c) Si-C and (d) Si-Si] of type II interfaces respectively. The absence of charge density near and around the broken sp^3 bond of Si(110) side nearest neighbor atom creates defect hole. The contour value is 25% of the maximum.

SiC bond stems from the different strengths of C and Si potentials which result in very different covalent radii. Also, the electronegativity of C (e_C=2.5) is considerably larger than that of Si (e_{Si}=1.7). The stronger C potential as compared with that of Si leads in SiC to a charge transfer from Si to C so that the electronic charge density distribution along the SiC bond is asymmetric [95]. The Si atoms act as cations while C atoms act as anion in 3C-SiC in the crystal. In this regard it is expected that, the heterojunction of Si-C or Si-Si interfacial charge distribution should not significantly differ from the bulk 3C-SiC or Si. Clearly, the charge distribution on the 3C-SiC side is not like the characteristic sp^3 type hybridization compared with the Si side. This might relate to the ionic character of the 3C-SiC(111) surface.

For the model interface systems, it should be noted that both Si- or C-terminated surface each has ten atoms and same number of dangling bonds (DB) directed perpendicular to the surface in the same fashion as that of H passivated surface region as shown in Figure 4.2. Similarly the Si(110) surface has eight atoms with same number of DBs, four of the DBs are directed away from the remaining four. When the 3C-SiC(111) surface is put on top of the Si(110) substrate, the effective DBs at the interface when the bonds are connected after relaxation are always two coming from the 3C-SiC(111) surface side in this model. Because DBs coming from different slabs are directed differently, implies during relaxation, interface atoms which try to connect to form a bond experience different residual angular force with Si-C interface being the least flexible because silicon carbide bonds are much difficult to bend than silicon bonds. This could be one of the plausible reason why the Si-Si interface energy is always minimum compared with the Si-C interface.

4.3 Interface Relaxation mechanism

As we noted in section 4.2, Figure [4.4 and 4.5] shows the relaxed structures of Si-C and Si-Si interfaces of both type I and type II relative atom positions. In both interface structures, we observe that near the heterojunction undulation persists and is basically due to the difference in the number of 3C-SiC(111) surface dense atoms and Si(110) surface sparse atoms. It is established that for (111) and (110) interfaces, strains reduce the crystal symmetry in such a way that the separation of the two atoms in the bulk primitive unit cell of diamond or zincblend structures is not uniquely determined from macroscopic

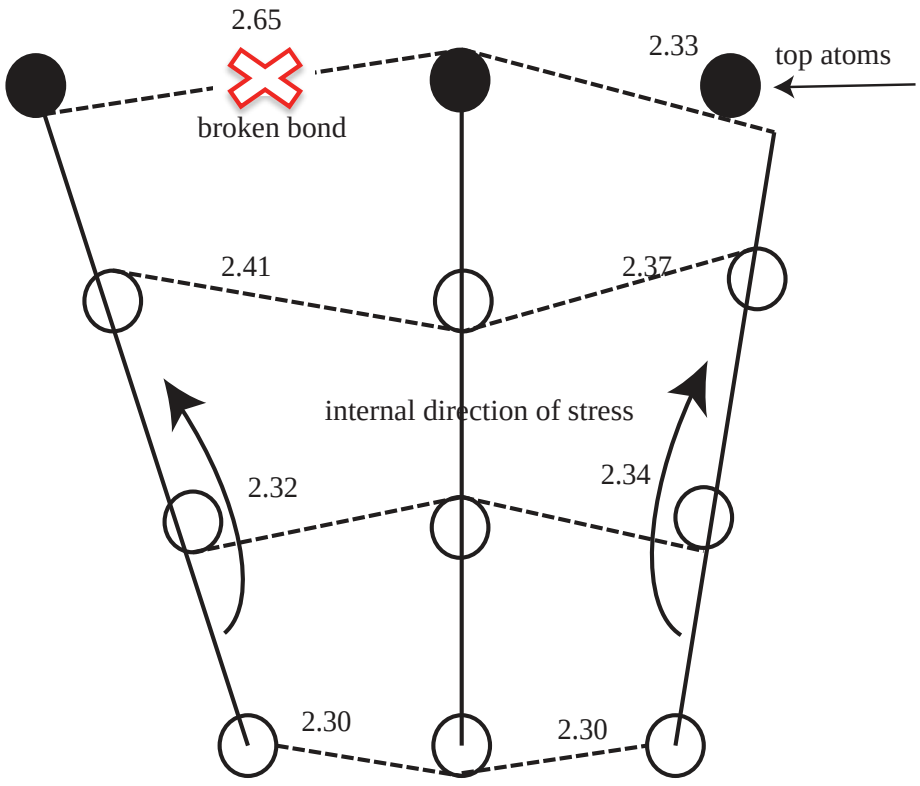

Figure 4.8: Schematic diagram showing the gradual bond stretching directions leading to the bond break at the heterojunction and indicated values are in Å. Full and open circles represent Si atoms at topmost layer and layers below. Hatched lines represent atomic bonds and full lines to aid eyes.

strains. When materials are distorted along these directions, internal displacements of atoms occur [3, 107] as a consequence of elongation or contraction.

By applying the above mechanism, we find that starting roughly from the fourth atomic layer of Si(110) side, the atomic bonds gradually elongate by reducing the crystal symmetry until the strain reaches the topmost layer at the heterojunction and then snaps as shown in Figure 4.8, that is, one of the topmost nearest neighbor atoms sp^3 bond completely breaks. The bending of the Si(110) surface affects the 3C-SiC(111) surface making the interface not flat. The distance between the atoms with broken bonds are tabulated in Table 4.3 below with the corresponding coordination numbers. The broken bond distances are believed to compensate for stress-release at the interface. The resulting effect is that,

Table 4.3: Nearest neighbor atoms with broken bond distance and the atoms coordination number.

	Si-C interface	Si-Si interface
Type I [Å]	3.43	2.65
Type II [Å]	3.57	2.78
Coordination number	(5, 4 and 3)-fold	3-fold

for Si-C interface, one of the broken Si atom bond from the 3C-SiC(111) surface becomes 5-fold coordinated whiles two Si-atoms from the Si(110) surface becoming (those with broken bonds) 4-fold and 3-fold coordinated respectively. The orientations of the atomic bonds with these coordination numbers are different in both type I and type II geometries. We note that, these orientations are not mirror symmetric. In the same way for Si-Si interface, we find that the atoms with the broken bonds remain 3-fold coordinated. The consequence effect is that bond breaking creates a hole which is a defect and perpendicular to the interface. As a fair comparison, Giancarlo *et al*, investigated 3C-SiC(100)/Si(100) interface by means of combined classical and *ab initio* molecular dynamics and concluded that misfit dislocation network pinned at the interface is the efficient mechanism for strain relief [106].

As a rough comparison let us consider the following examples; for Ge/Si(100) interface, Fujimoto *et al* proposed five-and seven-membered Ge rings of 90°-dislocation core [41] or pairing distortions around a vacancy [101] as the main mechanisms to account for the strain relaxed Ge film grown on Si substrate. Similarly for InAs/GaAs(110) interface, Oyama *et al* concluded that core confined at the interface is five-fold coordinated In atoms and confirmed by Choudhury and collaborators as the mechanism of epitaxial growth of InAs on GaAs(110). This further suggests that defect at the interface plays a vital role in strain relief. Based on the previous stress relief examples of interfaces as against the present 3C-SiC(111) on Si(110) surface, we propose that atomic bond breaking create a defect at the interface which is a key mechanism of the relaxation and reconstruction. We confirm that the interface bonds are still traditional sp^3 but are distorted and oriented in such a way that the supercell is energetically stable due to the new atomic re-arrangements.

4.4 Interface energy

To discuss the energetics of the interface, we introduce the interface energy as a quantity to compare the stability of the interface system under equal footing due to the difference in the bulk terminations. By definition, the interface energy $\mathbf{I}_E$ is the energy cost to form the interface system from the respective 3C-SiC and Si crystal phases. As we already know, there are two possible interface systems and therefore the respective interface energies are defined as follows:

1. For Si-Si interface, the 3C-SiC($\bar{1}\bar{1}\bar{1}$) is the terminated surface which is fixed. The interface energy calculated is defined as:

$$\mathbf{I}_E = \mathbf{E}_{opt} - \mu_{Si(bulk)}\mathbf{N}_{Si} - \mu_C\mathbf{N}_C - \{\mu_{H_{Si}}\mathbf{N}_{H_{Si}} + \mu_{H_C}\mathbf{N}_{H_C}\}. \tag{4.1}$$

2. For Si-C interface, the 3C-SiC(111) is the terminated surface which is equally fixed. The interface energy is defined as:

$$\mathbf{I}_E = \mathbf{E}_{opt} - \mu_{Si(bulk)}\mathbf{N}_{Si} - \mu_C\mathbf{N}_C - \mu_{H_{Si}}\mathbf{N}_{H_{Si}}. \tag{4.2}$$

where $\mathbf{E}_{opt}$, is the total energy of the interface system, $\mu_{Si(bulk)}$, μ_C, μ_{H_C}, $\mu_{H_{Si}}$, $\mathbf{N}_{Si}$, $\mathbf{N}_C$, $\mathbf{N}_{H_C}$,$\mathbf{N}_{H_{Si}}$ are the chemical potentials of Si, C, H and corresponding number of atoms in the supercell. The hydrogen chemical potentials are prepared depending on the environment to be used, that is either fixed to Si or C accordingly. These parameters are discussed in detail in section 3.1.1.

The interface energy per interface area of the supercell is given by:

$$\gamma = \frac{\mathbf{I}_E}{A}, \tag{4.3}$$

where A is the area of the interface system.

The true carbon chemical potential μ_C in the interface structure is determined from the equation:

$$\mu_C = \mu_{SiC(bulk)} - \mu_{Si(bulk)}. \tag{4.4}$$

Table 4.4: Summary of the evaluated 8L/8L 3C-SiC(111) on Si(110) interface energy per supercell in eV and also per interface area γ.

Type :	type I		type II	
	Si- Si	Si- C	Si-Si	Si- C
$\mathbf{I}_E$ [eV/cell]	9.571	10.406	9.890	10.840
γ [eV/Å^2]	0.117	0.127	0.121	0.133

Again, notice that equations (4.1) and (4.2) differ by the carbon-passivated surface. The interface energy must take into consideration this hydrogen chemical potential attached to the C for equal treatment. Using the above equations, we evaluate the interface energy of the interface system. The interface energy per area are summarized in Table 4.4 for 8L/8L 3C-SiC(111) on Si(110) surface.

The calculated interface energies reveal that the Si-Si interface is energetically favorable compared with the Si-C with the interface energies being 0.117eV/Å^2 and 0.127eV/Å^2 per supercell accordingly irrespective of the bistability. The interface energies are sensitive to the overall hydrogen chemical potential and the calculation conditions.

We discussed in the last paragraph of section 4.2 that, the origin of the stability of Si-Si interface can be understood that, the bonding character at the interface still remains sp^3 as shown in Figure 4.7 and that the bond strength of Si-Si bond is small compared with Si-C bond. As a comparison of the bond strengths between Si-Si and Si-C bonds, consider the elastic coefficients, zone-center transverse-optical phonon-frequency all are related to angular restoring forces. It is known that the phonon frequency and elastic coefficients of 3C-SiC are large compared with Si at any arbitrary crystallographic direction [94, 102–105]. As a consequence during the interface relaxation, angular forces due to bent tetrahedral bonds of Si-C experience large strain than Si-Si bonds. Hence this can be the potential reason why the Si-Si interface is energetically stabler compared with the Si-C interface.

4.5 Band dispersions of the interfaces

The electronic properties of the interface systems are determined by the interface area atomic structures. In particular, the presence of two effective dangling bonds which originate from the 3C-SiC(111) surface side in the ideal interface are partially occupied. It is

Table 4.5: Summary of relaxed 8L/8L 3C-SiC(111) on Si(110) surface energy band gap values.

8L/8L	Si-C interface [$\mathbf{E}_{gap}$]	Si-Si interface [$\mathbf{E}_{gap}$]
Type I [eV]	0.53	0.33
Type II [eV]	0.54	0.07

expected that, these partially occupied DBs will influence the interface states. As shown in Figure 4.9, the band dispersions of the ideal and relaxed 4L/4L 3C-SiC(111) on Si(110) prototype interface type I are along the high symmetry points ΓX-XK-KX'-X'Γ directions of the rectangular brillouin zone. With the Si-C interface, the two effective dangling bonds are localized on carbon D_C as depicted in Figure 4.9(a) compared with Si-Si interface which are localized on silicon D_{Si} as indicated in Figure 4.9(c).

After the atomic structure optimization, we find that the two effective DBs which are partially occupied in the ideal interface are now unoccupied. But this is not a simple DB disappearance; instead a consequence of an interesting interface relaxation. The resulting effect is the opening of band gaps as shown in Figures 4.9[(b) and (d)] accordingly with band gaps values of 0.69 and 0.31 eV. It should be noted that LDA do not give accurate values of the band gaps, however, it prescribes accurately the topology of bands and can also predict the nature of electronic structure property of materials.

For fair comparison of 4L/4L 3C-SiC(111) on Si(110), we calculate the electronic dispersions of the relaxed 8L/8L 3C-SiC(111) on Si(110) for both type I and II interface systems as indicated in Figure 4.10, since 4L/4L interface atomic layers are not converged to discuss accurate interface electronic properties. We find that the electronic structures of all the four 8L/8L relaxed interfaces systems have indirect band gaps just like the relaxed 4L/4L interface system. The corresponding energy band gaps are summarized in Table 4.5 with Si-Si interface having the least energy band gap value in the two types of interface geometries.

The occupied valence band maximum and unoccupied conduction band minimum are located at the high symmetry K and Γ points for type I interface structures and the same symmetry points are observed for Si-C interface of type II. As for Si-Si interface of type II, they are located at X and X' respectively. The character of the valence band maximum and conduction band minimum are mixed overlapped π- and π^*-like in nature. Careful observation shows that, the relaxed Si-C interface band structures of either 4L/4L or 8L/8L

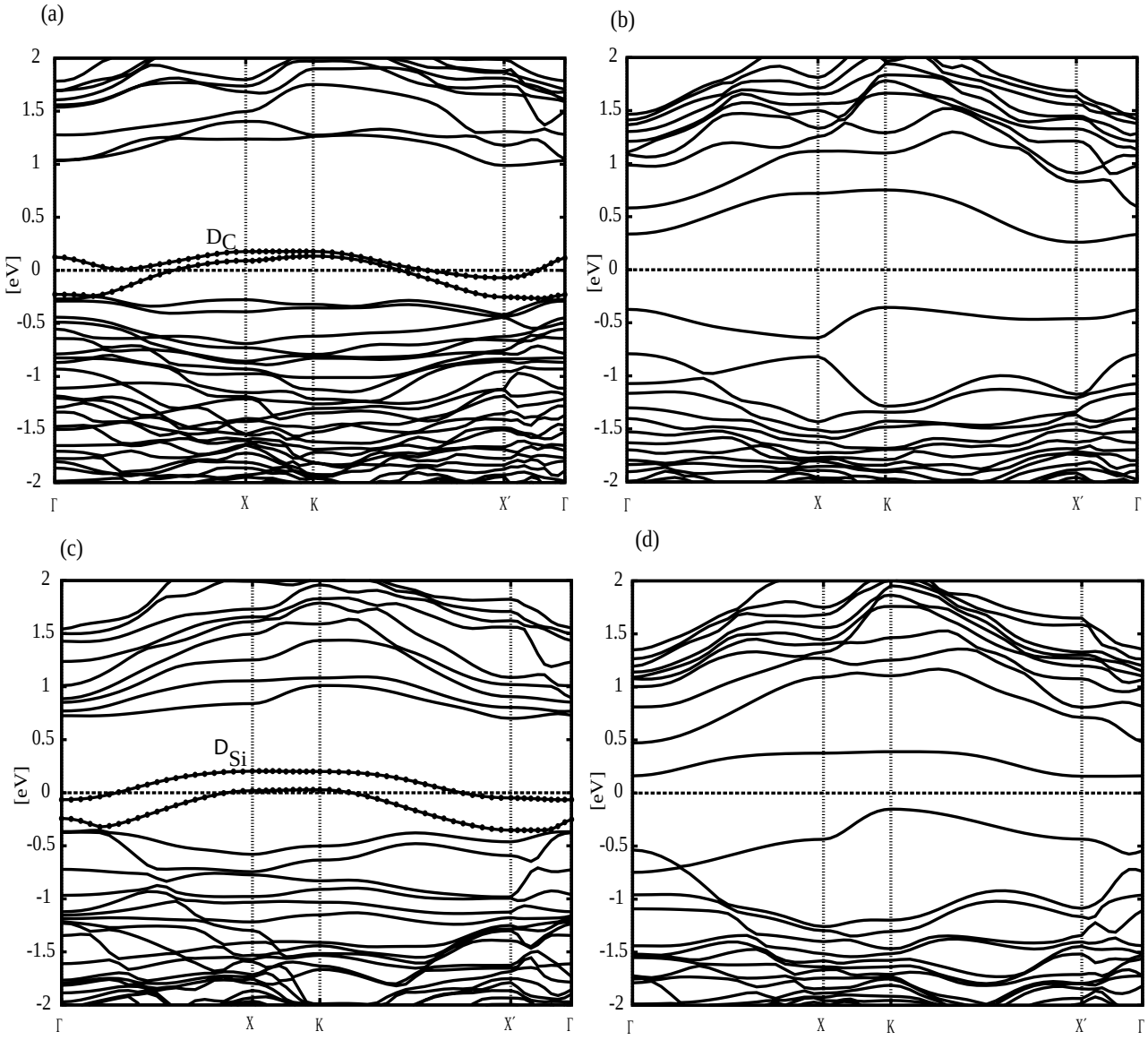

Figure 4.9: Type I interface of 4L/4L 3C-SiC(111) on Si(110) band dispersion diagrams [(a) Ideal (b) relaxed] Si-C interface and [(c) Ideal and (d) relaxed] Si-Si interface.

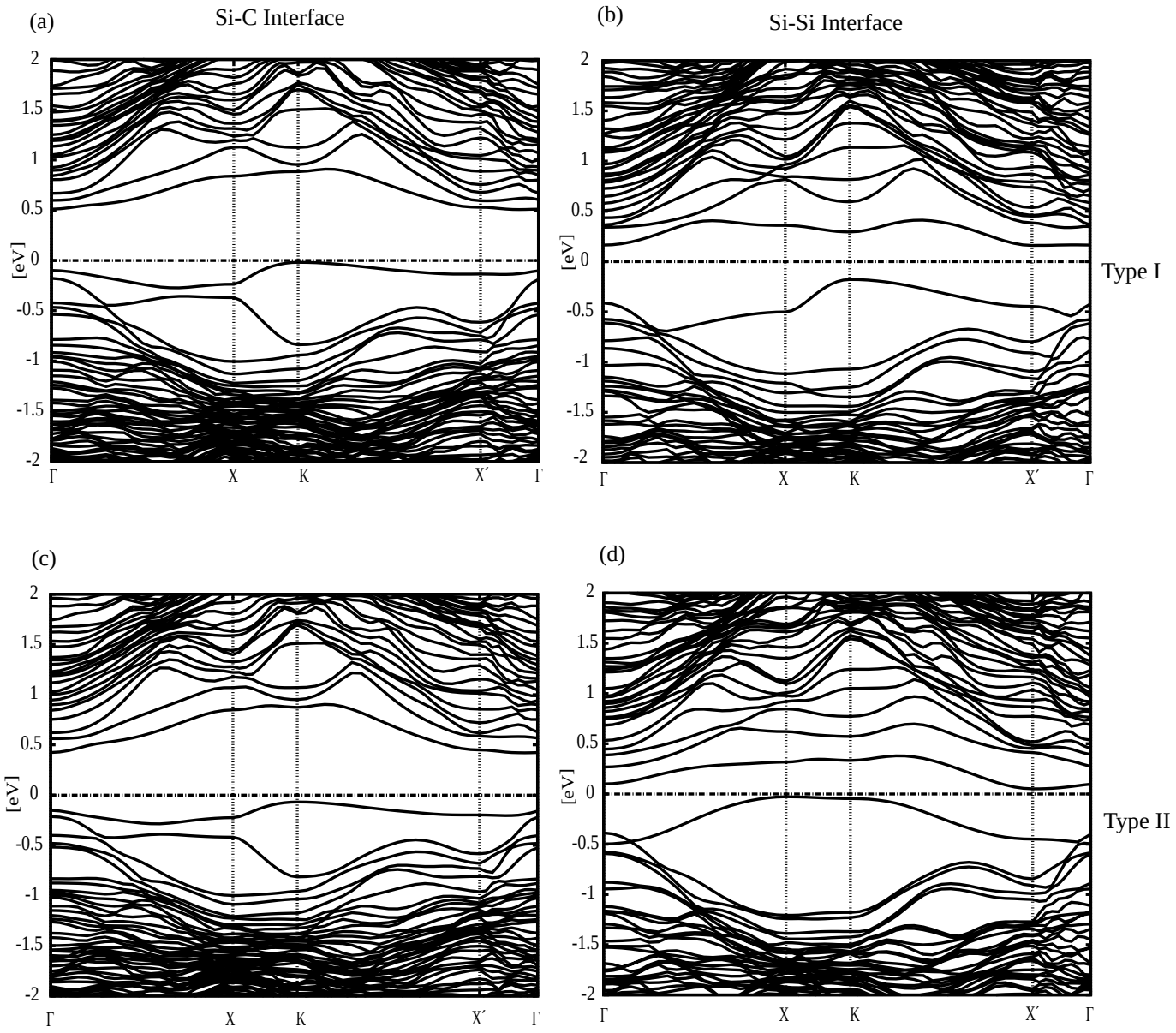

Figure 4.10: Relaxed 8L/8L 3C-SiC(111) on Si(110) band dispersion diagrams of [(a) Si-C and (b) Si-Si] of type I and [(c) Si-C and (d) Si-Si] of type II interfaces respectively.

are qualitatively similar in appearance in contrast with the Si-Si interface. An important observation we find is that the valence band tops of all the band structures considered show strong dispersion character suggesting that the interface states can be arranged periodically and perpendicularly at the interface.

The occupied floating bond states which are extended around the defect hole may give an explanation to the energetics of the interface system. The origin of the interface states comes from the broken adjacent Si-Si nearest neighbor bond discussed in section 4.3 and the two effective DBs coming from the 3C-Si(111). These DBs vanish after the geometry optimization leading to interface atomic rebonding. It is known that, bond breaking costs energy, but we now find that this is not true always from the present calculation. The model system considered indicates that Si(110) surface breaking one of its surface atom bond is the key mechanism of interface energy minimization. Since there is energy gain due to DBs rebonding result in the formation of extended floating bonds at the interface which create a defect hole. The mixture of extended floating bonds states around the defect hole creates partial induced polarization due to the electronegativity difference between the two crystals. By this complicated rebonding arrangements at the interface, the overall electronic property of the interfaces systems remains semiconducting. In Figure 4.11, we illustrate the schematic representation of the rebonding mechanism which leads to the disappearance of the two effective DBs coming from the 3C-SiC(111) surface side, though several interface atoms are involved in a complicated way especially the broken Si-Si nearest neighbor bond atoms.

To support this understanding, we located the doubly occupied interface floating bonds states around a defect hole which are mixed p_z-like character wavefunction near the valence band region as shown in Figures 4.12 for both type I and II interfaces. These extended floating interface states show bonding character with corresponding relative energy position indicated in Table 4.6. The type I occupied interface states have lower energy than the type II interface. In the Si-C interface states, the wavefunction extends more than the Si-Si interface. Figure 4.13[(a) and (b)] indicates the 90° rotation of Figures 4.12[(a) Si-C and (c) Si-Si] interface with decreased isovalue to show the extended floating bonds states around the defect hole.

Similarly we also located the unoccupied bonding σ^* character wavefunction of the interface floating bond states which are mixed p_z-like character wavefunction in the con-

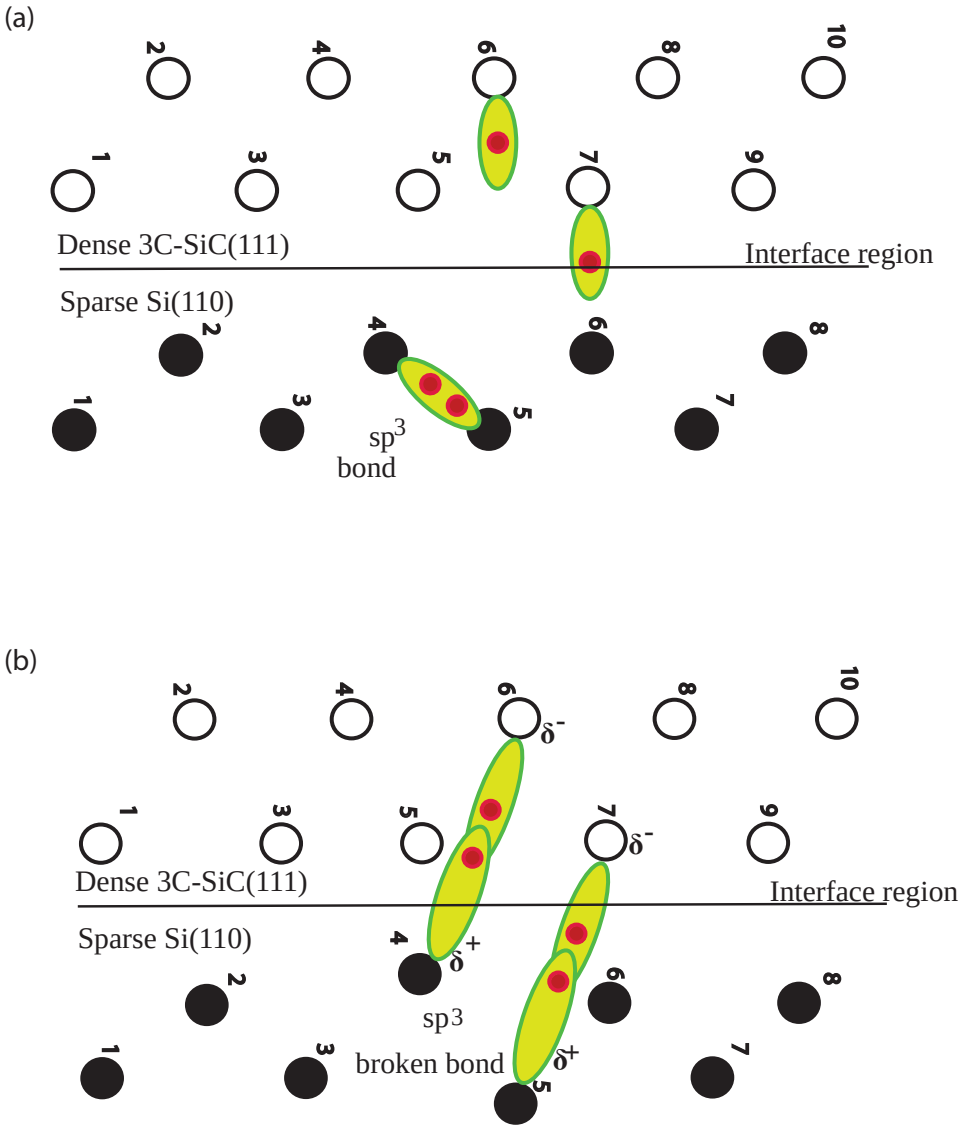

Figure 4.11: The electronic mechanism of charge redistribution at the 3C-SiC(111) on Si(110) surface showing (a) one of the expanded ideal sp^3 bonds of the topmost Si(110) surface atoms and the effective partially occupied two dangling bonds coming from 3C-SiC(111) side. (b) the relaxed broken sp^3 bond of Si(110) forming the extended rebonding with 3C-SiC(111) which are doubly occupied leading to the disappearance of dangling bonds at 3C-SiC(111) side in a complicated fashion. The empty circles represent atoms from 3C-SiC(111) side and full circle represent the Si(110) interface atoms. The labels show the positions of the interface atoms and red dot represent an electron.

Table 4.6: Summary of energy position of floating bond states which are occupied and originates mainly from the varnished DBs due to new rebonding arrangements. The energy position are relative to the valence band maximum and the corresponding wavefunctions are indicated in Figure 4.12.

Doubly occupied interface states	Si-C interface	Si-Si interface
Type I [eV]	- 0.5193	-0.6102
Type II [eV]	-0.4485	-0.4698

duction band as shown in Figures 4.14. The corresponding relative energy position are summarized in Table 4.7. The energy positions are calculated relative to the valence band top and conduction band minimum respectively for type I and type II at the gamma point.

Table 4.7: Summary of energy position of floating bond states which are unoccupied and located in the conduction band originates from the varnished DBs due to new atomic rebonding arrangements and show bonding character. The energy positions are relative to the conduction band minimum and the corresponding wavefunctions are indicated in Figure 4.14.

Unoccupied interface states	Si-C interface	Si-Si interface
Type I [eV]	0.3847	0.5218
Type II [eV]	0.0000	0.0000

4.6 Pre-relaxed Interface

In this section, we present the results of a pre-relaxed interface calculation. This is intended to collaborate with the interface relaxation pattern. It should be emphasised that, there are several possibilities of $n \times m$ 3C-SiC(111) on $n^{'} \times m^{'}$ Si(110) surfaces reconstructions. Therefore, this can be out of scope as a result we concentrate only on the reconstruction of the present system.

In Chapter 3, we discussed the Si-terminated, C-terminated and Si(110) (1×1) surfaces relaxation pattern and electronic structures of two atoms on lateral surface. To confirm the reliability of the interface calculations, we separately relax the Si-terminated, C-terminated and Si(110) slabs following the recipe of computations outlined in section 2.5 Figure 2.4 (a). The only significant difference is the size of the supercell, which is similar to the one used for the interface geometries as in Figure 2.5 (a). The same number of **k** points and cutoff energy are employed. The initial geometries are those which yield the relaxed stable geometry of type I interface system. We have manually removed those

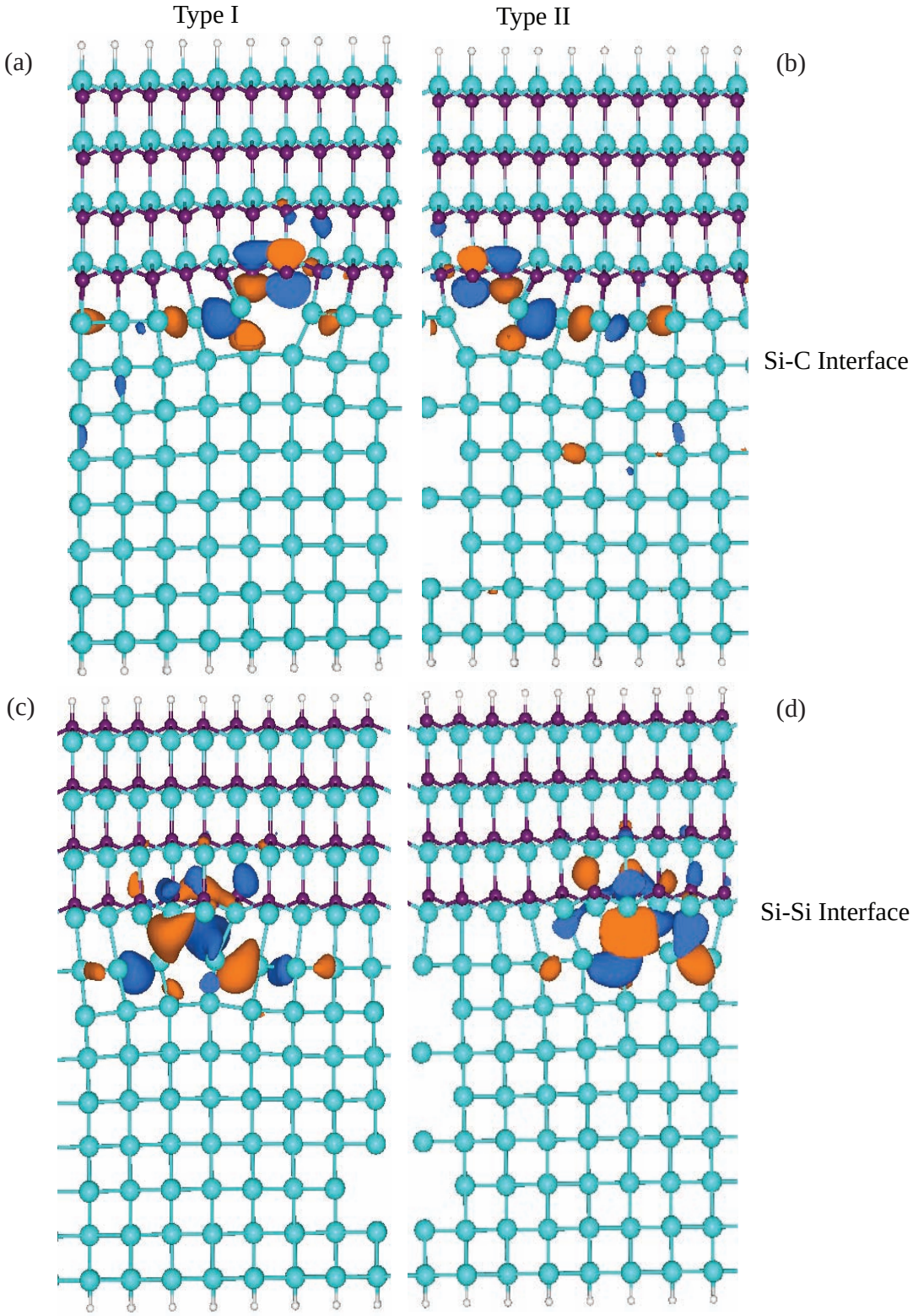

Figure 4.12: The relaxed 8L/8L 3C-SiC(111) on Si(110) surface geometries showing isosurface at Γ-point of Kohn-Sham wavefunctions which have large amplitudes and appear to localize mainly around the defect hole and mixed with side-bonds coming from Si(110). These floating states are doubly occupied and originates from the varnished DBs due to new rebonding arrangements. The mixed p_z-like character is obvious. [(a) Si-C and (c) Si-Si] of type I and [(b) Si-C and (d) Si-Si] of type II interfaces respectively with the isovalue $0.03a_0^{-3}$. The energy positions of these states are indicated in Table 4.6.

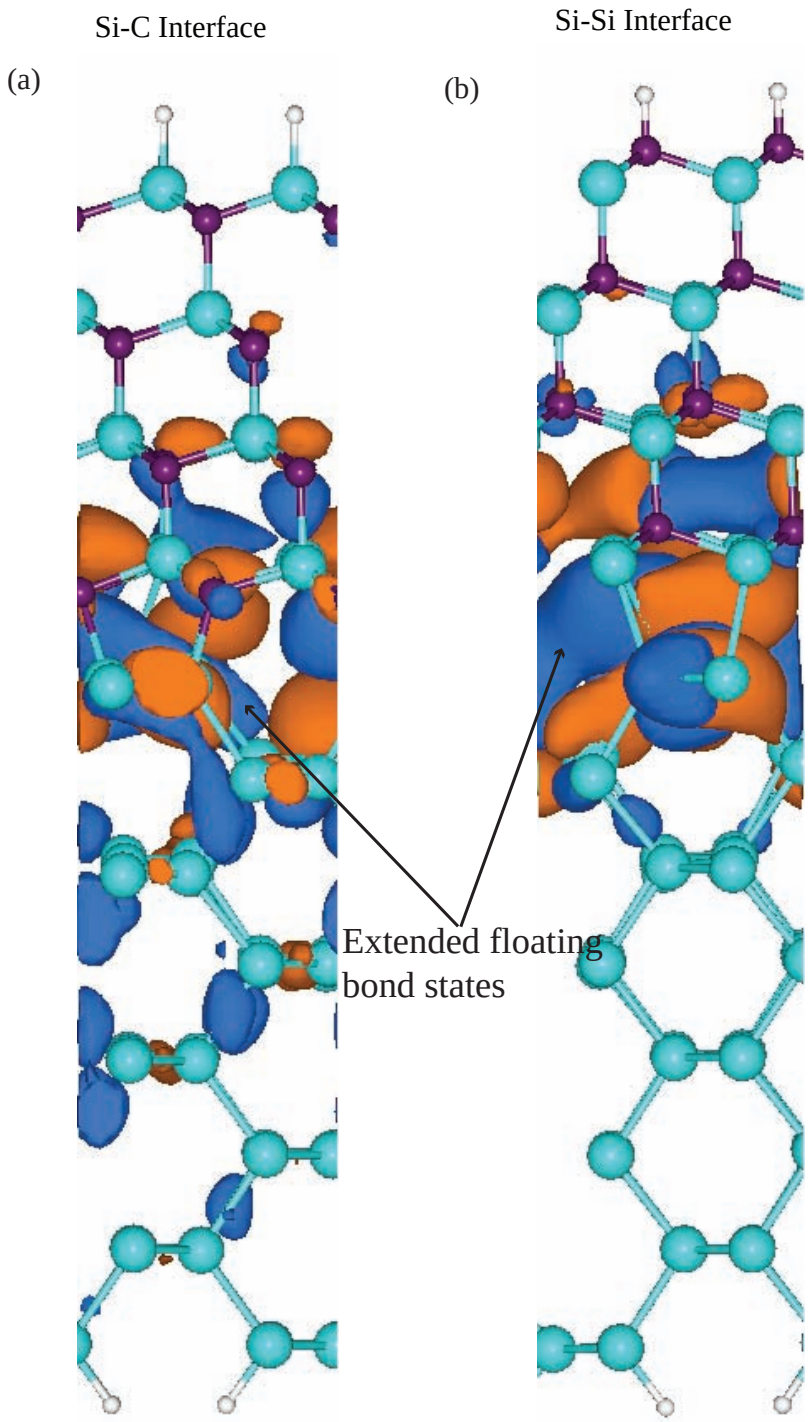

Figure 4.13: The 90° rotated side view of relaxed 8L/8L 3C-SiC(111) on Si(110) surface geometries and isosurface at Γ-point of Kohn-Sham wavefunctions which have large amplitudes and showing the extended doubly occupied floating bonds states around the defect hole (a) Si-C and (b) Si-Si interfaces respectively with reduced isovalue of $0.018 a_0^{-3}$.

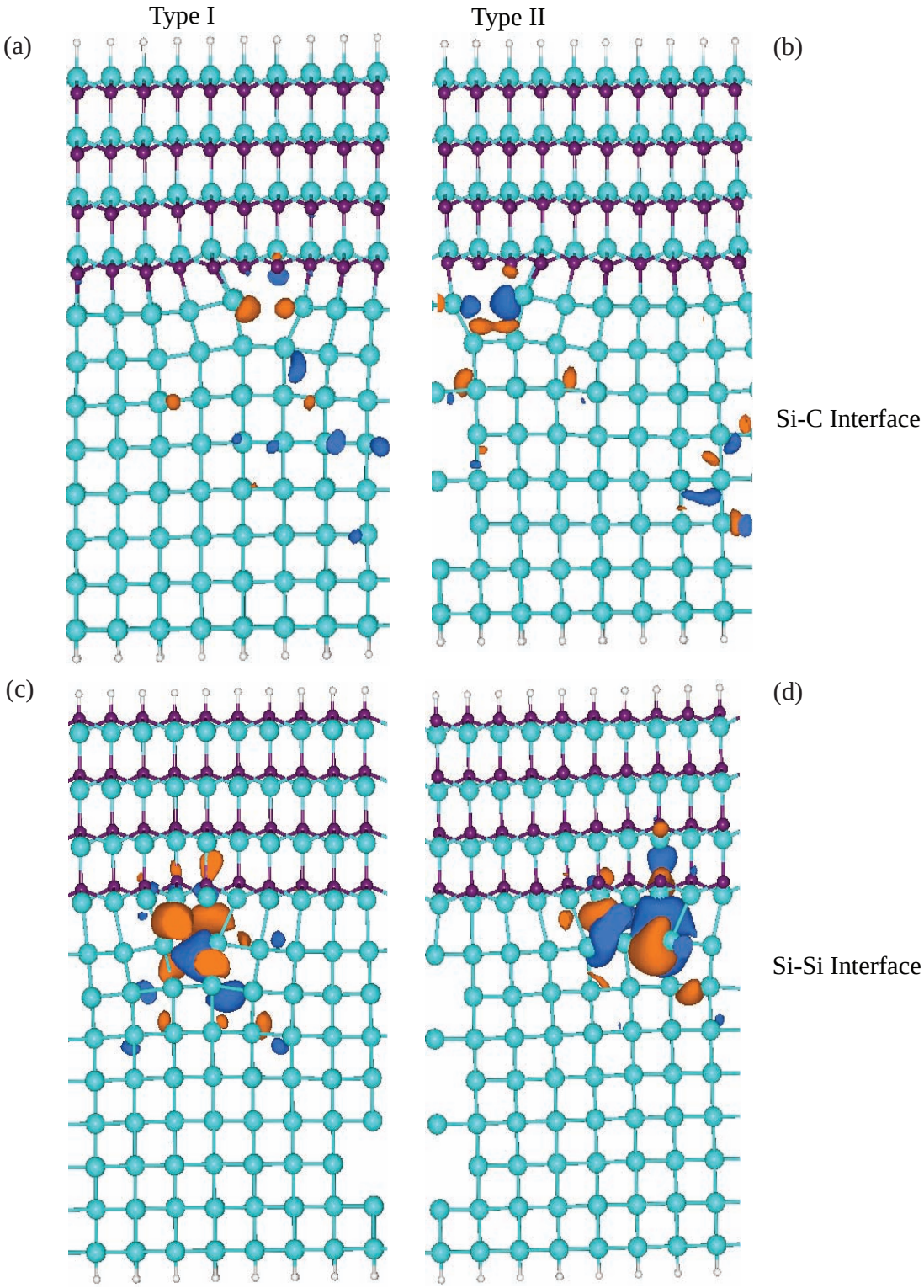

Figure 4.14: The relaxed 8L/8L 3C-SiC(111) on Si(110) surface geometries showing iso-surface at Γ-point of Kohn-Sham wavefunctions which have large amplitudes and appear to localize around the defect hole. These states are completely empty, originate mainly from the floating bond states and show σ^*-bonding character. [(a) Si-C and (c) Si-Si] of type I and [(b) Si-C and (d) Si-Si] of type II interfaces respectively with the isovalue of $0.03a_0^{-3}$. The corresponding energy positions of these states are indicated in Table 4.7.

atoms which do not apply appropriately and carried out the atomic structure optimization. Figure 4.15[(a), (b) and (c)] shows the relaxed Si-terminated, C-terminated and Si(110) surfaces respectively. Clearly, the individual slabs do not show any sign of undulations, however, a close look at Figure 4.17 (b) which is Si-terminated surface indicates slight vertical and lateral atomic displacements at the topmost bilayer consistent with the case of primitive lateral surface relaxation.

Afterwards, we match the relaxed slabs together to constitute the interface geometry and perform again atomic structure optimization. As already indicated in Figure 4.15 (d) and (e), the final relaxed interface geometries are marked by undulations when 4-atomic layers near the interface are viewed. The breaking of Si(110) surface one nearest neighbor atomic bond is obvious and relates to the lattice mismatch as well as dense and sparse nature of the two surfaces. Structurally, these pre-relaxed geometries are very similar to those indicated in Figure 4.4 suggesting that, irrespective of the manner of relaxation, relaxation patterns are the same. We find that the energy difference between these interface geometries and those of type I are 0.9 meV for Si-Si interface and 0.45 eV for Si-C interface. Again, the Si-Si interface is energetically stabler compared with Si-C interface. Also the electronic structure calculations show semiconducting behavior consistent with the previous results.

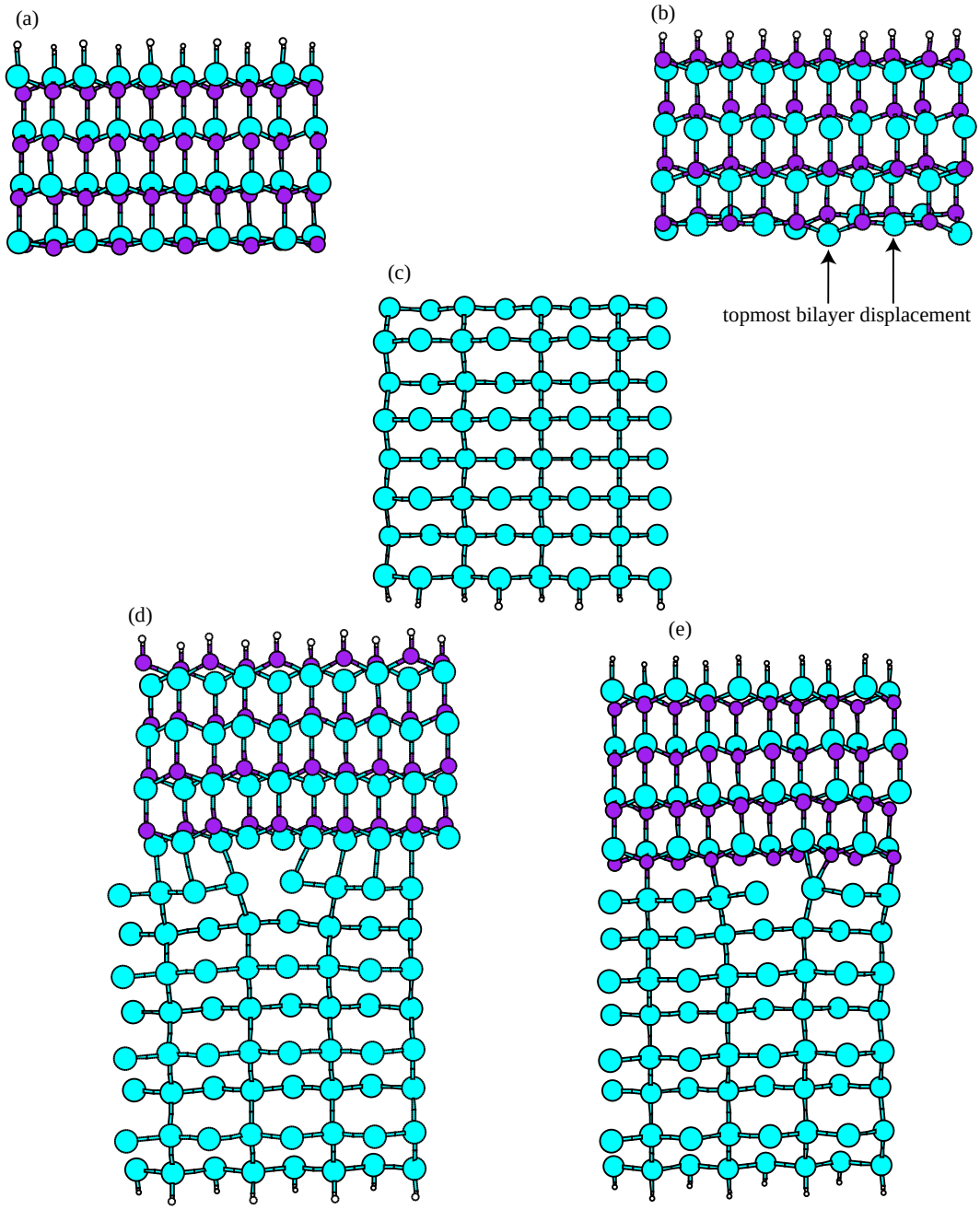

Figure 4.15: pre-relaxed 8-layers of : (a) 3C-SiC($\bar{1}\bar{1}\bar{1}$) (b) 3C-SiC(111) (c) Si(110) slabs. The interface geometries after silicon carbide slabs have been put on Si(110) surface to form 3C-SiC(111) on Si(110) interface slabe (d) Si-Si and (e) (Si-C interface.

First-principle study of atomic and electronic structures of 3C-SiC(111)/Si(110) interfaces

Eric K. K. ABAVARE
(Doctoral Program in Frontier Science)

Submitted to the Graduate School of
Pure and Applied Sciences
in Partial Fulfillment of the Requirements
for the Degree of Doctor of Philosophy in
Science

at the
University of Tsukuba

Chapter 5

Concluding Remarks

In conclusion, we perform a very reliable total-enegy electronic structure calculation based on real space density functional theory that provides sound theoretical foundation to discuss and clarify the interface atomic and electronic structures, interface relaxation mechanism, interface energetics and interface electronic structure properties of 3C-Si(111) on Si(110) surfaces.

To augment the existing knowledge of surface energies, we study the surface energies of Si(110) 1×1, 3C-SiC(111) and 3C-SiC($\bar{1}\bar{1}\bar{1}$) 1×1 surfaces. The surface energy of Si(110) is found to be 1.334 eV/atom (2100 mJm^{-2}) for unrelaxed and 1.111 eV/atom (1745 mJm^{-2}) for relaxed surfaces. We find that these values are in close agreement with other first principle calculations, however when compared with experiments these calculated values are overestimated by about 22%.

Similarly, we calculate for the first time relaxed and unrelaxed surface energies of C- and Si-terminated surfaces of 3C-SiC based on first principles calculations. In the relaxed C- and Si-terminated surfaces, the calculated surface energy values are 1.272 (2720) and 0.910 eV/atom (1830 mJm^{-2}) whereas for the unrelaxed surface, the calculated surface energies are 1.438 (3065) and 0.951 eV/atom (2856 mJm^{-2}), respectively. For the purpose of comparing the calculated results with the experiment, knowledge for the experimental surface energy values of C- and Si-terminated surfaces are crucial. However, the only known report on the experimental surface energy is that of the Si-terminated surface and the value is 2180 mJm^{-2}. If we compare this experimental value with the calculated relaxed surface energy, we find that Si-terminated surface energy is underestimated

by -16%. Arguably, Si(110) surface is not a polar surface compared with Si-terminated surface of 3C-SiC, therefore the exact reason why there is significant difference in the calculated surface energy values compared with the experimental values is not clearly understood. With regards to the dangling bond positions located on Si- and C- terminated surfaces, we find that the relative energy position of Si dangling bond D_{Si} is located 1.13 eV higher than the C dangling bond D_C, making it different from that of the $\alpha - 6H(0001)$ terminated surface as reported by Pollman and collaborators as 1.5eV [95]. We conclude that, despite the fact that the surface symmetry of 3C-SiC and $\alpha - 6H(0001)$ terminated surfaces are both hexagonal, they are electronically not the same because their dangling bond positions are different.

In order to investigate the stability of 3C-SiC(111) on Si(110) surface and the corresponding electronic structure properties, it is necessary to obtain the minimum interface atomic layers of each of the two semiconductor materials that is sufficient to discuss interface system. To obtain the necessary atomic layers of the interface structure, we initially use 4-atomic layers of each material and examine several interface geometries and then perform atomic structure calculations for the interface system until we find the most stable interface geometry.

Starting from the initial atomic positions of this most stable interface geometry, we systematically increase the interface atomic layers in the supercell and optimize each geometry until the calculated mean atom displacement from the ideal position per atomic layer is converged. By this procedure, we find that 8-atomic layers of 3C-SiC(111) on Si(110) (8L/8L) is considered converged interface layers and sufficient to discuss realistic interface systems. We find that there are only two possible interface heterojunctions, if silicon faces meet, we have Si-Si interface and if silicon and carbon faces meet, we have Si-C interface (are considered in this thesis).

We explore several candidate interface geometries and reach two distinctive types. We call them type I and type II after the atomic geometry optimizations. We find that these structures are bistable which implies there are four different geometries in total. After the geometry optimization, the most striking observable effect which results from the reconstruction and relaxation near the interface is marked undulations as an intrinsic property. The undulation effect is characteristically seen always within 4-atomic layers at the Si(110) surface side indicating that the interface is not very flat at the atomic level. We

find that the interface relaxation is associated with the breaking of exactly one Si(110) surface atom nearest neighbor bond in the supercell. The exactly one Si(110) surface atom nearest neighbor bond breaking in the supercell can be considered as a key mechanism to release the interface stress between Si(110) and 3C-SiC(111) interface system which might relate to the lattice mismatch. The combined effects of the observed undulation and bond breaking near the interface are likely to be the mechanism of the interface relaxation.

To discuss the energetics of the interface, we introduce the interface energy as a quantity to compare the stability of interface systems. The calculation reveals that the Si-Si interface structure is energetically favorable compared with the Si-C interface structure. The reason for the Si-Si interface energetic stability is that, after atomic structure relaxation the Si-Si interface connecting bonds become more flexible and can easily bend compared with the Si-C interface connecting bonds which are not flexible and difficult to bend. This is because the Si-Si interface bonds act like the bulk Si and the Si-C interface acts like 3C-SiC bulk. The 3C-SiC bonds are not flexible compared with the Si bonds. As a result the angular forces, due to bent tetrahedral bonds of Si-C interface, experience greater strain than Si-Si interface.

We find that, the interface electronic structure calculation predicts semiconducting behavior regardless of the type of interface system. The band gap of the Si-C interface is comparatively larger than Si-Si interface system. The mechanism of the semiconducting behavior of the interface system is attributed to the bond breaking of Si(110) surface one nearest neighbor atom bond. This break causes the disappearance of the two effective dangling bonds coming from 3C-SiC(111) surface by forming new extended bonds which then creates a defect hole perpendicular to the interface. By this process, all partially occupied dangling bonds disappear from the interface area leaving the interface system to remain semiconducting. Finally, to corroborate the results, we prepare pre-relaxed slabs of 8-atomic layers of each 3C-SiC(111) and Si(110) surfaces accordingly. We then match the two slabs to form the interface and relaxed it. The relaxed atomic structures show that Si-Si interface is still stabler than Si-C interface with energy difference 0.9 meV and 0.45 eV respectively, compared with the previous results of type I interface structures. In this calculation, the observation of undulation again near the interface re-enforces the assertion that, 3C-SiC(111) surface atoms are dense compared with the sparse flexible Si(110)

surface which tend to warp around the 3C-SiC.

Bibliography

[1] A. Franciosi, C. G. Van de Walle, Surf. Sci. Reports **25**, 1 (1996).

[2] C. G. Osbourn, J. Appl. Phys. **53**, 1586 (1982).

[3] C. G. Van de Walle, R. M. Martin, Phys. Rev. B **34**, 5621 (1986).

[4] D. J Eaglesham and M. Cerullo Phys. Rev. Lett. **64**, 1943 (1990).

[5] J. J. Berzelius, Ann. Phys. Lpz. **1**, 169 (1824).

[6] A. R. Verma and P. Krishna, *Polymorphism and Polytipism in Crystals (Wiley, New York, 1966)*.

[7] L. Patrick, Phys. Rev. **127**, 1878 (1962).

[8] L. U. Ogbuji, Phys. stat. sol b (**72**), 455 (1982).

[9] W. E. Nelson, F. A. Halden and A. Rosengreen, Appl. Phys. **37**, 333 (1966).

[10] M. Bhatnagar and J. Baliga, IEEE Trans Electron Devices **40**, 645 (1993).

[11] E. Pettenpaul, W. v. Münch and G. Ziegler, *Silicon carbid devices* Inst. Phys. Conf. Ser. **53**, 21 (1980).

[12] D. K. Ferry, Phys. Rev. B **12**, 2361 (1975).

[13] F. Yun, S. Chevtchenko, Y-Y. Moon, H. Morkoc, T. J. Fawcett and J. T. Wolan, Appl. Phys. Lett. **87**, 073507 (2005).

[14] D. M. Jackson and P.W. Howards. Trans. Met. Soc. AIME **223**, 488 (1965).

[15] K. S. Novoselov, D. Jiang, F. Schedin, T. J. Booth, V. V. Khotkevich, S. V. Morozov and A. K. Geim, Proc. Natl Acad. Sci. USA **102**, 10451 (2005), K. S. Novoselov, A.

K. Geim, S.V. Morozov, M. I. Katsnelson, I. V. Grigoriev, S. V. Dubonos and A. A. Firsov, *Nature Letters* **438**, 197 (2005), A. K. Geim, A. H. MacDonald, Phys. Today, 35 (2007).

[16] A. K. Geim and K. S. Novoselov, *Nature materials* Vol. **6**, 183 (2007).

[17] G. Brumfiel, *Nature***458**, 390 (2009).

[18] S. Roy, C. Jacob, and S. Basu, Sensors Actuators. B **94**, 17 (2003).

[19] Z. C. Feng, Microelecton. Eng. **83**, 164 (2006).

[20] S. Nishino, H. Suhara, H. Ono, H. Matsunami, Appl. Phys. Lett. **61**, 15 (1987).

[21] A. Addamiano and J. A. Sprague, Appl. Phys. Lett. **44**, 5 (1984).

[22] C. S. Chang, N. J Zheng, and I. S. T. Tsong, Y. C. Wang and R. F. Davis, J. Vac. Sci. Technol. B **9**, 2 (1991).

[23] S. Nishino, J. A. Powell and H. A. Will, Appl. Phys. Lett. **42**, 5 (1983).

[24] K. Yasui, J. Eto, Y. Narita, M. Takata and T. Akahane, Jpn. J. Appl. Phys. **44**, 1361 (2005).

[25] H. Nagasawa, T. Kawahara and K. Yagi, Mater. Sci, Forum **389-393**, 319 (2002).

[26] H. Nakazawa and M. Suemetsu, J. Appl. Phys. **93**, 5282 (2003).

[27] Z. C. Feng, W. J. Choyke, J. A. Powell, J. Appl. Phys. **64**, 12 (1988).

[28] T. Nishiguchi, Y. Mukai, S. Ohshima and S. Nishino, Phys. stat. sol c **0** No.7, 2585 (2003).

[29] K. Shibahara, S. Nishino and H. Matsunami, Appl. Phys. Lett. **50**, 1888 (1987)

[30] K. Shibahara, S. Nishino and H. Matsunami, J. Cryst. Growth **78**, 538 (1986).

[31] Y. Ishida, T. Takahashi, H. Okumura, T. Sekigawa and S. Yoshida, Jpn. J. Appl. Phys. Part I **38**, 3470 (1999).

[32] H. Matsunami, S. Nishino and H. Ono, IEEE Trans. Electron Devices **28**, 1235 (1981).

[33] S. Veprek, T. Kustmann, D. Volm and B. K. Meyer, J. Vac. Sci. Technol. A **15** 10 (1997).

[34] T. Nishiguch, M. Nakamura, K. Nishio, T. Isshiki, and S. Nishino, Appl. Phys. Lett. **84**, 3082 (2004).

[35] H. Mukaida, H. Okumura, J. H. Lee, H. Daimon, E. Sakuma, S. Misawa, K. Endo and S. Yoshida, J. Appl. Phys. **62** 254 (1987).

[36] A. Severino, G. D'Arrigo, C. Bongiorno, S. Scalese, F. La Via, D. Foti, J. Appl. Phys. **102**023518 (2007).

[37] Y. Ishida, T. Takahashi, H. Okumura, Jnp. J. Appl. Phys. **36**, 6633 (1997).

[38] N. Oyama, E. Ohta, K. Takeda, K. Shiraishi, H. Yamaguchi, J. Cryst. Growth, **433**, 900 (1999); Surf. Sci. **201/202**, 256 (1999).

[39] K. Shiraishi, N. Oyama, K. Okajima, N. Miyagishima, K. Takeda, H. Yamaguchi, T. Ito, T. Ohno, J. Cryst. Growth, **237**, 206 (2002).

[40] R. Choudhury, D. R. Bowler and M. J. Gillan, J. Phys. Condens. Matter **20** 235227 (2008).

[41] Y. Fujimoto and A. Oshiyama, Phys. Rev. B **81**, 205309 (2010).

[42] C. G. Van de Walle, Phy. Rev. B **39**, 1871 (1989).

[43] S. Y. Ren and J. D. Dow, Appl. Phys. Lett. 69, 251(1996).

[44] A. Ouerghi, R. Belkhou, M. Marangolo, M. G. Silly, S. El Moussaoui, M. Eddrief, L. Largeau, M. Portail and F. Sirotti, Appl. Phys. Lett. **97**, 3082 (2010).

[45] M. Suemitsu, Y. Miyamoto, H. Handa, and A. Konno, e-J. Surf. Sci. Nanotech. **7**, 311 (2009).

[46] M. Suemitsu, H. Fukidome, J. Phys. D: Appl. Phys. **43**, 374012 (2010).

[47] Y. Miyamoto, H. Handa, E. Saito, A. Konno, Y. Narita, M. Suemitsu, H. Fukidome, T. Ito, K. Yasui, H. Nakazawa, T. Endoh, e-J. Surf. Sci. Nanotech. **7**, 107 (2009).

[48] V. Yu Aristov, G. Urbanik, K. Kummer, D. V. Vyalikh, O. V. Molodtsova, A. B. Preobrajenski, A. A. Zakharov, C. Hess, T. Hänke, B. Büchner, I Vobornik, J. Fujii, G. Panaccione, Y. A. Ossipyan, M. Knupfer, Nano Lett. **10**, 992-995 (2010).

[49] A. Querghi, A. Kahouli, D. Lucot, M. Portail, L. Travers, J. Gierak, J. Penuelas, P. Jegou, A. Shukla, T. Chassagne and M. Zielinski, Appl. Phys. Lett. **96**, 191919 (2010).

[50] A. Querghi, M. Marangolo, R. Belkhou, S. El Moussaoui, M. G. Silly, M. Eddrief, L. Largeau, M. Portail, B. Fain and D. Sirotti, Phys. Rev. B **82**, 125445 (2010).

[51] M. Born and J. R Oppenheimer, Ann. Phys. **84**, 457 (1927).

[52] P. Hohenberg and W. Kohn Phys. Rev. **136**, B1864 (1964).

[53] W. Kohn and L. J. Sham, Phys. Rev. **140**, A1133 (1965).

[54] M. Levy, Proc. Nat. Acad. Sci. USA **76**, 6062 (1979).

[55] D. M. Ceperly and B. J. Alder Phys. Rev. Lett. **45**, 566 (1980).

[56] J. P. Perdew and A. Zunger Phys. Rev. B **23**, 5048 (1981).

[57] H. Hellmann, *Einfuhrung in die Quantumechemie* (Deuticcke, Leipzig, 1939).

[58] R. P. Feynman, Phys. Rev. **56**, 340 (1939).

[59] J.-I. Iwata, D. Takahashi, A. Oshiyama, T. Boku, K. Shiraishi, S. Okada and K. Y abana, J. Comp. Phys. **229**, 2339 (2010).

[60] E. Fermi, Il Nuovo Cimento **11**, 157 (1934).

[61] J.-I. Iwata, K. Shiraishi and A. Oshiyama, Phys. Rev. B **77**, 115208 (2008).

[62] E. L. Briggs, D. J. Sullivan, J. Bernholc, Phys. Rev. B **54**, 14362 (1996).

[63] C. Fiolhais, F. Nogueira and M. Marques, *A primier in Density Functional Theory* (Springer-Verlag, Heidelberg) (2003).

[64] L. Kleinman and D.M Bylander, Phys. Rev. Lett. **48**, 1425 (1982).

[65] B. J. Austine, V. Heine and L. J. Sham Phys. Rev. **127**, 276 (1962).

[66] N. Troullier and J L. Martins, Phys. Rev. B **43**, 1993 (1991).

[67] X. Gonze, R. Stumpf and M. Scheffler, Phys. Rev. B **44**, 8503 (1991).

[68] J. R. Chelikowsky, N. Troullier and Y. Saad, Phys. Rev. Lett. **72**, 1240 (1994).

[69] H. J. Monkhorst, J. D. Pack, Phys. Rev. B **13**, 5188 (1976).

[70] O. Jepson, O. .K Anderson, Solid State Communications **9**, 1763 (1971).

[71] G. Lehmann, M. Taut, Phys. stat. sol b **54**, 469 (1972).

[72] M. C. Payne, M. P. Teter, D. C Allan, T. A. Arrias and J. D. Joannopoulous Rev. Mod. Phys. **64**, 1045 (1992).

[73] J. Hafner, J. Comput. Chem. **29**, 2044 (2008).

[74] J. Kohanoff, *Electronic Structure Calculations for Solids and Molecules Theory and Computational Methods* pp. 90, Cambridge Univ. Press, UK (2006).

[75] P. Käckell, J. Furthmüller and F. Bechstedt, Appl. Surf. Sci. **104/105**, 45 (1995).

[76] B. Wenzien, P. Käckell, and F. Bechstedt, Surf. Sci. **989**, 307 (1994).

[77] F. M. Ross and J. Tersoff and R. M. Trom, Phys. Rev. Lett. **80**, 984 (1997).

[78] A. Fissel, K. Pfennighaus and W. Richter, Thin Solid Films **318**, 88 (1998).

[79] J. J Gilman, J. Appl. Phys. **31**, 2208 (1960).

[80] D. J. Eaglesham, A. E. White, L.C. Felman and D.C. Jacobson, Phys. Rev. Lett. **70**, 1643 (1993).

[81] B. N. Oshcherin Phys. Stat. sol a **34**, K181 (1976).

[82] J. H. Wilson, J. D. Todd, and A. P. Sutton, J. Phys, Condens. Mater **2**, 10259 (1990).

[83] G. H. Gilmer and A. F. Bakker, Mater. Res Soc. Sym Proc. **209**, 135 (1991).

[84] M. Tang and S. Yip, Phys. Rev. B **52**, 155150 (1995).

[85] T. Takai, T. Halicioglu, and W. A. Tiller, Surf. Sci. **164**, 327 (1985).

[86] A. A. Stekolnikov, J. Furthmüller and F. Beschstedt, Phys. Rev. B **65**, 11518-1 (2002).

[87] G. Kern, J. Hafner and G. Kresse, Surf. Sci. **366**, 445 (1996).

[88] G. Kern and J. Hafner, Phys Rev. B **56**, 4203 (1997).

[89] J. Furthmüller, J. Hafner and G. Kresse, Phys Rev. B **53**, 4203 (1996).

[90] K. D. Brommer, M. Needels, B. E. Larson and J. D Joannopoulos, Phys Rev. Lett. **66**, 1355 (1992).

[91] I. Stich, M. C. Payne, R. D. King-Smith, J.-S. Lin and L. J. Clark, Phys Rev. Lett. **68**, 1351 (1992).

[92] S. C. Erwin, A. A. Baski and L. J Whiteman, Phys Rev. Lett. **77**, 687 (1996).

[93] J. Wang, L. Zhang, Q. Zeng, G. L. Vignoles, L. Cheng and A. Guette, Phys. Rev. B **79**, 125304 (2009).

[94] D. J. Chadi, Phys. Rev. B **19**, 2074 (1979).

[95] J. Pollman, P. Krueger and M. Sabisch, Phys. stat. sol b **202**, 421 (1997).

[96] D. H. Lee, J. D. Joannopoulos, J. Vac. Sci. Technol. **2**, 21 (1982).

[97] S. P. Mehandru and A. B. Anderson, Phys. Rev. B **42**, 9040 (1990).

[98] A. A Stelkonikov, J. Furthmüller and F. Bechstedt Phys. Rev. Lett. **92**, 136104-1 (2004).

[99] A. Garcia and M. L. Cohen, Phys. Rev. B **47**, 4215 (1993).

[100] L. Kleinman, Phys. Rev. **128**, 2614 (1962).

[101] K. Takai, Ph.D. Thesis, University of Tsukuba, (2008).

[102] Z. C. Feng, W. J. Choyke, J. A. Powell, J. Appl. Phys. **64**, 12 (1988).

[103] W. R. L. Lambrecht, B. Segall, M. Methfessel, M. van Schilfgaarde, Phys. Rev. B **44** 3685 (1991).

[104] J. J. Wortman, R. A. Evans J. Appl. Phys. **36**, 153 (1964).

[105] W. A. Brantley, J. Appl. Phys. **44**, 534 (1973).

[106] G. Cicero, L. Pizzagalli and A. Catellani, Phys. Rev. Lett. **89**, 156101-1 (2002).

[107] L. Kleinman, Phys. Rev. **24**, 7412 (1981).